Engineering silk fibroin scaffolds to model hypoxia in neuroblastoma

A Dissertation
Submitted to the Faculty of
WORCESTER POLYTECHNIC INSTITUTE
In partial fulfillment of the requirements for the
Degree of Doctor of Philosophy in
Biomedical Engineering
July 26th, 2019
By

Kimberly J. Ornell

Approved by:

Jeannine M. Coburn, Ph.D.
Assistant Professor, Advisor
Biomedical Engineering
Worcester Polytechnic Institute

Marsha W. Rolle, Ph.D.
Associate Professor, Chair
Biomedical Engineering
Worcester Polytechnic Institute

George D. Pins, Ph.D.
Professor
Biomedical Engineering
Worcester Polytechnic Institute

Tanja Dominko, Ph.D., D.V.M.
Associate Professor
Biology and Biotechnology
Worcester Polytechnic Institute

Jason M. Shohet, M.D., Ph.D.
Associate Professor
Pediatrics
UMass Medical School

Acknowledgements

I would first and foremost like to thank my advisor Jeannine M. Coburn Ph.D. for all of her guidance and support over the past years. I appreciate the opportunity to work in your lab, learn from you, and all of the opportunities you provided me with. Thank you for all of the advice you have given.

I would also like to thank my committee, Marsha Rolle, George Pins, Tanja Dominko, and Jason Shohet for all of the time and feedback they have provided me with. Their guidance has been of great assistance in this project.

I would also like to thank the rest of the Biomedical Engineering faculty as well as lab staff in Gateway Park for their advice and technical knowledge.

I've been lucky enough to cross paths with many other graduate and undergraduate students who have helped me through my time at WPI. Especially, Coburn lab members both past and present Katelyn Mistretta, Elizabeth van Zyl, Alycia Abbott, Emily Newman, Natalia Vargas-Montoya, Coulter Raltson, Danilo Lozada and Carolina Villareal. I owe a special thanks to Nhi Phan who worked with me for 3 years as an undergraduate student and 1 year as a master's student. Many of the projects I completed would not have been done without her willingness to learn and assist.

Finally, I'd like to thank my friends and family for their support throughout my time here. I'd especially like to thank my husband Eric for having patience through a ll the weekends and late nights I worked, and particularly all the times I said I was leaving work and didn't leave for another few hours. Without the words of encouragement and endless support from my friends and family I would not have been able to complete this dissertation.

Table of Contents

Table of Figures

Table of Tables

Abbreviations

Neuroblastoma (NB)

Tumor associate macrophage (TAM)

Cancer associated fibroblast (CAF)

Natural Killer (NK)

Patient derived xenograft (PDX)

Genetically engineering mouse model (GEMM)

Hypoxia -Inducible Factor (HIF)

Periodic-acid Schiffs base (PAS)

Three dimensional (3D)

Two dimensional (2D)

Hypoxia inducible factor (HIF)

Vascular endothelial growth factor (VEGF)

Fetal bovine serum (FBS)

Glucose transporter 1 (GLUT1)

Carbonic Anhydrase 9 (CAIX)

Matrix metallopeptidase 9 (MMP9)

Insulin-like growth factor-binding protein 3 (IGFBP3)

Interleukin 8 (IL-8)

Interleukin 6 (IL-6)

Granulocyte-Macrophage Colony Stimulating Factor (GM-CSF)

Granulocyte-colony stimulating factor (G-CSF)

Interferon–inducible T Cell Alpha Chemoattractant (ITAC)

Monocyte chemotactic protein-3 (MCP-3)

Chemokine (C-C motif) ligand 3 (CCL3)

Urokinase receptor (uPAR)

Genetically engineered mouse model (GEMM)

Bone marrow-derived mesenchymal stromal cell (BM-MSC)

Knock-in (KI)

Knock-out (KO)

Normal goat serum (NGS)

Extracellular matrix (ECM)

Polytetrafluoroethylene (PTFE)

Previous Publications

Ornell, K. J., Lozada, D., Phan, N. V., & Coburn, J. M. (2019). Controlling methacryloyl substitution of chondroitin sulfate: injectable hydrogels with tunable long-term drug release profiles. Journal of Materials Chemistry B, 7(13), 2151-2161.

Taylor, J. S., Zeki, J., Ornell, K., Coburn, J., Shimada, H., Ikegaki, N., & Chiu, B. (2019). Down-regulation of MYCN protein by CX-5461 leads to neuroblastoma tumor growth suppression. Journal of pediatric surgery, 54(6), 1192-1197.

Niemas-Teshiba, R., Matsuno, R., Wang, L.L., Tang, X.X., Chiu, B., Zeki, J., Coburn, J., Ornell, K., Naranjo, A., Van Ryn, C. and London, W.B., 2018. MYC-family protein overexpression and prominent nucleolar formation represent prognostic indicators and potential therapeutic targets for aggressive high-MKI neuroblastomas: a report from the children’s oncology group. Oncotarget, 9(5), 6416-6432.

Yin, Y., Ornell, K.J., Beliveau, A. and Jain, A., 2016. Modulation of microRNAs 34a and 21 affects viability, senescence, and invasion in glioblastoma multiforme. Journal of biomedical nanotechnology, 12(9), pp.1782-1797.

Abstract

Development of novel oncology therapeutics is limited by a lack of accurate pre-clinical models for testing, specifically the inability of traditional 2D culture to accurately mimic *in vivo* tumors. Neuroblastoma (NB) is a heterogeneous tumor, that in high-risk patients exhibits a 5-year event free survival rate of less than 50%. As such, there is a clinical need for development of novel systems that can mimic the tumor microenvironment and allow for increased understanding of critical pathways as well as be used for preclinical therapeutic testing. In this thesis, lyophilized silk fibroin scaffolds were used to develop 3D neuroblastoma models (scaffolded NB) using multiple neuroblastoma cell lines. Cells grown on scaffolds in low (1%) and ambient (21%) oxygen were compared to traditional 2D (monolayer) cell culture using oxygen-controlled incubators. We hypothesized that scaffolded growth would promote changes in gene expression, cytokine secretion, and therapeutic efficacy both dependent and independent of hypoxia. Monolayer culturing in low oxygen exhibited increased expression of hypoxia related genes such as *VEGF*, *CAIX*, and *GLUT1*, while scaffolded NB exhibited increased expression of hypoxia related genes under both low and ambient oxygen conditions. Pimonidazole staining (hypoxia marker) confirmed the presence of hypoxic regions in the scaffolded NB. Cytokine secretion in monolayer and scaffolded NB suggested differential secretion of cytokines due to both oxygen concentrations (e.g. VEGF, CCL3, uPAR) and 3D culture (e.g. IL-8, GM-CSF, ITAC). Additionally, treatment with etoposide, a standard chemotherapeutic, demonstrated a reduced response in scaffolded culture as compared to monolayer culture regardless of oxygen concentration. However, use of a hypoxia activated therapeutic, tirapazamine exhibited response in low oxygen monolayer culture as well as scaffolded culture in both low and ambient oxygen. To further expand this model into a single culture system capable of generating cell driven oxygen gradients, a stacked culture system was developed. NB scaffolds were stacked using a holder designed based on COMSOL modeling of oxygen tension in the medium. Post-culture, the scaffolds can be separated for analysis on a layer-by-layer basis. Analysis of scaffolds demonstrated a decrease in dsDNA and an increase in hypoxia related genes (VEGF, CAIX, and GLUT1) at the interior of the stack, comparable to that of the scaffolded low oxygen culture. Scaffolds on the periphery of the stack retained gene expression levels similar to that of scaffolded ambient oxygen culture. COMSOL modeling of stacks suggests oxygen gradients present throughout the tumor model similar to that of an *in vivo* tumor. Gradients of oxygen were confirmed through positive pimonidazole staining. In summary, we developed a system capable of altering critical oxygen-dependent and independent pathways through controlled oxygen levels and 3D culturing. Further, we enhanced this system through the design of a culture system capable of controlling cell driven hypoxic microenvironments to mimic that of an *in vivo* tumor. This system has the potential to be applied to multiple cancer types, allowing for understanding of key pathway changes and better development of therapeutics.

Chapter 1: Overview

1.1. Introduction

Despite advances in understanding critical oncologic pathways, development of effective therapeutics remains a challenge. Treatment of heterogeneous and orphan cancers, such as neuroblastoma, is particularly difficult in part due to the lack of effective preclinical models for testing [1-3]. Therapeutics are typically tested on cells attached to polystyrene dishes and grown in 2D (monolayer cells) [4]. These cells lack critical microenvironment features and cell-cell signaling present *in vivo* [5-8]. Thus, 3D modeling has become a mechanism to bridge the gap between *in vitro* culture and *in vivo* systems.

One relevant tumor microenvironment feature is gradients of oxygen, which result in a hypoxic (<2% O_2) core within the tumor (**Figure 1.1**) [9-11]. Regions of hypoxia are a major feature of advanced cancer that influences both the tumor cells and the surrounding cells within the microenvironment [12-15]. Hypoxia initiates a number of pathway effects within tumors, leading to the promotion of aggressive, malignant tumor cells [9, 11, 12, 14, 16-20]. The hypoxic response is mainly attributed to hypoxia-inducible factors (HIFs). HIFs consist of three transcription factors, HIF1, HIF2, and HIF3 [21, 22]. Tumor cells, as well as the surrounding tumor

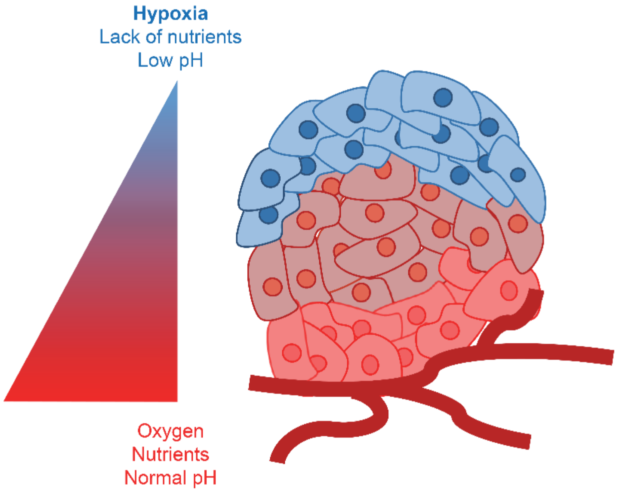

Figure 1.1. Schematic of gradients within a tumor.
Tumor cells further from vasculature demonstrated increased levels of hypoxia, lack of nutrients, and low pH. Tumor cells adjacent to vasculature demonstrate sufficient oxygenation, nutrients, and a normal pH.

microenvironment, are susceptible to HIF-driven transcriptional responses (**Figure 1.2.**) . In addition, the presence of hypoxia promotes an alternate (glycolytic) metabolism, as well as ECM remodeling to support metastases and vascularization [10, 13, 20, 22, 23]. Clinically, hypoxia has been linked to poor prognosis and resistance to therapeutics [9, 12, 19, 20, 24]. Thus, there is a need to develop *in vitro* systems to accurately mimic *in vivo* tumor hypoxia.

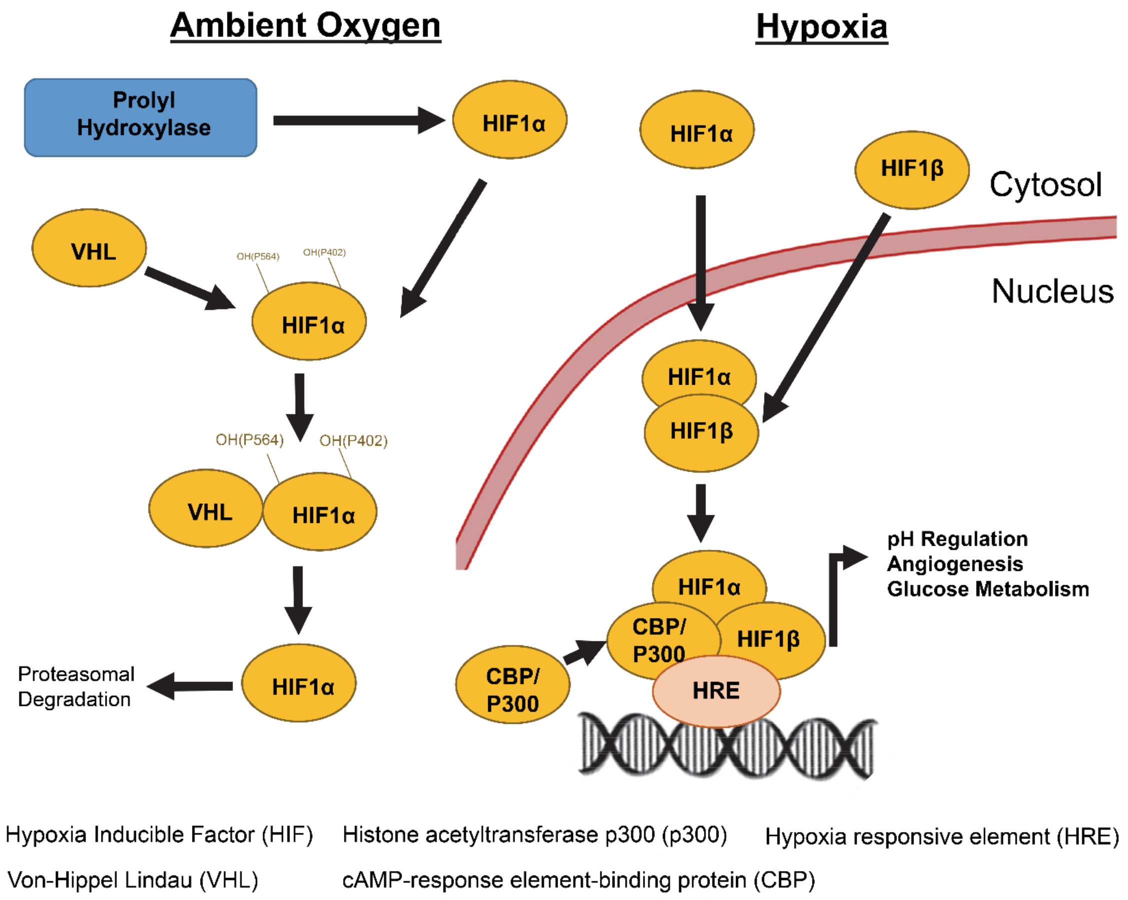

Figure 1.2. Hypoxic pathway in cancer cells.
Under normoxic conditions, HIF 1α is hydroxylated at proline residues 402 and 564 by proplyl hydroxylase domain containing proteins PHD1-3. HIF 1α then binds to VHL at these domainsleading to ubiquitination and proteosomal degradation within the cytosol. However, under hypoxia conditions this hydroxylation and degradation are impaired due to lack of oxygen. HIF 1α does not bind to VHL and instead it translocates to and accumulates in the nucleus. It then heterodimerizes with HIF 1β, recruits coactivators such as CBP/P300 and binds to the core DNA sequence RCTCG at hypoxia-responsive elements (HREs) in target genes. This leads to transcriptional induction of target genes.

Currently, many 3D culture systems have been employed to achieve more physiologically relevant tumor models. The most common 3D model is cells grown as spheroids, or aggregates of cells. These models have a critical size of approximately 400 µm and are able to partially recapitulate the *in vivo* microenvironment [7, 25-29]. However, spheroids are size limited (400 µm), are difficult to generate in a uniform size, and drug treating and changing the medium are challenging [30, 31]. An alternative to spheroids is tissue engineered scaffolded cultures. Scaffolding may act as a substitute for tumor ECM, providing physical support for the tumor cells and controlling spatial distribution.

Scaffold-based approaches consist primarily of natural and synthetic polymers. Natural polymers include collagen (and other ECM components), chitosan, proteoglycans, fibrin, agarose, and alginate [32-38]. As compared to synthetic polymers, they exhibit higher biocompatibility and lower toxicity. Additionally, scaffold materials may be bioactive. This can enhance cell proliferation and adhesion but can also influence cell morphology and pathway expression. Synthetic polymers, such as polyesters, polyglycolic acid, polylactic acid, and their respective copolymers/blends are advantageous as they are highly versatile, reproducible, and easier to process [39-41]. A wide variety of techniques can be used to process scaffold materials. These include freeze-drying (lyophilization), solvent casting/particle leaching, electrospinning, phase inversion, stereolithography, and 3D printing [42-45]. Many of these processes are limited due to the use of toxic solvents and batch-batch variability.

Silk fibroin is a natural biomaterial capable of being processed in an entirely aqueous method to generate porous 3D scaffolds [46-48]. It has been demonstrated to be biocompatible, have limited immunogenicity, and be stable at a wide range of temperatures and pH [46-49]. There are many different methods of fabricating silk into porous scaffolds. The most common include salt-leaching and lyophilization [48]. Salt-leaching involves mixing of silk solution with salt particles of a specific diameter. The salt content causes the silk to gel resulting in a water-stable porous material. These scaffolds create highly interconnected pores with pore size determined by the salt particle diameter. However, the minimum pore size for salt leached scaffolds is approximately 250 µm, which makes fabrication of thin (200 µm), mechanically stable scaffolds difficult. Lyophilization of silk fibroin creates a stable porous sponge-like scaffold, with an average pore size of 70-90 µm. Pores exhibit a honey-comb like structure with large enough pores to facilitate cell-cell interactions, but small enough pores to fabricate thin, stable materials. These scaffolds have been used both *in vitro* and *in vivo* for disease modeling and tissue engineering [46-49]. Cells can grow on silk scaffolds and within the porous structure without the incorporation of ECM components [46, 49-52]. However, analysis of potential hypoxic regions within silk scaffolds has not been examined, particularly for the use of engineering tumor microenvironments.

1.2. Overall goal and hypothesis

The overall goal of this project was to develop a culture system for 3D growth of neuroblastoma capable of characterizing different levels of the tumor microenvironment, specifically cell driven hypoxic gradients.

We hypothesize that 3D culture of neuroblastoma will induce expression of hypoxia-related genes and cytokines, as well as promote resistance to cytotoxic chemotherapeutics.

To test this hypothesis and develop this culture system, this dissertation was separated into two specific aims. We investigated the role of hypoxia and 3D culture on NB gene expression, cytokine secretion, and therapeutic efficacy in **Specific Aim 1**. Using low oxygen incubators and modeling of oxygen gradients we were able to elucidate whether changes were driven by hypoxia and 3D culture. In **Specific Aim 2**, we developed a culture system capable of controlling oxygen gradients by stacking scaffolds seeded with NB cells. The expected outcome of this dissertation was the identification of a system to determine changes in genes and cytokines induced in 3D growth and/or hypoxia, and the fabrication of a culture system capable of capturing multiple levels of tumor hypoxia in a single culture.

1.3. Specific Aim 1: Evaluate the impact scaffolded NB growth and hypoxia on relevant gene expression, cytokine secretion, and drug sensitivity.

A significant challenge in understanding cancer-relevant pathways and developing effective therapeutics is generating effective tumor model systems. The goal of this aim was to develop a model system that could elucidate the effects of scaffolded growth and hypoxia on NB gene expression, cytokine secretion, and therapeutic response. In **Chapter 3** of this thesis, we analyzed the effects of scaffolded growth and hypoxia on NB cell lines. Cells were grown in lyophilized silk scaffolds with a thickness of 200 µm at 21% (ambient) or 1% (low) oxygen. Scaffolded NB cells were compared to cells grown in traditional monolayer culture at ambient and low oxygen. Cells grown on silk scaffolds demonstrated upregulation of hypoxic markers as compared to monolayer cells grown in ambient oxygen. COMSOL modeling and use of hypoxic stain pimonidazole confirmed the presence of hypoxic regions within the scaffolds. Comparison of cells grown in low oxygen, scaffolds grown in low oxygen, and scaffolds grown in ambient oxygen allowed for the elucidation of whether critical changes were due to hypoxia or to scaffolded culture. Analysis of cytokine secretion demonstrated differential secretion profiles based on scaffolded growth and hypoxia. Hypoxia (both from scaffolded growth and low oxygen incubators) demonstrated upregulation of angiogenic and proinflammatory cytokines. A subset of cytokines, including IL-8, GM-CSF, and ITAC, demonstrated increased secretion only in scaffolded culture, suggesting changes specific to scaffolded growth. These secretion changes were confirmed through a combination of PCR and ELISA assays. Treatment with clinically used chemotherapeutic etoposide demonstrated enhanced resistance in scaffolded culture. No significant differences were observed in monolayer culture in the presence of hypoxia, suggesting that scaffolded culturing was the primary driver of resistance. When treated with the hypoxia-activated therapeutic tirapazamine, monolayer low oxygen culture, and scaffolded culture in low and ambient oxygen demonstrated a significant increase in cell response as compared to monolayer ambient oxygen culture. This suggests that therapeutic efficacy has differential effects based on culture conditions. Taken together, these data demonstrate the ability to modify NB culture conditions by employing hypoxia and scaffolds to more closely mimic that of an *in vivo* tumor. Ultimately, we anticipate that we can strategically use these culture methods to better understand NB pathways and better evaluate therapeutic efficacy.

1.4. Specific Aim 2: Design, fabricate, and evaluate a culture system capable of controllable cell driven microenvironments.

In vivo tumors express a range of oxygen gradients dependent on the distance between tumor cells and supplies of oxygen and nutrients. These cell-driven gradients are important to the tumor microenvironment as they drive critical pathways and can promote therapeutic resistance, metastasis, and overall malignancy. Development of *in vitro* models capable of generating these gradients remains a challenge. Scaffold are frequently limited by infiltration of cells (particularly for thicker scaffolds), while solid spheroid models are heterogeneous in size, difficult to control, and frequently exhibit necrotic centers. In **Chapter 4** of this thesis, we designed, fabricated, and evaluated a culture system capable of controllable cell driven microenvironments. Due to limitations in scaffold thickness, we determined that stacking of scaffolds was necessary to create cell-driven microenvironments. COMSOL modeling was used to identify scaffold holder parameters based on rate of oxygen diffusion to the cells to allow for generation of hypoxic gradients within stacks. Further, using COMSOL, we identified a minimum stack thickness (4 scaffolds) capable of differential oxygen levels throughout the layers of scaffolds. Hematoxylin and eosin staining of stacks demonstrated presence of cells throughout the stacked scaffolds. Analysis of DNA content demonstrated reduced dsDNA within the interior of the stack, similar to that of single scaffolds grown in low oxygen. Expression of hypoxia-driven genes in stacks were compared to cells grown in single scaffolds under ambient and low oxygen conditions. Scaffolds on the exterior of the stack demonstrated comparable expression of hypoxic markers to single scaffolds grown in ambient oxygen. Scaffolds at the interior of the stack demonstrated an up regulation of hypoxic markers, consistent with that of single scaffolds grown in low oxygen. Immunofluorescence staining for hypoxia (pimonidazole) confirmed a gradient of oxygen within the stacked scaffolds. These data demonstrate that stacked scaffolds experience different levels of hypoxia regulation in each layer due to cell-driven microenvironment changes. These changes are analogous to changes observed in *in vivo* tumors, suggesting that this culture system may provide new insight into clinically relevant pathway changes and responses to therapeutics.

1.5. References

[1] G.M. Brodeur, A. Nakagawara, Molecular basis of clinical heterogeneity in neuroblastoma, Am J Pediatr Hematol Oncol 14(2) (1992) 111-6.
[2] J.M. Maris, M.D. Hogarty, R. Bagatell, S.L. Cohn, Neuroblastoma, Lancet 369(9579) (2007) 2106-20.
[3] J.R. Park, A. Eggert, H. Caron, Neuroblastoma: biology, prognosis, and treatment, Hematol Oncol Clin North Am 24(1) (2010) 65-86.
[4] A. Riedl, M. Schlederer, K. Pudelko, M. Stadler, S. Walter, D. Unterleuthner, C. Unger, N. Kramer, M. Hengstschlager, et al., Comparison of cancer cells in 2D vs 3D culture reveals differences in AKT-mTOR-S6K signaling and drug responses, J Cell Sci 130(1) (2017) 203-218.
[5] L.G. Griffith, M.A. Swartz, Capturing complex 3D tissue physiology in vitro, Nat Rev Mol Cell Biol 7(3) (2006) 211-24.
[6] A. Nyga, U. Cheema, M. Loizidou, 3D tumour models: novel in vitro approaches to cancer studies, J Cell Commun Signal 5(3) (2011) 239-48.
[7] H.R. Kumar, X. Zhong, D.J. Hoelz, F.J. Rescorla, R.J. Hickey, L.H. Malkas, J.A. Sandoval, Three-dimensional neuroblastoma cell culture: proteomic analysis between monolayer and multicellular tumor spheroids, Pediatr Surg Int 24(11) (2008) 1229-34.
[8] T. Teitz, J.J. Stanke, S. Federico, C.L. Bradley, R. Brennan, J.K. Zhang, M.D. Johnson, J. Sedlacik, M. Inoue, et al., Preclinical Models for Neuroblastoma: Establishing a Baseline for Treatment, Plos One 6(4) (2011).
[9] H.M. Ameis, A. Drenckhan, M. Freytag, J.R. Izbicki, C.T. Supuran, K. Reinshagen, S. Holland-Cunz, S.J. Gros, Influence of hypoxia-dependent factors on the progression of neuroblastoma, Pediatr Surg Int 32(2) (2016) 187-92.
[10] J.A. Bertout, S.A. Patel, M.C. Simon, The impact of O2 availability on human cancer, Nat Rev Cancer 8(12) (2008) 967-75.
[11] R. Courtnay, D.C. Ngo, N. Malik, K. Ververis, S.M. Tortorella, T.C. Karagiannis, Cancer metabolism and the Warburg effect: the role of HIF-1 and PI3K, Mol Biol Rep 42(4) (2015) 841-51.
[12] A. Jogi, I. Ora, H. Nilsson, A. Lindeheim, Y. Makino, L. Poellinger, H. Axelson, S. Pahlman, Hypoxia alters gene expression in human neuroblastoma cells toward an immature and neural crest-like phenotype, Proc Natl Acad Sci U S A 99(10) (2002) 7021-6.
[13] B. Muz, P. de la Puente, F. Azab, A.K. Azab, The role of hypoxia in cancer progression, angiogenesis, metastasis, and resistance to therapy, Hypoxia (Auckl) 3 (2015) 83-92.
[14] E.B. Rankin, J.M. Nam, A.J. Giaccia, Hypoxia: Signaling the Metastatic Cascade, Trends Cancer 2(6) (2016) 295-304.
[15] A.S. Truong, M.R. Lockett, Oxygen as a chemoattractant: confirming cellular hypoxia in paper-based invasion assays, Analyst 141(12) (2016) 3874-82.
[16] F. Agani, B.H. Jiang, Oxygen-independent regulation of HIF-1: novel involvement of PI3K/AKT/mTOR pathway in cancer, Curr Cancer Drug Targets 13(3) (2013) 245-51.
[17] J. Chiche, K. Ilc, J. Laferriere, E. Trottier, F. Dayan, N.M. Mazure, M.C. Brahimi-Horn, J. Pouyssegur, Hypoxia-inducible carbonic anhydrase IX and XII promote tumor cell growth by counteracting acidosis through the regulation of the intracellular pH, Cancer Res 69(1) (2009) 358-68.
[18] L. D'Ignazio, M. Batie, S. Rocha, Hypoxia and Inflammation in Cancer, Focus on HIF and NF-kappaB, Biomedicines 5(2) (2017).

[19] J. Hartwich, W.S. Orr, C.Y. Ng, Y. Spence, C. Morton, A.M. Davidoff, HIF-1 alpha activation mediates resistance to anti-angiogenic therapy in neuroblastoma xenografts, J Pediatr Surg 48(1) (2013) 39-46.
[20] P. Ramani, A. Headford, M.T. May, GLUT1 protein expression correlates with unfavourable histologic category and high risk in patients with neuroblastic tumours, Virchows Arch 462(2) (2013) 203-9.
[21] A. Palazon, A.W. Goldrath, V. Nizet, R.S. Johnson, HIF transcription factors, inflammation, and immunity, Immunity 41(4) (2014) 518-28.
[22] A.M. Graham, J.S. Presnell, Hypoxia Inducible Factor (HIF) transcription factor family expansion, diversification, divergence and selection in eukaryotes, PLoS One 12(6) (2017) e0179545.
[23] A. Zimna, M. Kurpisz, Hypoxia-Inducible Factor-1 in Physiological and Pathophysiological Angiogenesis: Applications and Therapies, Biomed Res Int 2015 (2015) 549412.
[24] P. Fardin, A. Barla, S. Mosci, L. Rosasco, A. Verri, R. Versteeg, H.N. Caron, J.J. Molenaar, I. Ora, et al., A biology-driven approach identifies the hypoxia gene signature as a predictor of the outcome of neuroblastoma patients, Mol Cancer 9 (2010).
[25] N. Baek, O.W. Seo, M. Kim, J. Hulme, S.S.A. An, Monitoring the effects of doxorubicin on 3D-spheroid tumor cells in real-time, Oncotargets and Therapy 9 (2016) 7207-7218.
[26] A. Coulon, M. Flahaut, A. Muhlethaler-Mottet, R. Meier, J. Liberman, K. Balmas-Bourloud, K. Nardou, P. Yan, S. Tercier, et al., Functional sphere profiling reveals the complexity of neuroblastoma tumor-initiating cell model, Neoplasia 13(10) (2011) 991-1004.
[27] S. Daster, N. Amatruda, D. Calabrese, R. Ivanek, E. Turrini, R.A. Droeser, P. Zajac, C. Fimognari, G.C. Spagnoli, et al., Induction of hypoxia and necrosis in multicellular tumor spheroids is associated with resistance to chemotherapy treatment, Oncotarget 8(1) (2017) 1725-1736.
[28] J.B. Kim, Three-dimensional tissue culture models in cancer biology, Semin Cancer Biol 15(5) (2005) 365-377.
[29] N.R. Patel, B. Aryasomayajula, A.H. Abouzeid, V.P. Torchilin, Cancer cell spheroids for screening of chemotherapeutics and drug-delivery systems, Ther Deliv 6(4) (2015) 509-20.
[30] L.M. Griner, K. Gampa, T. Do, H. Nguyen, D. Farley, C.J. Hogan, D.S. Auld, S.J. Silver, Generation of High-Throughput Three-Dimensional Tumor Spheroids for Drug Screening, J Vis Exp (139) (2018).
[31] O.I. Hoffmann, C. Ilmberger, S. Magosch, M. Joka, K.W. Jauch, B. Mayer, Impact of the spheroid model complexity on drug response, J Biotechnol 205 (2015) 14-23.
[32] C. Curtin, J.C. Nolan, R. Conlon, L. Deneweth, C. Gallagher, Y.J. Tan, B.L. Cavanagh, A.Z. Asraf, H. Harvey, et al., A physiologically relevant 3D collagen-based scaffold-neuroblastoma cell system exhibits chemosensitivity similar to orthotopic xenograft models, Acta Biomater 70 (2018) 84-97.
[33] K.A. Fitzgerald, J.F. Guo, E.G. Tierney, C.M. Curtin, M. Malhotra, R. Darcy, F.J. O'Brien, C.M. O'Driscoll, The use of collagen-based scaffolds to simulate prostate cancer bone metastases with potential for evaluating delivery of nanoparticulate gene therapeutics, Biomaterials 66 (2015) 53-66.
[34] E.L.S. Fong, S.E. Lamhamedi-Cherradi, E. Burdett, V. Ramamoorthy, A.J. Lazar, F.K. Kasper, M.C. Farach-Carson, D. Vishwamitra, E.G. Demicco, et al., Modeling Ewing sarcoma tumors in vitro with 3D scaffolds, P Natl Acad Sci USA 110(16) (2013) 6500-6505.

[35] J. Kazantseva, R. Ivanov, M. Gasik, T. Neuman, I. Hussainova, Graphene-Augmented Nanofiber Scaffolds Trigger Gene Expression Switching of Four Cancer Cell Types, Acs Biomater Sci Eng 4(5) (2018) 1622-1629.
[36] M. Mitra, C. Mohanty, A. Harilal, U.K. Maheswari, S.K. Sahoo, S. Krishnakumar, A novel in vitro three-dimensional retinoblastoma model for evaluating chemotherapeutic drugs, Mol Vis 18(142-45) (2012) 1361-1378.
[37] K.D. Roehm, S.V. Madihally, Bioprinted chitosan-gelatin thermosensitive hydrogels using an inexpensive 3D printer, Biofabrication 10(1) (2018).
[38] X. Xu, M.C. Farach-Carson, X. Jia, Three-dimensional in vitro tumor models for cancer research and drug evaluation, Biotechnol Adv 32(7) (2014) 1256-1268.
[39] Y.K. Girard, C. Wang, S. Ravi, M.C. Howell, J. Mallela, M. Alibrahim, R. Green, G. Hellermann, S.S. Mohapatra, et al., A 3D fibrous scaffold inducing tumoroids: a platform for anticancer drug development, PLoS One 8(10) (2013) e75345.
[40] S. Moscato, F. Ronca, D. Campani, S. Danti, Poly(vinyl alcohol)/gelatin Hydrogels Cultured with HepG2 Cells as a 3D Model of Hepatocellular Carcinoma: A Morphological Study, J Funct Biomater 6(1) (2015) 16-32.
[41] G. Huang, F. Li, X. Zhao, Y. Ma, Y. Li, M. Lin, G. Jin, T.J. Lu, G.M. Genin, et al., Functional and Biomimetic Materials for Engineering of the Three-Dimensional Cell Microenvironment, Chem Rev 117(20) (2017) 12764-12850.
[42] J. Xue, T. Wu, Y. Dai, Y. Xia, Electrospinning and Electrospun Nanofibers: Methods, Materials, and Applications, Chem Rev 119(8) (2019) 5298-5415.
[43] D.W. Hutmacher, Scaffold design and fabrication technologies for engineering tissues--state of the art and future perspectives, J Biomater Sci Polym Ed 12(1) (2001) 107-24.
[44] A. Cheng, Z. Schwartz, A. Kahn, X. Li, Z. Shao, M. Sun, Y. Ao, B.D. Boyan, H. Chen, Advances in Porous Scaffold Design for Bone and Cartilage Tissue Engineering and Regeneration, Tissue Eng Part B Rev 25(1) (2019) 14-29.
[45] S.J. Hollister, Porous scaffold design for tissue engineering, Nat Mater 4(7) (2005) 518-24.
[46] C. Correia, S. Bhumiratana, L.P. Yan, A.L. Oliveira, J.M. Gimble, D. Rockwood, D.L. Kaplan, R.A. Sousa, R.L. Reis, et al., Development of silk-based scaffolds for tissue engineering of bone from human adipose-derived stem cells, Acta Biomater 8(7) (2012) 2483-92.
[47] J. Rnjak-Kovacina, L.S. Wray, K.A. Burke, T. Torregrosa, J.M. Golinski, W. Huang, D.L. Kaplan, Lyophilized Silk Sponges: A Versatile Biomaterial Platform for Soft Tissue Engineering, Acs Biomater Sci Eng 1(4) (2015) 260-270.
[48] D.N. Rockwood, R.C. Preda, T. Yucel, X. Wang, M.L. Lovett, D.L. Kaplan, Materials fabrication from Bombyx mori silk fibroin, Nat Protoc 6(10) (2011) 1612-31.
[49] L.S. Wray, J. Rnjak-Kovacina, B.B. Mandal, D.F. Schmidt, E.S. Gil, D.L. Kaplan, A silk-based scaffold platform with tunable architecture for engineering critically-sized tissue constructs, Biomaterials 33(36) (2012) 9214-24.
[50] A. Backer, O. Erhardt, L. Wietbrock, N. Schel, B. Goppert, M. Dirschka, P. Abaffy, T. Sollich, A. Cecilia, et al., Silk scaffolds connected with different naturally occurring biomaterials for prostate cancer cell cultivation in 3D, Biopolymers 107(2) (2017) 70-79.
[51] E. Dondajewska, W. Juzwa, A. Mackiewicz, H. Dams-Kozlowska, Heterotypic breast cancer model based on a silk fibroin scaffold to study the tumor microenvironment, Oncotarget 9(4) (2018) 4935-4950.

[52] B. Subia, T. Dey, S. Sharma, S.C. Kundu, Target specific delivery of anticancer drug in silk fibroin based 3D distribution model of bone-breast cancer cells, ACS Appl Mater Interfaces 7(4) (2015) 2269-79.

Chapter 2: Background

2.1. Need for a more accurate preclinical neuroblastoma model

Neuroblastoma (NB) is the most common extracranial childhood tumor, accounting for approximately 15% of all childhood cancer deaths [1-3]. Nearly half of all patients are classified as having high-risk disease, portending poor long-term survival despite multimodal treatment [4]. NB is a disease of the sympaticoadrenal lineage of the neural crest, with tumors forming anywhere in the sympathetic nervous system. Tumors most commonly arise in the abdomen (65%), however they also occur in the neck, chest, and pelvis. Approximately 50% of patients present with evidence of metastasis [5, 6]. Frequent metastasis sites include cortical bone, bone marrow, liver, and lymph nodes [5, 6]. The disease exhibits a broad range of clinical behaviors, making treatment difficult, particularly for high-risk patients [1, 4]. While NB typically occurs in children who do not have a family history of the disease, there are some genetic changes frequently associated with the disease [7]. The most commonly genetic change is MYCN amplification, occurring in approximately 20% of patients, which strongly correlated with advanced stage NB [8, 9]. In addition, deletions of the short arm of chromosome 1 (1p) are found in 25-35% of patients and can be correlated with MYCN amplification [10-12]. Outside of MYC linked changes, allelic loss of 11q is present in 35-45% of patients and is also associated with high-risk disease features [13, 14].

Treatment strategies for NB are guided by the staging and risk level of the disease. In low risk patients, surgery is frequently curative. Should recurrence of NB occur, it is usually local to the original tumor site and can be managed surgically [14, 15]. Use of cytotoxic therapies is typically avoided due to the high amount of long-term complications [16]. Treatment for patients with intermediate or high-risk NB consists of a multimodal approach including surgical resection, chemotherapy, and radiation [4]. Therapy for high-risk NB begins with resection of the primary tumor coupled with chemotherapy and radiation to manage the tumor size and facilitate resection [17, 18]. However, if the tumor is too large for surgical resection, an initial induction treatment with chemotherapy is utilized to shrink the tumor. Chemotherapies typically used include doxorubicin, vincristine, cisplatin, etoposide, and cyclophosphamide [19]. In addition, stem cell rescue can be used during the consolidation part of the therapeutic regime after high-dose chemotherapy to kill the cells within the bone marrow [20].

There are many therapeutics currently undergoing preclinical development or in clinical trials for NB including: cytotoxic agents such as topoisomerase 1 inhibitors, radionuclides, retinoids, angiogenesis inhibitors, and tyrosine kinase inhibitors [21-26]. Recently, immunotherapy has emerged as a promising therapy to improve outcomes in patients with advanced stage NB, specifically targeting the highly expressed disialoganglioside GD2. Currently, monoclonal antibodies for GD2 have been clinically approved for therapy in combination with GM-CSF, IL-2, and 13-cis-retinoic acid, while other forms of immunotherapy (e.g. T-cell) are still under development [27-29]. Despite the emergence of novel treatment strategies including immunotherapeutics, the prognosis for high-risk patients remains poor.

NB is a heterogeneous cancer, with few distinct subtypes and many different clinical presentations [30]. Development of effective therapeutics is dependent on understanding tumor heterogeneity and the ability to accurately test therapies in a preclinical setting. Preclinical models typically use developed environments (murine or *in vitro*) to assess how a tumor will respond to therapeutics. The high degree of heterogeneity, lack of a consistent genetic marker, and range of prognosis (dependent on stage) makes development of an accurate preclinical model difficult. This chapter highlights current strategies and challenges of *in vitro* and *in vivo* NB modeling for preclinical therapeutic testing.

2.2. Preclinical murine models

Murine models are frequently used for preclinical testing of therapeutics due to their genetic homology to humans (~80%), ability to be genetically manipulated to mimic human diseases, and complex multicomponent environment (e.g. stroma, immune cells) [31]. They are advantageous as they provide information regarding therapeutic efficacy that cannot be demonstrated in traditional, less complex monolayer *in vitro* cultures. Murine models are typically a necessary stage before progressing therapies to clinical trials. There are many different types of murine models, including genetically engineered models, spontaneously formed tumors, mice with implanted mouse or human tumors, and, more recently, mixed cell type xenograft models. Each of these models is uniquely suited for preclinical testing of therapeutics, however there is still a need for further development and refinement to drive the development of successful therapeutics.

2.2.1. Transgenic mouse models

Transgenic mice, also referred to as genetically engineered mouse models (GEMMs), can be engineered through promotion or addition of genes (knock-in) or inhibition of gene expression (knock-out). Methods of GEMM development have been reviewed elsewhere [32, 33]. **Table 2.1** contains a list of currently used GEMMs for NB. The most widely used GEMM researched for NB is the TH-MYCN model developed by Weiss et al. [34]. These mice overexpress MYCN through a tyrosine hydroxylase promoter. This model was the first to demonstrate that MYCN amplification can drive NB development, identifying the MYCN pathway as a potential therapeutic target. Tumors generated from MYCN overexpressing mice have MYCN protein levels similar to that of the established NB KELLY cell line, known to contain amplified MCYN [34]. Additionally, similar histopathology is observed between MYCN-amplified patient tumor samples and TH-MYCN tumors [35]. This model has been used extensively in preclinical testing for small molecule inhibitors and chemotherapeutics [35-41]. MYCN pathway inhibitors that showed success *in vitro* in MYCN-amplified cell lines, such as bromodomain and extra-terminal domain protein inhibitors and cyclin-dependent kinase inhibitors, demonstrated similar results in the TH-MYCN model [37, 42, 43]. High MYCN expression has been linked to high levels of angiogenesis. TH-MYCN tumors treated with angiogenic inhibitors, such as the angiogenesis inhibitor TNP-470, demonstrated a high level of response with intact blood vessels being replaced with hemorrhagic areas containing necrosis and apoptosis [35]. This model has also been used, although in a limited capacity, for testing immune checkpoint inhibitors [44]. While the TH-MYCN model has been considered the standard for preclinical modeling of MYCN amplified tumors, there are some limitations. There is a high rate of tumor incidence in the 129/SVJ background (100% for homozygous mice and 33% for heterozygous mice), but a considerably lower rate of incidence in alternative background strains such as BL6 (5% incidence), this makes crossing this strain with established BL6 GEMMs a challenge [34]. Additionally, distant metastasis frequently occur in the clinical presentation of MYCN-amplified tumors, but are rarely observed in the TH-MYCN model [45]. This model is also limited by a long development time (an average of 65 days), making it difficult for rapid, high-throughput testing [45, 46].

To address some of the limitations of the TH-MYCN model, a mouse with Cre inducible MYCN expression (LSL-MYCN;Dbh-iCre) was created [46]. This model has a better-defined transgene insertion site allowing tumors to develop from multiple locations in the neural crest, such as the adrenals, and the celiac and superior cervical ganglia. It allows for tumor development in multiple mouse strain backgrounds, unlike the TH-MYCN which has a low incidence in backgrounds other than 129/SvJ [46], which is important when attempting to combine the TH-MYCN mouse with other cancer relevant alleles. LSL-MYCN;Dbh-iCre mice recapitulates NB histology and in molecular expression patterns. These mice are advantageous as compared to TH-MYCN mice as it localizes the transgene insertion to the ROSA26 locus, a commonly used locus for genetic insertion, which when discontinued has no phenotypic change in mice. Alternatively, the TH-MYCN mouse primarily inserts into the distal region of chromosome 18, the effects of which have not fully been characterized. While the insertion site has been changed, MYCN expression increased to comparable levels as the TH-MYCN model. Cell lines derived from the LSL-MYCN;Dbh-iCre mouse respond to MYCN targeting drugs, MLN8327 and JQ1 [46]. This model presents a more defined MYCN-amplified tumor model for preclinical testing, and could prove useful in the future for testing of therapies aimed at treating high risk MYCN-amplified NB.

In addition to the LSL-MYCN;Dbh-iCre mouse, the TH-MYCN mouse has been genetically modified to incorporate other oncogenes. A cross of a TH-Cre caspase-8 knockout mouse with a TH-MYCN mouse exhibited increased bone marrow metastasis as compared to the TH-MYCN mouse (37% versus 5% incidence) [47]. Loss of caspase-8 does not change the incidence of primary tumors, however it does change the extracellular matrix (ECM) structure of the primary tumor into a more migratory phenotype with increased collagen 4A2 and laminin α4 as well as increased EMT genes (Snai2, Twist1 and TfpI2). The metastatic propensity of this model could be useful in identifying treatments for metastatic NB. In addition, similar to clinical treatment strategies, the primary tumors in the mice could be debulked and allowed to metastasize. This could allow for this model to be used to gain knowledge about the metastatic population and identify therapeutic approaches specifically geared towards those tumors [47].

To mimic the impaired p53 function frequently present in high-risk NB recurrence, a TH-MYCN/Trp53(KI/KI) mouse with a tamoxifen inducible p53ER fusion protein was created [48]. Survival in TH-MYCN/Trp53(KI/KI) mice was reduced, and the tumors exhibited decreased radiosensitivity [48]. In addition, when functional p53 was restored to these mice, only 50% regained sensitivity to radiation, suggesting other resistance mechanisms. The authors also identified upregulation of the glutathione S-transferase pathway in this model, which was correlated with poor survival in NB patients [48]. TH-MYCN/Trp53(KI/KI) allografted tumors treated with the glutathione S-transferase pathway inhibitor buthionine sulfoximine regained sensitization to radiation, suggesting a potential therapeutic strategy for patients with amplified MYCN and impaired p53 function [48].

Other mutations have been examined as a method of inducing NB, such as activation of anaplastic lymphoma kinase mutations [49], present in approximately 10% of NB [50]. One model used targeted expression of the most common and aggressive ALK mutation ALK^{F1174}. This model exhibited a similar phenotype to NB and syntenic changes to those present in clinical NB including 17q gain and MYCN amplification [51]. Preclinically, this model has been used to evaluate drug response to ALK inhibitors and may provide useful insight into treatments for ALK mutated NB. To provide a model comparable to patient tumor that exhibit both MYCN amplification and ALK mutations, the ALK^{F1174} mutation model was crossed with TH-MYCN mice [52]. Mice hemizygotic for both ALK^{F1174L} and MYCN exhibited high tumor penetrance with rapid lethality superior to that observed in MYCN hemizygotes allowing for elucidation of the interplay between the ALK and MYCN pathways [53].

Finally, a transgenic mouse line carrying tetracycline inducible simian virus 40 T-antigen (SV40 Tag) has been created using tetracycline responsive elements with a cytomegalovirus promoter and SV40 Tag [54]. These mice all die by 28 weeks of age and exhibit bilateral adrenal tumors. When compared to both human adrenal NB and pheochromocytoma, higher similarity to human NB tumors as compared to the pheochromocytoma was observed. NB-associated genetic changes were present with upregulation of: MYCN, paired-like homeobox 2b, gamma-aminobutyric acid A receptor beta3 subunit, islet 1, and kinesin family member 1A [54, 55]. In addition, when this model was linked to the olfactory marker protein promoter region, it generated a line of mice with highly metastatic tumors originating in the adrenals or sympathetic ganglia. These metastatic tumors were morphologically very similar to clinical NB histologically [56]. While limited preclinical therapeutic testing has been performed with these models, it has the potential to be promising for therapeutic testing due to its genetic similarity to NB and ability to mimic metastasis.

GEMMs are advantageous as they utilize mouse homologs of tumorigenic mutations present in patient tumors to mirror clinical tumors. The mouse retains an intact immune system and stroma, allowing for evaluation of therapeutics that target both the tumor and the surrounding microenvironment. In addition, GEMMs have specific pathway activations, allowing for analysis and targeted therapeutic testing [42, 52, 57]. The genetic changes are constitutively active in mice throughout development or can be induced at a specific development stage. This is important as neuroblastoma arises from developing cells in pediatric patients. In addition, transgenic mice with different allele modifications can be crossed in order to study crosstalk between oncogenic pathways [52]. While GEMMs are useful in understanding tumorigenesis and developing therapeutics there are some drawbacks to these models. They are time consuming and difficult to generate, and, while murine pathways share some homology to human pathways, they are not a perfect match [31]. Further, a large number of therapies still exhibit a differential response between murine and clinical models [58]. This may be partially due to a lack of control of modification (e.g. achieving full knock-out) of targeted oncogenes. While more advanced methods such as the CRISPR system have been employed for other cancers and for NB cell lines *in vitro*, they have yet to be reported on for NB murine models. In addition, a fundamental problem with many GEMMs is that the mutations are frequently not localized to pathological cells and can impact other cells within the mouse [34].

Table 2.1. Murine GEMM NB models

Mouse Model	Advantages	Limitations	References
TH-MYCN	Representative of high-risk NB, high rate of tumor incidence	Long time for tumor development, few metastasis, limited background strain	[34-43]
LSL-MYCN;Dbh-iCre	Better defined transgene insertion then TH-MYCN, high rate of incidence in multiple background strains	Few metastasis, Limited work with preclinical therapeutic testing	[44]
TH-MYCN/CASP8(KO)	Metastasis, high rate of tumor incidence	Altered ECM structure of primary tumor	[47]
TH-MYCN/Trp53(KI)	Inducible p53 loss	p53 mutation more frequently present in recurrences, survival in mice greatly reduced	[48]
ALK (F1174)	Consistent with NB phenotype	Only present in 10% of NB	[51, 52]
TH-MYCN/ALK(F1174)	High tumor incidence, faster tumor growth	Relevance is limited to <10% patients	[52]
SV40 Tag	Consistent with NB phenotype, high tumor incidence rate, metastasis	All mice die by 28 weeks of age	[54-56]

2.2.2. Syngeneic mouse models

Syngeneic mouse models, also known as allograft tumor models, utilize murine derived tumor cells implanted into a mouse of the same genetic strain. Tumor cells can be removed from GEMMs, used to develop cell lines *in vitro*, then reintroduced into mice of the same strain [59-62]. Tumorigenic cells capable of cell line derivation have been identified in TH-MYCN mice as early as day E13.5 [62]. TH-MYCN tumors from both homozygous and hemizygous mice have been used to develop syngeneic tumors. Whether the mouse was homozygous or hemizygous impacted the cell phenotype, allowing for creation of different tumor lines. Hemizygous tumors gave rise to cell lines which were phenotypically similar to an N-type NB, expressing high levels of MYCN. Homozygous tumors were able to give rise to both cell lines phenotypically comparable those of hemizygous tumors (N-type, high MYCN) and to S-type, adherent NB cells, that exhibited a reduction in MYCN expression [61]. Interestingly, the cell lines derived from hemizygous tumors also displayed reduced tumorigenicity in a syngeneic model, compared to that of the original tumor phenotype. Further, these cell lines contain many genetic changes present in clinical NB, allowing for syngeneic mice to better represent clinical NB. For example, mouse chromosome homologous to human chromosomes 7 and 12 were gained in one cell line, which has been observed in a subset of clinical cases. Gains homologous to chromosomes 1q and 18q were observed frequently in TH-MYCN derived cell lines, further suggesting that molecular and biological features of NB are present in derived murine cell lines [61]. These murine tumor cells can be transplanted into mice of the background strain leaving an intact matched immune system and stroma [59-61].

TH-MYCN derived lines have been transplanted into mice both subcutaneously and orthotopically [59-61]. Injection of tumor lines derived from TH-MYCN tumors (C57Bl/6 background) into C57Bl/6 mice has been used for preclinical testing of immunotherapies [59]. Kroesen et al. demonstrated the relevance of this model for immunotherapy testing due to the tumors expressing similar surface markers profiles (low HLA molecules and presence of NKG2D activating ligand Rae1), and containing a similar resident immune population [59]. In addition to TH-MYCN derived tumors, other tumors derived from murine cell lines such as neuro-2a (spontaneous NB from strain A albino mice, C1300 derived), TBJ (C1300, a strain A/J spontaneous tumor), 9464D (TH-MYCN on a C57Bl/6) and NXS2 (created from C1300 tumors as well) have been engrafted both subcutaneously and orthotopically for testing of immunotherapuetics [63-65]. This included preclinical testing of GD2 targeting immunotherapeutics, both individually and in combination with IL-2, as well as examining the impact on other immune components [59, 60, 65-67].

Syngeneic transplantations of murine cells are advantageous as tumorous cells can be engrafted in mice with a non-genetically modified matching immune system and stroma [59, 60]. Unlike transgenic mouse models, the genetic mutations are confined to the transplanted tumor cells. In addition, there is typically an abundance of cells for transplantation, which allows for large scale therapeutic testing [59]. Further genetic modification of cells *in vitro* can also be performed that either add tumor relevant pathway modifications or add markers to improve cell visualization such as fluorescent or luciferase labels [64, 68, 69]. Potential modifications to cells will be discussed further in the *in vitro* model section. Disadvantages to syngeneic models include inconsistency in tumor engraftment and use of a murine (human homolog) system. Additionally, similar to GEMMs, engrafted tumors are frequently based on a single oncogenic based mutation as compared to the heterogeneity exhibited in clinical tumors [45].

2.2.3. Xenograft models

Human cells have been engrafted into mice for preclinical testing and understanding the mechanisms of NB. Xenograft models can be generated via subcutaneous or orthotopic injection of human NB cells. Tumors developed in these studies are considered advantageous as compared to those that developed in GEMMs or in syngeneic models as they more closely mimic a primary human tumor and are better at predicting clinical response [45]. Use of cell lines with different genetic profiles can allow for formation of tumors with different phenotypes and growth rates [45, 70]. A table of different cell lines commonly xenografted into mice can be found in **Table 2.2**. Additionally, these tumors mimic some of the heterogeneity observed in patient tumors [45]. They are typically easier to generate than tumors generated using primary patient-derived cells, and allow for large scale studies, as cell lines can be scaled up *in vitro* before engraftment. However, they require the use of immunocompromised mice (typically lacking T-cells) for engraftment and survival, which provides a less realistic tumor microenvironment and limits the conclusions that can be made when testing immunotherapies. Both orthotopic and subcutaneous tumors have been used extensively for preclinical testing of therapeutics, including chemotherapy, radiotherapy, small interfering RNA, antisense oligonucleotides and pathway inhibitors as well as drug delivery methods such as nanoparticles and drug loaded scaffolds or films [57, 70-77]. In addition to subcutaneous and orthotopic injection, Seong et al. used intracardiac injection xenograft models to identify NB sub-populations with a higher metastatic potential. Metastatic populations and phenotype differences correlated with genetic changes representing utility for these metastatic cells in identifying new therapeutic targets [78].

Borriello et al. evaluated the impact of the heterogeneous microenvironment. NB cell lines with and without bone marrow-derived mesenchymal stromal cells (BM-MSCs) and cancer-associated fibroblasts (CAFs) taken from NB patients were injected subcutaneously and just below the renal capsule [79]. Engrafted tumors were treated with chemotherapeutics etoposide, etoposide with ruxolitinib (JAK2/STAT3 inhibitor), and trametinib MEK/ERK1/2 (inhibitor). These inhibitors were chosen as CAFs and BM-MSCs have activated STAT3 and ERK1/2 pathways, which contributes to drug resistance. No difference in response to etoposide between NB cells and NB cells with BM-MSCs and CAFs was observed. However, response to etoposide by NB cells and NB cells with BM-MSCs and CAFs was enhanced when combined with ruxolitinib and trametinib. In the NB cell alone tumors, murine CAFs were identified within the tumor, potentially explaining the similarity in response.

While cell lines injected into mice are typically passaged *in vitro*, many studies have shown that traditional *in vitro* culture methods significantly impact the cell genotype and phenotype. This may be due to the cells adapting to the tissue culture environment and the lack of *in vivo* relevant signaling, instead relying on culture medium, with potential adverse effects, specifically related to fetal bovine serum (FBS). FBS is frequently used as a source of hormone factors, essential nutrients, and growth factors needed for a stable growth environment [80]. However, growth with serum has been demonstrated to lead to cellular differentiation and genetic changes, causing the cells to no longer mimic their original clinical phenotype and increasing drug sensitivity [81, 82].

As NB is an orphan disease, a limited number of patient-derived tumor specimens are available. Patient-derived xenografts (PDX) are typically taken directly from patients and passaged by subcutaneously or orthotopically implanting pieces of the primary tumor or previously implanted tumor cells into mice. A list of current PDX tumor cells and suppliers can be found in **Table 2.3**. Passaging the tumor as a xenograft eliminates *in vitro* culture adaptations often observed with sub-cultured lines [83, 84]. Braekeveldt et al. and Stewart et al. demonstrated that

PDX tumor cells orthotopically grown shared molecular characteristics with primary NB cells, retained classic NB markers, and spontaneously metastasized in murine models [83, 84] . Increased infiltration and distant metastasis were observed with orthotopically injected PDX cells as compared to orthotopically injected cell lines. In addition, hallmarks of the microenvironment such as vascular infiltration, CAFs, and tumor-associated macrophages (TAMs) with an M2 phenotype were observed in orthotopic PDX tumors [85]. Continuous xenograft transplantation has also been used to identify genetic changes that tumors undergo during metastasis [86]. Regarding patient-derived tumor cells that need to be propagated *in vitro,* culturing cells without serum and instead with basic fibroblast growth factor, epidermal growth factor, and B27 (generating non-adherent cell lines) was demonstrated to more closely mimic primary cell lines both *in vitro* and *in vivo* [87].

PDX models have been used successfully to evaluate standard of care chemotherapeutics as well as targeted therapeutics [84]. While PDX tumors are the gold standard for xenograft models, there are still many limitations. The time to establish tumors is long and generating enough consistently sized tumors for large scale therapeutic studies is difficult. In addition, PDX cells are injected into immunocompromised mice, limiting their effectiveness for testing of immunotherapies [88]. *In vivo,* PDX cells rely on the mouse microenvironment, which does not completely mimic that of a human, confounding potential stromal interactions [85].

Table 2.2. Frequently used human NB cell lines for preclinical testing

Cell Line	MYCN Status	ALK Mutation	P53 mutation	References
KELLY	Amplified	WT	WT	[70, 89-94]
CHP-212	Amplified	WT	WT	[95, 96]
SKNAS	Non-Amplified	WT	H168R	[95, 97-105]
SH-SY-5Y	Non-Amplified	F1174L	WT	[89, 90, 94, 97, 106-108]
IMR-32	Amplified	WT	WT	[99, 107, 109, 110]
IMR-05	Amplified	WT	WT	[37, 105, 108, 111]
LA-N-5	Amplified	R1275Q	WT	[90, 112, 113]
NB-1	Amplified	WT; Amplified	WT	[114, 115]
SK-N-BE(2)	Amplified	WT	C135F	[152, 160, 166][97, 105, 116]
SK-N-BE(2)-C	Amplified	WT	C135F	[[97]
CHP-134	Amplified	WT	WT	[97, 108, 117, 118]
SK-N-DZ	Amplified	WT	R110L	[101, 103, 104]
NB-1691	Amplified	WT	WT	[102, 119, 120]

Table 2.3. Available NB PDX cell lines and sources

PDX Line	Stage of Tumor	Age of Patient (Yr.M)	MCYN Status	p53 Status	Organization
NB-SD	4	1	Amp	Mut	Pediatric Preclinical Testing Program
NB-1771	4	2.1	Amp	Mut	
NB-1691	4	1.9	Amp	WT	
NB-EBc1	4	2.6	Non Amp	WT	
CHLA-79	4	2	Non Amp	WT	
NB-1643	4	1.7	Amp	WT	
NB-1382	3	3.5	Amp	N/A	
IGR-NB8	3	5.0	Amp	N/A	Insitut Curie
IGR-N835	4	2.0	Amp	N/A	
MAP-IC-A23-NB-1	L2	2.6	Non Amp	N/A	
MAP-GR-B25-NB-1	4	4.0	Amp	N/A	
MAP-GR-A99-NB-1	4	1.10	Amp	N/A	
HSJD-NB-011	4	2.6	Amp	N/A	
SJNBL012407_X1	4	0.1	Amp	N/A	Children's Solid Tumor Network
SJNBL013761_X1	4	3.0	Non Amp	N/A	
SJNBL013762_X1	4	1.3	Amp	N/A	
SJNBL013763_X1	2B	2.0	Amp	N/A	
SJNBL015724_X1	4	2.0	Non Amp	N/A	
SJNBL046_X	4	2.0	Amp	N/A	
SJNBL108_X	4	3.0	Non Amp	N/A	
SJNBL046145_X1	4	2.0	Non Amp	N/A	
SJNBL046148_X1	4	1.11	Amp	N/A	
SJNBL047443_X1	4	12.0	Non Amp	N/A	

PDX-1	4	1.4	Amp	N/A	Lund University
PDX-2	4	2.2	Amp	N/A	
PDX-3	3	2.9	Amp	N/A	
PDX-4	4	4.9	Amp	N/A	
PDX-5	4	2.4	Non Amp	N/A	
PDX-6	2B	12.0	Amp	N/A	
COG-N-415x	Unknown	Unknown	Amp	WT	Children’s Oncology Group
COG-N-440x	Unknown	Unknown	Amp	WT	
COG-N-453x	Unknown	Unknown	Amp	WT	
COG-N-471x	Unknown	Unknown	Amp	WT	
COG-N-496x	Unknown	Unknown	Amp	N/A	
COG-N-519x	Unknown	Unknown	Amp	N/A	
COG-N-534m	Unknown	Unknown	Non Amp	N/A	
COG-N-549x	Unknown	Unknown	Non Amp	N/A	
COG-N-557x	Unknown	Unknown	Amp	N/A	
COG-N-573x	Unknown	Unknown	Amp	N/A	
Felix (COG-N-426)	Unknown	Unknown	Non Amp	N/A	
CHLA-90	4	8	Non Amp	N/A	
CHLA-136	4	3	Amp	N/A	

Amp=Amplified, Mut=Mutation, WT=Wild-type, N/A= Not Available

2.2.4. Xenografted tumors with humanized immune mice

A major limitation of xenograft models is the use of immunocompromised mice and therefore lack of a fully functional immune system. As more immunotherapies are being developed, identification of preclinical models for this testing is critical. Recently, immunodeficient mice with humanized immune systems have emerged as a method to examine xenografted tumor growth with an engrafted human immune system. These humanized mice (HM) are developed to investigate the interactions between tumor cells and immune cells. There are several methods of developing HM, the most basic of which consists of direct injection of human peripheral blood into immunocompromised mice [85]. Alternatively, stromal tissue can be injected alongside tumor tissue, resulting in an active immune population [121]. More commonly, human hematopoietic stem cells and/or precursor cells (CD34+ or CD133+) are injected into the bone marrow of irradiated immunocompromised mice, allowing for generation of immune cells including T cells, B cells, and macrophages [122]. This method is advantageous as a patient’s own marrow or blood could be injected into the mouse, allowing for matching between the immune system and tumor. However, successful use of this method has not been reported yet for NB. While the method of hematopoietic stem cell injection is extremely promising, there are still many components that need to be developed. These models still retain mouse stroma and cytokines, which has the potential to prevent complete immune cell differentiation including T cells and B cells [122]. Furthermore, these models have been shown to exhibit antigen-specific immune responses [123, 124]. The development of accurate humanized mice represents the future for effective pre-clinical therapeutic development.

2.3. Preclinical *in vitro* models

While murine-based systems are the primary method for preclinical testing, advances in tissue culture techniques and *in vitro* systems are promising for creating accurate NB models. Furthermore, the high cost of murine models as well as cross species pathways and microenvironment differences makes accurate, high-throughput screening challenging. *In vitro* models encompass a wide range of systems, including traditional adherent monolayer cells, cells grown in 3D suspension cultures (spheroids), and more complex tissue engineering approaches. In addition, they allow for testing of cell response or cell-cell communication in a more controlled manner (e.g. control of cell confluence, ratio of different cell types, etc.). While *in vitro* systems are already frequently used for screening of therapeutics prior to *in vivo* studies, advances in tissue engineering approaches are creating more accurate models that will be better indicators of clinical responses.

2.3.1. Monolayer co-culture models

The NB tumor microenvironment is composed of multiple cell types including vascular cells, tumor-associated macrophages, fibroblasts, T-cells, natural killer (NK) cells, and others [125]. Each cell type has the potential to influence NB phenotype based on cell-cell interactions, paracrine signaling and secreted factors. Hashimoto et al. co-cultured NB cells with two prominent microenvironment cells, fibroblasts and macrophages. Consistent with clinical results that correlated areas of fibroblasts with aggressive NB phenotype, co-culturing with fibroblasts increased NB cell proliferation [125]. In addition, peripheral blood macrophages were co-cultured with NB cells directly and indirectly using NB cell conditioned medium. Indirect co-culture of macrophages with tumor cell medium transitioned the macrophages into a pro-tumor survival M2 phenotype, or TAM phenotype, suggesting a crosstalk between NB cells and macrophages supporting tumor progression. Indirect co-culture of NB cells macrophage medium increased tumor invasiveness (through a Matrigel based invasion assay) likely through CXCL2 secretion [125]. Direct co-culture of NB cells and macrophages did not result in an increase in NB proliferation; however, it did enhance the invasiveness of NB cells. In co-culture with tumor cells, both macrophages and fibroblasts exhibited and enhanced behavior, suggesting that they are attracted to the tumor site.

Borriello et al. co-cultured NB cells with fibroblasts derived from MSC cells. They observed that fibroblasts induced a pro-tumorigenic effect on NB cells including increased proliferation and inhibited apoptosis [79]. Chemoresistance to therapeutics etoposide and melphalan was evaluated through co-culture of fibroblasts using chemosensitive and chemoresistant NB cell lines. It was determined that co-culturing significantly reduced responsiveness of both the NB cells and the fibroblasts to chemotherapy. This suggests that presence of fibroblasts in the tumor bed contributes to chemoresistance. The authors also determined that these effects do not require cell-to-cell contact but are likely due to soluble factors, many of which have convergent activity in the STAT3 and ERK 1/2 signaling pathways [79].

To evaluate the effect of ECM components on self-organization in co-cultures, Rizvanov et al. co-cultured NB cells with MSCs on different surfaces including poly-l-lysine, fibronectin, gelatin, collagen I, and Matrigel to examine the surface effect on cell phenotype [126]. No phenotypic differences were observed between non-coated surfaces and surfaces coated with poly-l-lysine, fibronectin, gelatin, or collagen I. In these culture conditions, the cells organized into distinct patterns with channels of MSCs and islands of NB cells, comparable to a tumor. However, when cultured on Matrigel, MSCs organized into a dense core with a surrounding ring of NB cells. The authors suggested that this phenotype was more representative of metastatic tumors and could be used as a potential model for metastasis. In addition, exposure of this co-culture model to oxidative stress through the addition of hydrogen peroxide demonstrated that the presence of MSCs resulted in higher NB viability [126]. As oxidative stress is one of the primary death mechanisms of radiation therapy, this finding implies that this culture system is more mimetic of an *in vivo* resistant tumor [126].

For immunotherapy testing, short-term co-culturing is performed with NK cells. Co-culture of NB and NK cells are frequently used as part of an antibody-dependent cell-mediated cytotoxicity assay for testing of immunotherapies. The NK cells induce lysis of NB cells in the presence of antibodies [127]. Similar studies have been carried out to test therapeutic efficacy with leukocytes, peripheral blood mononuclear cells, and granulocytes [128, 129]. In addition, these systems have been used to test out combination therapies of cytokines or retinoids with immunotherapies [130, 131]. However, there has been little work done with longer-term culture of these immune cell populations and characterization of the impact of co-culture on tumor cells and immune cells. As immune cells are present in NB tumors, further development of these co-culture models may be critical to developing better therapeutic strategies.

NB cells have also been cultured with hepatocytes, as NB frequently metastasizes to the liver [132, 133]. The authors observed resistance to apoptosis by the NB cells, induction of apoptosis in the hepatocytes, and an increase in VEGF secretion. The hepatocytes induced NB cells to overexpress Bcl-2, thereby reducing NB apoptosis and establishing Bcl-2 as a therapeutic target for NB liver metastasis. Interestingly, studies focusing on VEGF secretion demonstrated that expression of VEGF receptors is highly heterogeneous across NB lines, which likely extends to patient tumors [132]. It is therefore critical to examine the expression of each individual tumor when investigating the use of anti-VEGF therapies [132, 133].

Co-culture systems also enable the investigation of cell migration in the presence of other cell types, as commonly evaluated using transwell plates. NB cells in transwell systems have primarily been used to examine the impact of NB cells on migration of human umbilical vein endothelial cells (HUVECs). NB cell expression of MYCN induced HUVEC migration proportionately. In addition, it was demonstrated that efficacy of a PI3K inhibitor NVP-BEZ235 (as angiogenesis is regulated by PI3K) was dependent on MYCN. This suggests that a link between angiogenesis, the PI3K pathway, and MYCN in NB [134]. Additional studies have demonstrated that growth of HUVECs in medium conditioned by NB cells induced vessel angiogenesis and upregulation of VEGF and IL-8 [135].

Co-culturing NB cells with other cell types present within the tumor microenvironment such as fibroblasts and immune cells as well as cells present at metastatic sites allows for understanding of the impact of tumor microenvironment on NB phenotype [125]. These culture systems allow for an increase in understanding of tumor heterogeneity as well as critical tumor signaling pathways. For preclinical therapeutic testing, this provides an opportunity to better understand tumor escape as mediated by signaling factors secreted from neighboring cells and how therapies influence non-tumor cells. Incorporating additional microenvironment stress components, including hypoxia and mechanics, would add additional complexity and relevance for drug development.

2.3.2. 3D in vitro models: Spheroid

Growth of NB cells in spheroids has been used as a preclinical model, as it has been shown to more accurately mimic the clinical phenotype and response to therapeutics [83, 85, 87]. NB spheroid cultures can be generated by using low or non-attachment culture dishes, coated plates or dishes, or the removal of serum from the medium [136-139]. Comparing cells grown in monolayer culture to spheroids, spheroid cultures exhibited increased expression of metabolic markers, cell stress response proteins, cell structure proteins, and transport polypeptides [49]. Sidarovich et al. used spheroids for high throughput drug screening of over 300 FDA-approved anti-cancer compounds or compounds undergoing clinical trials [140]. From this screen, the authors identified, and later evaluated *in vivo*, two different compounds (ponatinib and axitinib) as potential new therapies for NB based on toxicity, molecular target, and side effects [140].

Spheroids are advantageous as once they reached a critical size of >100 µm, they begin to exhibit microenvironment changes due to nutrient and oxygen gradients, as well as spatial organization of cells that more closely mimic the *in vivo* tumor microenvironment [138]. Changes in nutrient and oxygen gradients induce therapeutic resistance through upregulation of pro-survival and tumor promoting pathways [138]. Growth of NB cell lines and patient-derived tumor cells as non-adherent spheroids demonstrated retention of cellular phenotype more closely resembling primary tumors [83, 85, 87]. Additional advantages of spheroids include altered diffusion and ECM deposition that impacts therapeutic efficacy, often increasing the necessary effective concentration [136].

Culturing as spheroids demonstrated selectively for tumor-initiating cells [141]. Coulon et al. evaluated spheroid formation of serially passaged PDXs and found that only the bone marrow-derived metastatic cells (the patient equivalent of stage 4) were able to generate spheroids suggesting that the metastatic cells have a high degree of self-renewal and that this subset of cells is likely enriched with a cancer stem cell population [142]. This is important as it allows spheroids to be used to test therapies that target pathway changes associated with tumor stem cells such as Notch and WNT [143, 144]. Regarding cellular phenotype and spheroid formation, MYCN amplified tumor cells exhibit a higher propensity for spheroid formation then non-MYCN amplified cells [142]. The ability to form spheroids is directly dependent on cellular differentiation status, or stemness. Treatment with 13-*cis*-retinoic acid, a differentiation agent that induces a neuronal phenotype, inhibited spheroid formation [145].

Gransbury et al. fabricated spheroids of different diameters (ranging from 50-800 microns) to evaluate different microenvironments [138]. Using the spheroid culture, the authors were able to examine different levels of hypoxia, diffusion, and redox state, giving them further insights into therapeutic potential than otherwise possible with 2D culture models [138]. Two different cancer therapies were identified: NAMI-A and KP1019 which are Ru^{III}-based anti-metastatic and cytotoxic drugs that are administered in a non-active form and subsequently become activated under oxidative environments. Cuperus et al. used spheroid cultures to study fenretinide, which has been shown to induce apoptosis through retinoic acid and reactive oxygen species dependent pathways [146]. In combination with buthionine sulfoximine, an inhibitor of glutathione synthesis, fenretinide reduced proliferation and induced apoptosis both in monolayer and in spheroids.

Spheroid culture systems have been used to model drug diffusion challenges and develop drug delivery systems with improved tumor penetration. Sagnella et al. used spheroid culture of NB to evaluate the therapeutic potential of EDV^{TM} nanocells – a bacterially-derived drug delivery system consisting of nonviable cells that are ~ 400 nm in diameter. The authors demonstrated that the EGFR-targeted nanocells enhanced penetrance of doxorubicin compared to non-targeted doxorubicin loaded nanocells and doxorubicin without a delivery vehicle, resulting in increased apoptosis. These findings were confirmed in an orthotopic xenograft model [147]. Spheroids have also been used to evaluate radiotherapy cytotoxic agents and relavent pathway inhibitors such as multikinase inhibitors, Betulinic acid, and oxidative phosphorylation inhibitors [148-151].

Spheroid cultures are an important part of preclinical testing. They are currently the most widely used approach to bridge the gap between two-dimensional cell culture and the *in vivo* tumor microenvironment [139]. Growth in spheroids exhibits phenotypes better resembling *in vivo* tumors [88]. In addition to a higher degree of mimicry to *in vivo* tumors, spheroids are advantageous as they allow for rapid preclinical testing [139]. They also exhibit cell-cell contact similar to that of an *in vivo* tumor and exhibit similar diffusion limitations for nutrients and therapeutics [83, 85, 87]. Limitations to spheroid tumors include heterogeneity in sizes, a necrotic core in large spheroids, and lack of additional environmental components such the stroma and immune cells [152, 153]. Non-uniform spheroid generation results in varying diffusion gradients, making controlled experimentation challenging. Frequently tumors *in vivo* exhibit a hypoxic core, with the necrotic cells secreting factors which induce angiogenesis, thus preventing the tumors from becoming overly necrotic. Angiogenesis does not occur without a vascular component in the spheroid cultures, so care must be taken to avoid large regions of necrosis. Stroma and immune cells are critical components of the tumor microenvironment and can impact oncogenic pathways and therapeutic efficacy. Co-culture of NB cells with stroma and immune components, as performed for other cancer types, in spheroids present a unique opportunity to mimic the tumor microenvironment [154-157].

2.3.3. Hydrogels and scaffolds for 3D tumor growth

Limited work has been done with NB growth in 3D outside of spheroid cultures. However, 3D growth of NB cells can be achieved using a broad range of scaffold and/or hydrogel materials. ECM hydrogels such as collagen I and Matrigel have been used to mimic tumor ECM and provide a backbone for 3D tumor growth. These 3D matrices have the potential to impact gene expression and cell morphology [158]. Li et al. used microarray analysis to demonstrate differences in gene expression in cells grown in monolayer, collagen I hydrogels, and Matrigel hydrogels [158]. All 3D culture conditions induced morphological differences as compared to monolayer. Cells grown in collagen I exhibited longer neurites then those grown in Matrigel, likely due to the fibrils present in the collagen. This study focused on genes associated with morphology and neurite outgrowth; studies evaluating impact on key NB tumor pathways have not been performed.

Mitchell et al., used spheroids embedded in collagen hydrogels to evaluate the invasive behavior of NB. Mixed cellular population of NB cells, neuronal type NB cells and stromal type NB cells, exhibited a heterogeneous invasive population. Crosstalk between both cell types was identified where neuronal type NB cells decreased invasion of stromal type NB cells and stromal type NB cells enhanced invasion in neuronal types NB cells [159]. This could be useful in identifying which cell populations to target therapeutically to decrease metastasis.

Studies have suggested the presence of ECM molecules as well as growth in 3D can impact responsiveness to therapeutics [160]. Mitchell et al., also evaluated siRNA-targeting Rac on both single cell suspensions and cells suspended in 3D collagen hydrogels. Cell lines with different morphologies, stromal, neuronal, or the combination, were evaluated. As Rac inhibition is most effective in cells with elongated, invasive morphology, studies in 3D were critical to identifying the differences in invasion and morphology for determining therapeutic efficacy [160].

Non-hydrogel-based scaffolds typically consist of porous or fibrous materials, either synthetic or biological-derived, that can be used to mimic structures present *in vi*vo. They are advantageous as they have tunable degradation (based on material properties or material choice), can be functionalized to mimic the native environment, and provide control over spatial organization. Scaffolded approached have been used for the modeling of other cancer types but limited scaffolded work has been done with NB cell lines. Curtin et al. used lyophilized collagen I/glycosaminoglycan and collagen I/nanohydroxyapatite scaffolds for culturing of KELLY NB cells and a cisplatin-resistant KELLY cell derivative [161]. Collagen/glycosaminoglycan and collagen/nanohydroxyapatite were chosen as glycosaminoglycans such as hyaluronic acid are typically found in the tumor ECM and NB frequently metastasizes to the bone, which contains a high content of hydroxyapatite. Consistent with results of other cancer cells grown in 3D, the NB cells exhibited reduced cellular growth rate in 3D [162, 163]. Interestingly, the cisplatin-resistant cell line exhibited increased proliferation in the collagen/hydroxyapatite scaffold. Response to cisplatin was evaluated in monolayer, 3D culture, and an in an orthotopic xenograft model. Both 3D culture systems exhibited similar chemosensitivity to the orthotopic *in vivo* model, with a reduced response observed as compared to the monolayer culture. Using these scaffolds, KELLY NB cells grown in 2D and 3D were used for evaluation of liposomes delivering miRNA for therapeutic gene silencing [161]. Unlike the chemotherapy studies, the miRNA exhibited similar effects in 2D and 3D highlighting the potential usefulness of miRNA as a therapeutic.

Scaffold based studies have also been used for biomechanical modeling. One scaffold-based study used graphene-augmented nanofiber scaffolds to determine the impact of an “out-of-comfort” nanobiomechanical environment for NB cells [164]. Growth on highly aligned graphene fibers changed the morphology from flat to be more rounded in shape as the cells enveloped the fibers. In addition, increased gene expression of pro-migratory and pro-invasion markers was observed [164]. This represents a potential system to examine the more migratory or more metastatic like NB cells, and develop therapeutics aimed at effectively inhibiting those cells.

3D scaffold-based modeling has been explored for other pediatric blastoma and similar pediatric cancers. For example, polymeric poly(lactide-co-glycolide) nanoparticles have been used to generate 3D cultures of retinoblastoma cells. When exposed to etoposide and doxorubicin loaded nanoparticles, cells in 2D exhibited a higher reduction in proliferation then those in 3D. The authors correlated this to a decreased drug uptake in cells grown in 3D as compared to 2D, likely due to diffusion barriers [165]. Electrospun poly(ε-caprolactone) microfiber scaffolds have been used to generate models of Ewing sarcoma [166]. Using these models, cells grown in microfiber scaffolds exhibited reduced proliferation as compared to 2D cultured cells. Cell growth on the microfiber scaffold was comparable to xenograft growth, as was levels of relevant pathways such as IGF-1R signaling and mTor [166]. Ewing sarcoma cell lines and PDX cells have been grown on a porous matrix composed of freeze-dried type I collagen and hyaluronic acid meant to mimic both mechanical and biologic cues present in the body. Both the Ewing sarcoma cell lines and PDX cells demonstrated increased drug resistance and closer resemblance of *in vivo* tumors [167]. Scaffold-based approaches could be applied for preclinical NB modeling. These approaches are advantageous as scaffolds can be fabricated from materials that mimic the native tumor ECM (both chemically and mechanically). In addition, layered scaffold models with multiple cell types can be used to model different components of the tumor architecture.

2.3.4. 3D co-culture models

3D models can be expanded to include multiple different cell types found in the tumor microenvironment. Villasante et al. used a tissue engineered model consisting of sheets of HUVEC cells and NB cells stacked to reach a total height of ~100 µm placed on a “vascular bed” made of collagen, fibrin, and HUVEC cells. The stacked vascular bed was placed on a collagen gel with microchannels to mimic vessel-like structures within NB [168]. This system was cultured in a perfusion bioreactor to mimic the *in vivo* environment. The therapeutic potential of isotretinoin was evaluated using this model. Isotretinoin blocks cell proliferation and reduces tumor vasculature *in vivo*. Isotretinoin increased cellular apoptosis, and decreased mRNA levels of NB markers MYCN and GLI1. In addition, isotretinoin weakened and disassembled the vascular networks by blocking cell-to-cell adhesions. Resistant populations of both cancer cells and vascular cells to isotretinoin were identified. Further characterization of resistant cells identified an increase in SOX2 expression in the resistant population. This correlation had not previously been identified using conventional 2D culture [168].

NB cells and MSCs have been co-encapsulated inside collagen I microspheres to investigate the impact of the stromal environment on NB growth [169]. The MSCs were used as they exhibited a fibroblast like morphology, resembling CAFs *in vivo*. The MSCs induced increased NB proliferation, suggesting that the stromal component has a direct impact on tumor growth. The cultured NB cells and MSCs exhibited a rosette like phenotype, resembling that of clinical NB. MMP9-expressing cells were found primarily on the periphery of the microspheres, the more migratory region. Previous work with these microspheres identified a hypoxic core, which could be evaluated with the NB model to mimic the hypoxic core frequently found in clinical NB tumors [170].

Multicellular models grown in 3D are an emerging trend in tissue engineering to attempt to understand the complex tumor microenvironment. This remains largely unexplored for NB; however, preliminary studies suggest that it can provide insightful information about tumor pathway crosstalk and potential therapeutic efficacy. The heterogeneity in NB, both within the tumor microenvironment and across individual tumors represents a challenge for effective therapeutic development. *In vitro* 3D culture of NB cells and relevant microenvironment cells would allow for elucidation of critical pathways and mechanisms of resistance that mimic those *in vivo*.

2.3.5. Monolayer *in vitro* systems

Traditional *in vitro* models consist of commercially available or lab-derived cell lines adherent to polystyrene dishes, typically grown in the presence of fetal bovine serum, nutrients, and antibiotics. Monolayer culturing is the most common method of evaluating therapeutic efficacy, primarily due to the higher number of cells that can be generated, allowing for rapid screening of many compounds. In addition, these cells can be modified at the genetic level to evaluate the impact of pathway changes on therapeutic efficacy. Methods of inducing gene changes, including transfection, transduction, and more recently use of CRISPR systems, have been previously reviewed [171-173]. Genes that have been identified as potential mediators in NB pathways can then be evaluated through knockdown, overexpression, or direct targeting using pathway inhibitors.

MYCN-amplified cell lines have been useful in identifying many proteins and genes that either contribute to or are associated with MYCN. Park et al. determined that high expression of protein arginine methyltransferase 5 (PRMT5) was strongly associated with MYCN amplification. Use of short-interfering RNA to reduce expression of PRMT5 decreased MYCN expression as well as cell death in MYCN-amplified cell lines [174]. Ambrosio et al. identified lysine-specific demethylase 1 (LSD1), a histone modifier, as a transcriptional modulator of NDRG1 (N-Myc Downstream-Regulated Gene 1, a metastasis suppressor). In both *in vitro* models and patient samples, high levels of LSD1 correlated with low levels of NDRG1 [175].

RNAi and CRISPR screens have been useful in identifying genes that could be targets for therapeutic regimes. In a kinome-wide RNAi screen, Shen et al. targeted protein kinases and kinase associated genes to identify sensitizing and inhibitory kinases to HDAC8 inhibitors. Knockdown of ALK sensitized NB cells to HDAC8 inhibitors, and combinatory treatment of NB tumors with crizotinib, an ALK inhibitor, and HDAC8 inhibitors increased cell death [176]. CRISPR-Cas9 screening of MYCN-amplified NB cells by Chen et al. demonstrated cell dependency on the PRCR2 complex, specifically EZH2. MYCN binds at the EZH2 promoter, repressing neuronal differentiaton of NB cells, which promotes a more tumorigenic phenotype. This was further confirmed through genetic and pharmacological suppression of EZH2, which inhibited NB growth. Screens such as these are useful in identifying key pathways that could be therapeutically targeted in NB [177].

In addition to screening through genetic modifications, screens of high numbers of cell lines and therapies can be conducted *in vitro*. Mahoney et al. screened 482 cell lines with metabolic inhibitors [178]. Neuroendocrine cells, specifically NB cells, showed a higher sensitivity to NB-598, an inhibitor of enzyme squalene epoxidase (SQLE). This suggests that targeting of this pathway may have therapeutic potential. Similarly, Michaelis et al. screened 321 cancer cell lines (from 26 different types of cancer) for response to flubendazole (an inhibitor of microtubule function) [179]. NB was identified as highly sensitive to flubendazole, reducing viability of 140 NB cells lines. Large scale screens such as these have the potential to identify novel therapeutics for NB.

2.4. Conclusions

Neuroblastoma is a heterogeneous disease both in clinical presentation and prognosis. Understanding of critical pathways in disease progression and development of effective preclinical therapies remains a challenge. Murine models, including GEMM, syngeneic, and xenograft have been developed for therapeutic testing, particularly geared towards mimicking high-risk phenotypes. However, challenges remain as therapeutic development trends toward immunotherapies and a mouse capable of combining a human NB tumor with an intact immune system has not been created. The future of this likely lies within humanized immune mouse models which have the potential to use a mouse as a vehicle to evaluate a human tumor, with an intact human immune system.

Tissue engineering represents a promising approach for development of systems capable of high throughput therapeutic evaluation using multicellular systems. The growth of cells in 3D allows for diffusion gradients of nutrients, oxygen, and therapeutics similar to those found *in vivo*. For development of effective models, it is critical to incorporate multiple cell types (stromal, vascular, and immune) in an environment capable of mimicking relevant diffusion limitations. Patient derived tumors are the most representative of the heterogeneous tumor phenotype. In the future, combining patient tumors with patient-derived stroma and immune cells may achieve a more accurate model for preclinical therapeutic testing.

2.5. References

[1] G.M. Brodeur, A. Nakagawara, Molecular basis of clinical heterogeneity in neuroblastoma, Am J Pediatr Hematol Oncol 14(2) (1992) 111-6.
[2] S.M. Ries LAG, Gurney JG, Linet M, Tamra T, Young JL, Bunin GR (eds), Cancer Incidence and Survival among Children and Adolescents: United States SEER Program 1975-1995, National Cancer Institute, SEER Program NIH Pub. No. 99-4649. Bethesda, MD, (1999).
[3] C.A. Stiller, D.M. Parkin, International variations in the incidence of neuroblastoma, Int J Cancer 52(4) (1992) 538-43.
[4] K.K. Matthay, J.G. Villablanca, R.C. Seeger, D.O. Stram, R.E. Harris, N.K. Ramsay, P. Swift, H. Shimada, C.T. Black, et al., Treatment of high-risk neuroblastoma with intensive chemotherapy, radiotherapy, autologous bone marrow transplantation, and 13-cis-retinoic acid. Children's Cancer Group, N Engl J Med 341(16) (1999) 1165-73.
[5] S.G. DuBois, Y. Kalika, J.N. Lukens, G.M. Brodeur, R.C. Seeger, J.B. Atkinson, G.M. Haase, C.T. Black, C. Perez, et al., Metastatic sites in stage IV and IVS neuroblastoma correlate with age, tumor biology, and survival, J Pediat Hematol Onc 21(3) (1999) 181-9.
[6] D.A. Morgenstern, W.B. London, D. Stephens, S.L. Volchenboum, T. Simon, A. Nakagawara, H. Shimada, G. Schleiermacher, K.K. Matthay, et al., Prognostic significance of pattern and burden of metastatic disease in patients with stage 4 neuroblastoma: A study from the International Neuroblastoma Risk Group database, Eur J Cancer 65 (2016) 1-10.
[7] T. Shojaei-Brosseau, A. Chompret, A. Abel, F. de Vathaire, M.A. Raquin, L. Brugieres, J. Feunteun, O. Hartmann, C. Bonaiti-Pellie, Genetic epidemiology of neuroblastoma: a study of 426 cases at the Institut Gustave-Roussy in France, Pediatr Blood Cancer 42(1) (2004) 99-105.
[8] R.C. Seeger, G.M. Brodeur, H. Sather, A. Dalton, S.E. Siegel, K.Y. Wong, D. Hammond, Association of multiple copies of the N-myc oncogene with rapid progression of neuroblastomas, N Engl J Med 313(18) (1985) 1111-6.
[9] G.M. Brodeur, R.C. Seeger, M. Schwab, H.E. Varmus, J.M. Bishop, Amplification of N-myc in untreated human neuroblastomas correlates with advanced disease stage, Science 224(4653) (1984) 1121-4.
[10] T. Martinsson, R.M. Sjoberg, F. Hedborg, P. Kogner, Deletion of chromosome 1p loci and microsatellite instability in neuroblastomas analyzed with short-tandem repeat polymorphisms, Cancer Res 55(23) (1995) 5681-6.
[11] P.S. White, P.M. Thompson, T. Gotoh, E.R. Okawa, J. Igarashi, M. Kok, C. Winter, S.G. Gregory, M.D. Hogarty, et al., Definition and characterization of a region of 1p36.3 consistently deleted in neuroblastoma, Oncogene 24(16) (2005) 2684-94.
[12] P.S. White, P.M. Thompson, B.A. Seifried, E.P. Sulman, S.J. Jensen, C. Guo, J.M. Maris, M.D. Hogarty, C. Allen, et al., Detailed molecular analysis of 1p36 in neuroblastoma, Med Pediatr Oncol 36(1) (2001) 37-41.
[13] D. Plantaz, J. Vandesompele, N. Van Roy, M. Lastowska, N. Bown, V. Combaret, M.C. Favrot, O. Delattre, J. Michon, et al., Comparative genomic hybridization (CGH) analysis of stage 4 neuroblastoma reveals high frequency of 11q deletion in tumors lacking MYCN amplification, Int J Cancer 91(5) (2001) 680-6.
[14] R. Spitz, B. Hero, K. Ernestus, F. Berthold, Deletions in chromosome arms 3p and 11q are new prognostic markers in localized and 4s neuroblastoma, Clin Cancer Res 9(1) (2003) 52-8.
[15] C.A. Perez, K.K. Matthay, J.B. Atkinson, R.C. Seeger, H. Shimada, G.M. Haase, D.O. Stram, R.B. Gerbing, J.N. Lukens, Biologic variables in the outcome of stages I and II neuroblastoma

treated with surgery as primary therapy: a children's cancer group study, J Clin Oncol 18(1) (2000) 18-26.

[16] D.R. Strother, W.B. London, M.L. Schmidt, G.M. Brodeur, H. Shimada, P. Thorner, M.H. Collins, E. Tagge, S. Adkins, et al., Outcome After Surgery Alone or With Restricted Use of Chemotherapy for Patients With Low-Risk Neuroblastoma: Results of Children's Oncology Group Study P9641, J Clin Oncol 30(15) (2012) 1842-1848.

[17] B.H. Kushner, N.K. Cheung, M.P. LaQuaglia, P.F. Ambros, I.M. Ambros, M.A. Bonilla, W.L. Gerald, M. Ladanyi, F. Gilbert, et al., Survival from locally invasive or widespread neuroblastoma without cytotoxic therapy, J Clin Oncol 14(2) (1996) 373-81.

[18] A.D. Pearson, C.R. Pinkerton, I.J. Lewis, J. Imeson, C. Ellershaw, D. Machin, G. European Neuroblastoma Study, C. Children's, G. Leukaemia, High-dose rapid and standard induction chemotherapy for patients aged over 1 year with stage 4 neuroblastoma: a randomised trial, Lancet Oncol 9(3) (2008) 247-56.

[19] N.K. Cheung, B.H. Kushner, M. LaQuaglia, K. Kramer, S. Gollamudi, G. Heller, W. Gerald, S. Yeh, R. Finn, et al., N7: a novel multi-modality therapy of high risk neuroblastoma (NB) in children diagnosed over 1 year of age, Med Pediatr Oncol 36(1) (2001) 227-30.

[20] F. Berthold, J. Boos, S. Burdach, R. Erttmann, G. Henze, J. Hermann, T. Klingebiel, B. Kremens, F.H. Schilling, et al., Myeloablative megatherapy with autologous stem-cell rescue versus oral maintenance chemotherapy as consolidation treatment in patients with high-risk neuroblastoma: a randomised controlled trial, Lancet Oncol 6(9) (2005) 649-58.

[21] A. Langler, A. Christaras, K. Abshagen, K. Krauth, B. Hero, F. Berthold, Topotecan in the treatment of refractory neuroblastoma and other malignant tumors in childhood - a phase-II-study, Klin Padiatr 214(4) (2002) 153-6.

[22] G.A. Wiseman, L.K. Kvols, Therapy of neuroendocrine tumors with radiolabeled MIBG and somatostatin analogues, Semin Nucl Med 25(3) (1995) 272-8.

[23] E. Wassberg, S. Pahlman, J.E. Westlin, R. Christofferson, The angiogenesis inhibitor TNP-470 reduces the growth rate of human neuroblastoma in nude rats, Pediatr Res 41(3) (1997) 327-33.

[24] G. Klement, S. Baruchel, J. Rak, S. Man, K. Clark, D.J. Hicklin, P. Bohlen, R.S. Kerbel, Continuous low-dose therapy with vinblastine and VEGF receptor-2 antibody induces sustained tumor regression without overt toxicity, J Clin Invest 105(8) (2000) R15-24.

[25] A.E. Evans, K.D. Kisselbach, X. Liu, A. Eggert, N. Ikegaki, A.M. Camoratto, C. Dionne, G.M. Brodeur, Effect of CEP-751 (KT-6587) on neuroblastoma xenografts expressing TrkB, Med Pediatr Oncol 36(1) (2001) 181-4.

[26] R. Ho, J.E. Minturn, T. Hishiki, H. Zhao, Q. Wang, A. Cnaan, J. Maris, A.E. Evans, G.M. Brodeur, Proliferation of human neuroblastomas mediated by the epidermal growth factor receptor, Cancer Res 65(21) (2005) 9868-75.

[27] A.L. Yu, M.M. Uttenreuther-Fischer, C.S. Huang, C.C. Tsui, S.D. Gillies, R.A. Reisfeld, F.H. Kung, Phase I trial of a human-mouse chimeric anti-disialoganglioside monoclonal antibody ch14.18 in patients with refractory neuroblastoma and osteosarcoma, J Clin Oncol 16(6) (1998) 2169-80.

[28] S. Gonzalez, A. Naranjo, L.M. Serrano, W.C. Chang, C.L. Wright, M.C. Jensen, Genetic engineering of cytolytic T lymphocytes for adoptive T-cell therapy of neuroblastoma, J Gene Med 6(6) (2004) 704-11.

[29] E. Bolesta, A. Kowalczyk, A. Wierzbicki, P. Rotkiewicz, B. Bambach, C.Y. Tsao, I. Horwacik, A. Kolinski, H. Rokita, et al., DNA vaccine expressing the mimotope of GD2

ganglioside induces protective GD2 cross-reactive antibody responses, Cancer Res 65(8) (2005) 3410-8.

[30] S. Ackermann, M. Cartolano, B. Hero, A. Welte, Y. Kahlert, A. Roderwieser, C. Bartenhagen, E. Walter, J. Gecht, et al., A mechanistic classification of clinical phenotypes in neuroblastoma, Science 362(6419) (2018) 1165-1170.

[31] C. Mouse Genome Sequencing, R.H. Waterston, K. Lindblad-Toh, E. Birney, J. Rogers, J.F. Abril, P. Agarwal, R. Agarwala, R. Ainscough, et al., Initial sequencing and comparative analysis of the mouse genome, Nature 420(6915) (2002) 520-62.

[32] J.C. Walrath, J.J. Hawes, T. Van Dyke, K.M. Reilly, Genetically engineered mouse models in cancer research, Adv Cancer Res 106 (2010) 113-64.

[33] C.S. Branda, S.M. Dymecki, Talking about a revolution: The impact of site-specific recombinases on genetic analyses in mice, Dev Cell 6(1) (2004) 7-28.

[34] W.A. Weiss, K. Aldape, G. Mohapatra, B.G. Feuerstein, J.M. Bishop, Targeted expression of MYCN causes neuroblastoma in transgenic mice, Embo J 16(11) (1997) 2985-2995.

[35] L. Chesler, D.D. Goldenberg, I.T. Seales, R. Satchi-Fainaro, M. Grimmer, R. Collins, C. Struett, K.N. Nguyen, G. Kim, et al., Malignant progression and blockade of angiogenesis in a murine transgenic model of neuroblastoma, Cancer Res 67(19) (2007) 9435-9442.

[36] C.A. Burkhart, F. Watt, J. Murray, M. Pajic, A. Prokvolit, C. Xue, C. Flemming, J. Smith, A. Purmal, et al., Small-molecule multidrug resistance-associated protein 1 inhibitor reversan increases the therapeutic index of chemotherapy in mouse models of neuroblastoma, Cancer Res 69(16) (2009) 6573-80.

[37] A. Henssen, K. Althoff, A. Odersky, A. Beckers, R. Koche, F. Speleman, S. Schafers, E. Bell, M. Nortmeyer, et al., Targeting MYCN-Driven Transcription By BET-Bromodomain Inhibition, Clin Cancer Res 22(10) (2016) 2470-81.

[38] E. Chipumuro, E. Marco, C.L. Christensen, N. Kwiatkowski, T. Zhang, C.M. Hatheway, B.J. Abraham, B. Sharma, C. Yeung, et al., CDK7 inhibition suppresses super-enhancer-linked oncogenic transcription in MYCN-driven cancer, Cell 159(5) (2014) 1126-1139.

[39] V. Colicchia, M. Petroni, G. Guarguaglini, F. Sardina, M. Sahun-Roncero, M. Carbonari, B. Ricci, C. Heil, C. Capalbo, et al., PARP inhibitors enhance replication stress and cause mitotic catastrophe in MYCN-dependent neuroblastoma, Oncogene 36(33) (2017) 4682-4691.

[40] J. Lu, S. Guan, Y. Zhao, Y. Yu, S.E. Woodfield, H. Zhang, K.L. Yang, S. Bieerkehazhi, L. Qi, et al., The second-generation ALK inhibitor alectinib effectively induces apoptosis in human neuroblastoma cells and inhibits tumor growth in a TH-MYCN transgenic neuroblastoma mouse model, Cancer Lett 400 (2017) 61-68.

[41] K. Waldeck, C. Cullinane, K. Ardley, J. Shortt, B. Martin, R.W. Tothill, J. Li, R.W. Johnstone, G.A. McArthur, et al., Long term, continuous exposure to panobinostat induces terminal differentiation and long term survival in the TH-MYCN neuroblastoma mouse model, Int J Cancer 139(1) (2016) 194-204.

[42] M.E.M. Dolman, E. Poon, M.E. Ebus, I.J.M. den Hartog, C.J.M. van Noesel, Y. Jamin, A. Hallsworth, S.P. Robinson, K. Petrie, et al., Cyclin-Dependent Kinase Inhibitor AT7519 as a Potential Drug for MYCN-Dependent Neuroblastoma, Clin Cancer Res 21(22) (2015) 5100-5109.

[43] Z.H. Chen, Z.Y. Wang, J.C. Pang, Y. Yu, S. Bieerkehazhi, J.X. Lu, T. Hu, Y.L. Zhao, X. Xu, et al., Multiple CDK inhibitor dinaciclib suppresses neuroblastoma growth via inhibiting CDK2 and CDK9 activity, Sci Rep-Uk 6 (2016).

[44] Y. Mao, N. Eissler, K.L. Blanc, J.I. Johnsen, P. Kogner, R. Kiessling, Targeting Suppressive Myeloid Cells Potentiates Checkpoint Inhibitors to Control Spontaneous Neuroblastoma, Clin Cancer Res 22(15) (2016) 3849-59.
[45] T. Teitz, J.J. Stanke, S. Federico, C.L. Bradley, R. Brennan, J.K. Zhang, M.D. Johnson, J. Sedlacik, M. Inoue, et al., Preclinical Models for Neuroblastoma: Establishing a Baseline for Treatment, Plos One 6(4) (2011).
[46] K. Althoff, A. Beckers, E. Bell, M. Nortmeyer, T. Thor, A. Sprussel, S. Lindner, K. De Preter, A. Florin, et al., A Cre-conditional MYCN-driven neuroblastoma mouse model as an improved tool for preclinical studies, Oncogene 34(26) (2015) 3357-3368.
[47] T. Teitz, M. Inoue, M.B. Valentine, K.J. Zhu, J.E. Rehg, W. Zhao, D. Finkelstein, Y.D. Wang, M.D. Johnson, et al., Th-MYCN Mice with Caspase-8 Deficiency Develop Advanced Neuroblastoma with Bone Marrow Metastasis, Cancer Res 73(13) (2013) 4086-4097.
[48] O. Yogev, K. Barker, A. Sikka, G.S. Almeida, A. Hallsworth, L.M. Smith, Y. Jamin, R. Ruddle, A. Koers, et al., p53 Loss in MYC-Driven Neuroblastoma Leads to Metabolic Adaptations Supporting Radioresistance, Cancer Res 76(10) (2016) 3025-3035.
[49] H.R. Kumar, X. Zhong, D.J. Hoelz, F.J. Rescorla, R.J. Hickey, L.H. Malkas, J.A. Sandoval, Three-dimensional neuroblastoma cell culture: proteomic analysis between monolayer and multicellular tumor spheroids, Pediatr Surg Int 24(11) (2008) 1229-34.
[50] N. Javanmardi, S. Fransson, A. Djos, R.M. Sjoberg, S. Nilsson, K. Truve, P. Kogner, T. Martinsson, Low Frequency ALK Hotspots Mutations In Neuroblastoma Tumours Detected By Ultra-deep Sequencing: Implications For ALK Inhibitor Treatment, Sci Rep-Uk 9(1) (2019) 2199.
[51] L.C. Heukamp, T. Thor, A. Schramm, K. De Preter, C. Kumps, B. De Wilde, A. Odersky, M. Peifer, S. Lindner, et al., Targeted Expression of Mutated ALK Induces Neuroblastoma in Transgenic Mice, Sci Transl Med 4(141) (2012).
[52] T. Berry, W. Luther, N. Bhatnagar, Y. Jamin, E. Poon, T. Sanda, D. Pei, B. Sharma, W.R. Vetharoy, et al., The ALK(F1174L) Mutation Potentiates the Oncogenic Activity of MYCN in Neuroblastoma, Cancer Cell 22(1) (2012) 117-130.
[53] C.S. Alvarado, W.B. London, A.T. Look, G.M. Brodeur, D.H. Altmiller, P.S. Thorner, V.V. Joshi, S.T. Rowe, M.B. Nash, et al., Natural history and biology of stage A neuroblastoma: a Pediatric Oncology Group Study, J Pediat Hematol Onc 22(3) (2000) 197-205.
[54] H. Iwakura, H. Ariyasu, N. Kanamoto, K. Hosod, K. Naka, K. Kangawa, T. Akamizu, Establishment of a novel neuroblastoma mouse model, Int J Oncol 33(6) (2008) 1195-1199.
[55] Y. Hattori, N. Kanamoto, K. Kawano, H. Iwakura, M. Sone, M. Miura, A. Yasoda, N. Tamura, H. Arai, et al., Molecular characterization of tumors from a transgenic mouse adrenal tumor model: Comparison with human pheochromocytoma, Int J Oncol 37(3) (2010) 695-705.
[56] B. Servenius, J. Vernachio, J. Price, L.C. Andersson, P.A. Peterson, Metastasizing Neuroblastomas in Mice Transgenic for Simian-Virus-40 Large-T (Sv40t) under the Olfactory Marker Protein Gene Promoter, Cancer Res 54(19) (1994) 5198-5205.
[57] J. Guan, E.R. Tucker, H. Wan, D. Chand, L.S. Danielson, K. Ruuth, A. El Wakil, B. Witek, Y. Jamin, et al., The ALK inhibitor PF-06463922 is effective as a single agent in neuroblastoma driven by expression of ALK and MYCN, Dis Model Mech 9(9) (2016) 941-952.
[58] P. Perel, I. Roberts, E. Sena, P. Wheble, C. Briscoe, P. Sandercock, M. Macleod, L.E. Mignini, P. Jayaram, et al., Comparison of treatment effects between animal experiments and clinical trials: systematic review, Bmj-Brit Med J 334(7586) (2007) 197-200.
[59] M. Kroesen, I.C. Brok, D. Reijnen, M.A. van Hout-Kuijer, I.S. Zeelenberg, M.H. Den Brok, P.M. Hoogerbrugge, G.J. Adema, Intra-adrenal murine TH-MYCN neuroblastoma tumors grow

more aggressive and exhibit a distinct tumor microenvironment relative to their subcutaneous equivalents, Cancer Immunol Immun 64(5) (2015) 563-572.

[60] M. Kroesen, S. Nierkens, M. Ansems, M. Wassink, R.J. Orentas, L. Boon, M.H. den Brok, P.M. Hoogerbrugge, G.J. Adema, A transplantable TH-MYCN transgenic tumor model in C57Bl/6 mice for preclinical immunological studies in neuroblastoma, Int J Cancer 134(6) (2014) 1335-1345.

[61] A.J. Cheng, N.C. Cheng, J. Ford, J. Smith, J.E. Murray, C. Flemming, M. Lastowska, M.S. Jackson, C.S. Hackett, et al., Cell lines from MYCN transgenic murine turnours reflect the molecular and biological characteristics of human neuroblastorna, Eur J Cancer 43(9) (2007) 1467-1475.

[62] S. Tsubota, S. Kishida, T. Shimamura, M. Ohira, S. Yamashita, D. Cao, S. Kiyonari, T. Ushijima, K. Kadomatsu, PRC2-Mediated Transcriptomic Alterations at the Embryonic Stage Govern Tumorigenesis and Clinical Outcome in MYCN-Driven Neuroblastoma, Cancer Res 77(19) (2017) 5259-5271.

[63] A.M. Davidoff, S.A. Kimbrough, C.Y.C. Ng, S.J. Shochat, E.F. Vanin, Neuroblastoma regression and immunity induced by transgenic expression of interleukin-12, J Pediatr Surg 34(5) (1999) 902-906.

[64] T. Shimizu, A. Berhanu, R.E. Redlinger, Jr., S. Watkins, M.T. Lotze, E.M. Barksdale, Jr., Interleukin-12 transduced dendritic cells induce regression of established murine neuroblastoma, J Pediatr Surg 36(8) (2001) 1285-92.

[65] H.N. Lode, R. Xiang, N.M. Varki, C.S. Dolman, S.D. Gillies, R.A. Reisfeld, Targeted interleukin-2 therapy for spontaneous neuroblastoma metastases to bone marrow, J Natl Cancer Inst 89(21) (1997) 1586-94.

[66] S. Inoue, Y. Setoyama, A. Odaka, D. Kitagawa, Y. Beck, Chemoimmunotherapeutic effect of combined treatment with ex vivo generated antigen-presenting immune cells and conventional antitumor agents in a mouse neuroblastoma model, J Pediatr Surg 52(10) (2017) 1642-1650.

[67] D.F. Bauer, L. Pereboeva, G.Y. Gillespie, G.A. Cloud, O. Elzafarany, C. Langford, J. Markert, L.S. Lamb, Effect of HSV-IL12 Loaded Tumor Cell-Based Vaccination in a Mouse Model of High-Grade Neuroblastoma, J Immunol Res (2016).

[68] W. Jing, J.A. Gershan, B.D. Johnson, Depletion of CD4 T cells enhances immunotherapy for neuroblastoma after syngeneic HSCT but compromises development of antitumor immune memory, Blood 113(18) (2009) 4449-57.

[69] V. Rigo, L. Emionite, A. Daga, S. Astigiano, M.V. Corrias, C. Quintarelli, F. Locatelli, S. Ferrini, M. Croce, Combined immunotherapy with anti-PDL-1/PD-1 and anti-CD4 antibodies cures syngeneic disseminated neuroblastoma, Sci Rep-Uk 7(1) (2017) 14049.

[70] B. Chiu, J. Coburn, M. Pilichowska, C. Holcroft, F.P. Seib, A. Charest, D.L. Kaplan, Surgery combined with controlled-release doxorubicin silk films as a treatment strategy in an orthotopic neuroblastoma mouse model, Brit J Cancer 111(4) (2014) 708-715.

[71] S. Odate, V. Veschi, S. Yan, N. Lam, R. Woessner, C.J. Thiele, Inhibition of STAT3 with the Generation 2.5 Antisense Oligonucleotide, AZD9150, Decreases Neuroblastoma Tumorigenicity and Increases Chemosensitivity, Clin Cancer Res 23(7) (2017) 1771-1784.

[72] A. Corroyer-Dulmont, N. Falzone, V. Kersemans, J. Thompson, D.P. Allen, S. Able, C. Kartsonaki, J. Malcolm, P. Kinchesh, et al., Improved outcome of I-131-mIBG treatment through combination with external beam radiotherapy in the SK-N-SH mouse model of neuroblastoma, Radiother Oncol 124(3) (2017) 488-495.

[73] A. Jani, F. Shaikh, S. Barton, C. Willis, D. Banerjee, J. Mitchell, S.L. Hernandez, T. Hei, A. Kadenhe-Chiweshe, et al., High-Dose, Single-Fraction Irradiation Rapidly Reduces Tumor Vasculature and Perfusion in a Xenograft Model of Neuroblastoma, Int J Radiat Oncol 94(5) (2016) 1173-1180.

[74] F.L. Byrne, L. Yang, P.A. Phillips, L.M. Hansford, J.I. Fletcher, C.J. Ormandy, J.A. McCarroll, M. Kavallaris, RNAi-mediated stathmin suppression reduces lung metastasis in an orthotopic neuroblastoma mouse model, Oncogene 33(7) (2014) 882-890.

[75] R. Iyer, J.L. Croucher, M. Chorny, J.L. Mangino, I.S. Alferiev, R.J. Levy, V. Kolla, G.M. Brodeur, Nanoparticle delivery of an SN38 conjugate is more effective than Irinotecan in a mouse model of Neuroblastoma, Cancer Res 75 (2015).

[76] C. Yang, J. Tan, J. Zhu, S. Wang, G.H. Wei, YAP promotes tumorigenesis and cisplatin resistance in neuroblastoma, Oncotarget 8(23) (2017) 37154-37163.

[77] H.Q. Wang, E. Halilovic, X.Y. Li, J.S. Liang, Y.C. Cao, D.P. Rakiec, D.A. Ruddy, S. Jeay, J.U. Wuerthner, et al., Combined ALK and MDM2 inhibition increases antitumor activity and overcomes resistance in human ALK mutant neuroblastoma cell lines and xenograft models, Elife 6 (2017).

[78] B.K.A. Seong, K.E. Fathers, R. Hallett, C.K. Yung, L.D. Stein, S. Mouaaz, L. Kee, C.E. Hawkins, M.S. Irwin, et al., A Metastatic Mouse Model Identifies Genes That Regulate Neuroblastoma Metastasis, Cancer Res 77(3) (2017) 696-706.

[79] L. Borriello, R. Nakata, M.A. Sheard, G.E. Fernandez, R. Sposto, J. Malvar, L. Blavier, H. Shimada, S. Asgharzadeh, et al., Cancer-Associated Fibroblasts Share Characteristics and Protumorigenic Activity with Mesenchymal Stromal Cells, Cancer Res 77(18) (2017) 5142-5157.

[80] C.Y. Fang, C.C. Wu, C.L. Fang, W.Y. Chen, C.L. Chen, Long-term growth comparison studies of FBS and FBS alternatives in six head and neck cell lines, PLoS One 12(6) (2017) e0178960.

[81] J. Lee, S. Kotliarova, Y. Kotliarov, A. Li, Q. Su, N.M. Donin, S. Pastorino, B.W. Purow, N. Christopher, et al., Tumor stem cells derived from glioblastomas cultured in bFGF and EGF more closely mirror the phenotype and genotype of primary tumors than do serum-cultured cell lines, Cancer Cell 9(5) (2006) 391-403.

[82] J.P. Gillet, A.M. Calcagno, S. Varma, M. Marino, L.J. Green, M.I. Vora, C. Patel, J.N. Orina, T.A. Eliseeva, et al., Redefining the relevance of established cancer cell lines to the study of mechanisms of clinical anti-cancer drug resistance, Proc Natl Acad Sci U S A 108(46) (2011) 18708-13.

[83] N. Braekeveldt, C. Wigerup, D. Gisselsson, S. Mohlin, M. Merselius, S. Beckman, T. Jonson, A. Borjesson, T. Backman, et al., Neuroblastoma patient-derived orthotopic xenografts retain metastatic patterns and geno- and phenotypes of patient tumours, Int J Cancer 136(5) (2015) E252-E261.

[84] E. Stewart, A. Shelat, C. Bradley, X. Chen, S. Federico, S. Thiagarajan, A. Shirinifard, A. Bahrami, A. Pappo, et al., Development and characterization of a human orthotopic neuroblastoma xenograft, Dev Biol 407(2) (2015) 344-355.

[85] N. Braekeveldt, C. Wigerup, I. Tadeo, S. Beckman, C. Sanden, J. Jonsson, J.S. Erjefalt, A.P. Berbegall, A. Borjesson, et al., Neuroblastoma patient-derived orthotopic xenografts reflect the microenvironmental hallmarks of aggressive patient tumours, Cancer Letters 375(2) (2016) 384-389.

[86] Q. Gao, C.F. Chen, Q. Dong, L. Hou, X. Chen, Y.L. Zhi, X. Li, H.T. Lu, H.Y. Zhang, Establishment of a neuroblastoma mouse model by subcutaneous xenograft transplantation and its use to study metastatic neuroblastoma, Genet Mol Res 14(4) (2015) 16297-16307.

[87] L.T. Bate-Eya, M.E. Ebus, J. Koster, I.J.M. den Hartog, D.A. Zwijnenburg, L. Schild, I. van der Ploeg, M.E.M. Dolman, H.N. Caron, et al., Newly-derived neuroblastoma cell lines propagated in serum-free media recapitulate the genotype and phenotype of primary neuroblastoma tumours, Eur J Cancer 50(3) (2014) 628-637.

[88] M. Hidalgo, E. Bruckheimer, N.V. Rajeshkumar, I. Garrido-Laguna, E. De Oliveira, B. Rubio-Viqueira, S. Strawn, M.J. Wick, J. Martell, et al., A pilot clinical study of treatment guided by personalized tumorgrafts in patients with advanced cancer, Mol Cancer Ther 10(8) (2011) 1311-6.

[89] L. Zhang, B. Wu, S. Baruchel, Oral Metronomic Topotecan Sensitizes Crizotinib Antitumor Activity in ALK(F1174L) Drug-Resistant Neuroblastoma Preclinical Models, Transl Oncol 10(4) (2017) 604-611.

[90] U. Valentiner, F.U. Valentiner, U. Schumacher, Expression of CD44 is associated with a metastatic pattern of human neuroblastoma cells in a SCID mouse xenograft model, Tumor Biology 29(3) (2008) 152-160.

[91] J. Zeki, J.S. Taylor, B. Yavuz, J. Coburn, N. Ikegaki, D.L. Kaplan, B. Chiu, Disseminated injection of vincristine-loaded silk gel improves the suppression of neuroblastoma tumor growth, Surgery 164(4) (2018) 909-915.

[92] J.M. Coburn, J. Harris, R. Cunningham, J. Zeki, D.L. Kaplan, B. Chiu, Manipulation of variables in local controlled release vincristine treatment in neuroblastoma, J Pediatr Surg 52(12) (2017) 2061-2065.

[93] B. Yavuz, J. Zeki, J.M. Coburn, N. Ikegaki, D. Levitin, D.L. Kaplan, B. Chiu, In vitro and in vivo evaluation of etoposide - silk wafers for neuroblastoma treatment, J Control Release 285 (2018) 162-171.

[94] S.S. More, M. Itsara, X.D. Yang, E.G. Geier, M.K. Tadano, Y. Seo, H.F. VanBrocklin, W.A. Weiss, S. Mueller, et al., Vorinostat Increases Expression of Functional Norepinephrine Transporter in Neuroblastoma In Vitro and In Vivo Model Systems, Clin Cancer Res 17(8) (2011) 2339-2349.

[95] Y. Takeuchi, T. Tanaka, M. Higashi, S. Fumino, T. Iehara, H. Hosoi, T. Sakai, T. Tajiri, In vivo effects of short- and long-term MAPK pathway inhibition against neuroblastoma, J Pediatr Surg 53(12) (2018) 2454-2459.

[96] A. Wyce, G. Ganji, K.N. Smitheman, C.W. Chung, S. Korenchuk, Y.C. Bai, O. Barbash, B.C. Le, P.D. Craggs, et al., BET Inhibition Silences Expression of MYCN and BCL2 and Induces Cytotoxicity in Neuroblastoma Tumor Models, Plos One 8(8) (2013).

[97] N. Ikegaki, H. Shimada, A.M. Fox, P.L. Regan, J.R. Jacobs, S.L. Hicks, E.F. Rappaport, X.X. Tang, Transient treatment with epigenetic modifiers yields stable neuroblastoma stem cells resembling aggressive large-cell neuroblastomas, P Natl Acad Sci USA 110(15) (2013) 6097-6102.

[98] K. Zins, D. Kovatchki, T. Lucas, D. Abraham, PlGF and VEGF-A Regulate Growth of High-Risk MYCN-Single Copy Neuroblastoma Xenografts via Different Mechanisms, Int J Mol Sci 17(10) (2016).

[99] P. Beaudry, M. Campbell, N.H. Dang, J. Wen, K. Blote, A.M. Weljie, A Pilot Study on the Utility of Serum Metabolomics in Neuroblastoma Patients and Xenograft Models, Pediatr Blood Cancer 63(2) (2016) 214-220.

[100] J. Harris, E. Herrero-Garcia, A. Russo, A. Kajdacsy-Balla, J.P. O'Bryan, B. Chiu, Silencing Intersectin 1 Slows Orthotopic Neuroblastoma Growth in Mice, J Pediat Hematol Onc 39(8) (2017) E413-E418.
[101] L.L. Lin, C.C. Huang, C.L. Wu, M.T. Wu, W.M. Hsu, J.H. Chuang, Downregulation of c-Myc is involved in TLR3-mediated tumor death of neuroblastoma xenografts, Laboratory Investigation 96(7) (2016) 719-730.
[102] J. Hartwich, W.S. Orr, C.Y. Ng, Y. Spence, C. Morton, A.M. Davidoff, HIF-1 alpha activation mediates resistance to anti-angiogenic therapy in neuroblastoma xenografts, J Pediatr Surg 48(1) (2013) 39-46.
[103] K. Zins, R. Schafer, P. Paulus, S. Dobler, N. Fakhari, M. Sioud, S. Aharinejad, D. Abraham, Frizzled2 signaling regulates growth of high-risk neuroblastomas by interfering with beta-catenin-dependent and beta-catenin-independent signaling pathways, Oncotarget 7(29) (2016) 46187-46202.
[104] C.C. Huang, S.Y. Wang, L.L. Lin, P.W. Wang, T.Y. Chen, W.M. Hsu, T.K. Lin, C.W. Liou, J.H. Chuang, Glycolytic inhibitor 2-deoxyglucose simultaneously targets cancer and endothelial cells to suppress neuroblastoma growth in mice, Dis Model Mech 8(10) (2015) 1247-1254.
[105] L. Swift, C.F. Zhang, T. Trippett, A. Narendran, Potent in vitro and xenograft antitumor activity of a novel agent, PV-10, against relapsed and refractory neuroblastoma, Oncotargets and Therapy 12 (2019) 1293-1307.
[106] W. Sun, Y. Rojas, H. Wang, Y. Yu, Y. Wang, Z. Chen, K. Rajapakshe, X. Xu, W. Huang, et al., EWS-FLI1 and RNA helicase A interaction inhibitor YK-4-279 inhibits growth of neuroblastoma, Oncotarget 8(55) (2017) 94780-94792.
[107] F. Nguyen, I. Alferiev, P. Guan, D.T. Guerrero, V. Kolla, G.S. Moorthy, M. Chorny, G.M. Brodeur, Enhanced Intratumoral Delivery of SN38 as a Tocopherol Oxyacetate Prodrug Using Nanoparticles in a Neuroblastoma Xenograft Model, Clin Cancer Res 24(11) (2018) 2585-2593.
[108] A.E. Evans, K.D. Kisselbach, D.J. Yamashiro, N. Ikegaki, A.M. Camoratto, C.A. Dionne, G.M. Brodeur, Antitumor activity of CEP-751 (KT-6587) on human neuroblastoma and medulloblastoma xenografts, Clin Cancer Res 5(11) (1999) 3594-3602.
[109] E. Daudigeos-Dubus, L. Le Dret, O. Bawa, P. Opolon, A. Vievard, I. Villa, J. Bosq, G. Vassal, B. Geoerger, Dual inhibition using cabozantinib overcomes HGF/MET signaling mediated resistance to pan-VEGFR inhibition in orthotopic and metastatic neuroblastoma tumors, Int J Oncol 50(1) (2017) 203-211.
[110] E. Daudigeos-Dubus, L. Le Dret, V. Rouffiac, O. Bawa, I. Leguerney, P. Opolon, G. Vassal, B. Geoerger, Establishment and Characterization of New Orthotopic and Metastatic Neuroblastoma Models, In Vivo 28(4) (2014) 425-434.
[111] A.G. Henssen, A. Odersky, A. Szymansky, M. Seiler, K. Althoff, A. Beckers, F. Speleman, S. Schafers, K. De Preter, et al., Targeting tachykinin receptors in neuroblastoma, Oncotarget 8(1) (2017) 430-443.
[112] C. Feng, T.Y. Wang, R.H. Tang, J.W. Wang, H. Long, X.N. Gao, S.Q. Tang, Silencing of the MYCN gene by siRNA delivered by folate receptor-targeted liposomes in LA-N-5 cells, Pediatr Surg Int 26(12) (2010) 1185-1191.
[113] Q.Q. Zhu, C. Feng, W.W. Liao, Y. Zhang, S.Q. Tang, Target delivery of MYCN siRNA by folate-nanoliposomes delivery system in a metastatic neuroblastoma model, Cancer Cell International 13 (2013).

[114] S. Ryu, M. Hayashi, H. Aikawa, I. Okamoto, Y. Fujiwara, A. Hamada, Heterogeneous distribution of alectinib in neuroblastoma xenografts revealed by matrix-assisted laser desorption ionization mass spectrometry imaging: a pilot study, Brit J Pharmacol 175(1) (2018) 29-37.
[115] M. Nomura, T. Shimbo, Y. Miyamoto, M. Fukuzawa, Y. Kaneda, 13-Cis retinoic acid can enhance the antitumor activity of non-replicating Sendai virus particle against neuroblastoma, Cancer Sci 104(2) (2013) 238-244.
[116] P.L. Yao, L.P. Chen, T.P. Dobrzanski, B.K. Zhu, B.H. Kang, R. Muller, F.J. Gonzalez, J.M. Peters, Peroxisome proliferator-activated receptor-beta/delta inhibits human neuroblastoma cell tumorigenesis by inducing p53-and SOX2-mediated cell differentiation, Mol Carcinogen 56(5) (2017) 1472-1483.
[117] S. Shusterman, S.A. Grupp, R. Barr, D. Carpentieri, H.Q. Zhao, J.M. Maris, The angiogenesis inhibitor TNP-470 effectively inhibits human neuroblastoma xenograft growth, especially in the setting of subclinical disease, Clin Cancer Res 7(4) (2001) 977-984.
[118] M.J. Morowitz, R. Barr, Q. Wang, R. King, N. Rhodin, B. Pawel, H.Q. Zhao, S.A. Erickson, G.S. Sheppard, et al., Methionine aminopeptidase 2 inhibition is an effective treatment strategy for neuroblastoma in preclinical models, Clin Cancer Res 11(7) (2005) 2680-2685.
[119] W.C. Zamboni, P.J. Houghton, J. Thompson, P.J. Cheshire, S.K. Hanna, L.B. Richmond, X.L. Lou, C.F. Stewart, Altered irinotecan and SN-38 disposition after intravenous and oral administration of irinotecan in mice bearing human neuroblastoma xenografts, Clin Cancer Res 4(2) (1998) 455-462.
[120] J. Thompson, W.C. Zamboni, P.J. Cheshire, L. Lutz, X.L. Luo, Y.L. Li, J.A. Houghton, C.F. Stewart, P.J. Houghton, Efficacy of systemic administration of irinotecan against neuroblastoma xenografts, Clin Cancer Res 3(3) (1997) 423-431.
[121] R.B. Bankert, S.V. Balu-Iyer, K. Odunsi, L.D. Shultz, R.J. Kelleher, Jr., J.L. Barnas, M. Simpson-Abelson, R. Parsons, S.J. Yokota, Humanized mouse model of ovarian cancer recapitulates patient solid tumor progression, ascites formation, and metastasis, PLoS One 6(9) (2011) e24420.
[122] L.D. Shultz, B.L. Lyons, L.M. Burzenski, B. Gott, X. Chen, S. Chaleff, M. Kotb, S.D. Gillies, M. King, et al., Human lymphoid and myeloid cell development in NOD/LtSz-scid IL2R gamma null mice engrafted with mobilized human hemopoietic stem cells, J Immunol 174(10) (2005) 6477-89.
[123] B.E. McIntosh, M.E. Brown, B.M. Duffin, J.P. Maufort, D.T. Vereide, I.I. Slukvin, J.A. Thomson, Nonirradiated NOD,B6.SCID Il2r gamma(-/-) Kit(W41/W41) (NBSGW) Mice Support Multilineage Engraftment of Human Hematopoietic Cells, Stem Cell Rep 4(2) (2015) 171-180.
[124] A.P.A. Theocharides, A. Rongvaux, K. Fritsch, R.A. Flavell, M.G. Manz, Humanized hemato-lymphoid system mice, Haematologica 101(1) (2016) 5-19.
[125] O. Hashimoto, M. Yoshida, Y.I. Koma, T. Yanai, D. Hasegawa, Y. Kosaka, N. Nishimura, H. Yokozaki, Collaboration of cancer-associated fibroblasts and tumour-associated macrophages for neuroblastoma development, J Pathol 240(2) (2016) 211-223.
[126] A.A. Rizvanov, M.E. Yalvac, A.K. Shafigullina, I.I. Salafutdinov, N.L. Blatt, F. Sahin, A.P. Kiyasov, A. Palotas, Interaction and self-organization of human mesenchymal stem cells and neuro-blastoma SH-SY5Y cells under co-culture conditions: A novel system for modeling cancer cell micro-environment, Eur J Pharm Biopharm 76(2) (2010) 253-259.
[127] M. Terme, M. Dorvillius, D. Cochonneau, T. Chaumette, W. Xiao, Chimeric Antibody c.8B6 to O-Acetyl-GD2 Mediates the Same Efficient Anti-Neuroblastoma Effects as Therapeutic

ch14.18 Antibody to GD2 without Antibody Induced Allodynia (vol 9, e87210, 2014), Plos One 9(7) (2014).

[128] N. Siebert, M. Zumpe, M. Juttner, S. Troschke-Meurer, H.N. Lode, PD-1 blockade augments anti-neuroblastoma immune response induced by anti-GD(2) antibody ch14.18/CHO, Oncoimmunology 6(10) (2017).

[129] A. Batova, A. Kamps, S.D. Gillies, R.A. Reisfeld, A.L. Yu, The Ch14.18-GM-CSF fusion protein is effective at mediating antibody-dependent cellular cytotoxicity and complement-dependent cytotoxicity in vitro, Clin Cancer Res 5(12) (1999) 4259-63.

[130] A. Shibina, D. Seidel, S.S. Somanchi, D.A. Lee, A. Stermann, B.J. Maurer, H.N. Lode, C.P. Reynolds, N. Huebener, Fenretinide sensitizes multidrug-resistant human neuroblastoma cells to antibody-independent and ch14.18-mediated NK cell cytotoxicity, J Mol Med 91(4) (2013) 459-472.

[131] M. Fukuda, K. Horibe, K. Furukawa, Enhancement of in vitro and in vivo anti-tumor activity of anti-GD2 monoclonal antibody 220-51 against human neuroblastoma by granulocyte-macrophage colony-stimulating factor and granulocyte colony-stimulating factor, Int J Mol Med 2(4) (1998) 471-5.

[132] E.A. Beierle, W. Dai, M.R. Langham, E.M. Copeland, M.K. Chen, Expression of VEGF receptors in cocultured neuroblastoma cells, J Surg Res 119(1) (2004) 56-65.

[133] M.K. Chen, L. Strande, M. Kain, T.V. Whalen, E.J. Doolin, Induction of apoptosis in a neuroblastoma and hepatocyte coculture model, J Surg Res 78(2) (1998) 123-130.

[134] Y.H. Chanthery, W.C. Gustafson, M. Itsara, A. Persson, C.S. Hackett, M. Grimmer, E. Charron, S. Yakovenko, G. Kim, et al., Paracrine Signaling Through MYCN Enhances Tumor-Vascular Interactions in Neuroblastoma, Sci Transl Med 4(115) (2012).

[135] P.L. Poliani, S. Mitola, M. Ravanini, G. Ferrari-Toninelli, C. D'Ippolito, L.D. Notarangelo, L. Bercich, C. Wagener, M. Memo, et al., CEACAM1/VEGF cross-talk during neuroblastic tumour differentiation, J Pathol 211(5) (2007) 541-9.

[136] N. Baek, O.W. Seo, M. Kim, J. Hulme, S.S.A. An, Monitoring the effects of doxorubicin on 3D-spheroid tumor cells in real-time, Oncotargets and Therapy 9 (2016) 7207-7218.

[137] K. Chikaraishi, H. Takenobu, R.P. Sugino, K. Mukae, J. Akter, M. Haruta, M. Kurosumi, T.A. Endo, H. Koseki, et al., CFC1 is a cancer stemness-regulating factor in neuroblastoma, Oncotarget 8(28) (2017) 45046-45059.

[138] G.K. Gransbury, P. Kappen, C.J. Glover, J.N. Hughes, A. Levina, P.A. Lay, I.F. Musgrave, H.H. Harris, Comparison of KP1019 and NAMI-A in tumour-mimetic environments, Metallomics 8(8) (2016) 762-773.

[139] L.M. Griner, K. Gampa, T. Do, H. Nguyen, D. Farley, C.J. Hogan, D.S. Auld, S.J. Silver, Generation of High-Throughput Three-Dimensional Tumor Spheroids for Drug Screening, J Vis Exp (139) (2018).

[140] V. Sidarovich, M. De Mariano, S. Aveic, M. Pancher, V. Adami, P. Gatto, S. Pizzini, L. Pasini, M. Croce, et al., A High-Content Screening of Anticancer Compounds Suggests the Multiple Tyrosine Kinase Inhibitor Ponatinib for Repurposing in Neuroblastoma Therapy, Mol Cancer Ther 17(7) (2018) 1405-1415.

[141] F. Lu, S. Kishida, P. Mu, P. Huang, D. Cao, S. Tsubota, K. Kadomatsu, NeuroD1 promotes neuroblastoma cell growth by inducing the expression of ALK, Cancer Sci 106(4) (2015) 390-6.

[142] A. Coulon, M. Flahaut, A. Muhlethaler-Mottet, R. Meier, J. Liberman, K. Balmas-Bourloud, K. Nardou, P. Yan, S. Tercier, et al., Functional sphere profiling reveals the complexity of neuroblastoma tumor-initiating cell model, Neoplasia 13(10) (2011) 991-1004.

[143] J. Suebsoonthron, T. Jaroonwitchawan, M. Yamabhai, P. Noisa, Inhibition of WNT signaling reduces differentiation and induces sensitivity to doxorubicin in human malignant neuroblastoma SH-SY5Y cells, Anticancer Drugs 28(5) (2017) 469-479.

[144] S. Ayla, A. Bilir, B.C. Soner, O. Yilmaz-Dilsiz, M. Erguven, G. Oktem, Notch signaling-related therapeutic strategies with novel drugs in neuroblastoma spheroids, J Pediat Hematol Onc 36(1) (2014) 37-44.

[145] B.T. Craig, E.J. Rellinger, A.L. Alvarez, H.L. Dusek, J. Qiao, D.H. Chung, Induced differentiation inhibits sphere formation in neuroblastoma, Biochem Biophys Res Commun 477(2) (2016) 255-9.

[146] R. Cuperus, A.B. van Kuilenburg, R. Leen, J. Bras, H.N. Caron, G.A. Tytgat, Promising effects of the 4HPR-BSO combination in neuroblastoma monolayers and spheroids, Free Radic Biol Med 51(6) (2011) 1213-20.

[147] S.M. Sagnella, J. Trieu, H. Brahmbhatt, J.A. MacDiarmid, A. MacMillan, R.M. Whan, C.M. Fife, J.A. McCarroll, A.J. Gifford, et al., Targeted Doxorubicin-Loaded Bacterially Derived Nano-Cells for the Treatment of Neuroblastoma, Mol Cancer Ther 17(5) (2018) 1012-1023.

[148] S. Aveic, D. Corallo, E. Porcu, M. Pantile, D. Boso, C. Zanon, G. Viola, V. Sidarovich, E. Mariotto, et al., TP-0903 inhibits neuroblastoma cell growth and enhances the sensitivity to conventional chemotherapy, Eur J Pharmacol 818 (2018) 435-448.

[149] M.L. Schmidt, K.L. Kuzmanoff, L. Ling-Indeck, J.M. Pezzuto, Betulinic acid induces apoptosis in human neuroblastoma cell lines, Eur J Cancer 33(12) (1997) 2007-10.

[150] J. Navratilova, M. Karasova, M. Kohutkova Lanova, L. Jirakova, Z. Budkova, J. Pachernik, J. Smarda, P. Benes, Selective elimination of neuroblastoma cells by synergistic effect of Akt kinase inhibitor and tetrathiomolybdate, J Cell Mol Med 21(9) (2017) 1859-1869.

[151] S.H. Cunningham, R.J. Mairs, T.E. Wheldon, P.C. Welsh, G. Vaidyanathan, M.R. Zalutsky, Toxicity to neuroblastoma cells and spheroids of benzylguanidine conjugated to radionuclides with short-range emissions, Brit J Cancer 77(12) (1998) 2061-8.

[152] J.M. Lee, D.Y. Park, L. Yang, E.J. Kim, C.D. Ahrberg, K.B. Lee, B.G. Chung, Generation of uniform-sized multicellular tumor spheroids using hydrogel microwells for advanced drug screening, Sci Rep-Uk 8(1) (2018) 17145.

[153] S. Daster, N. Amatruda, D. Calabrese, R. Ivanek, E. Turrini, R.A. Droeser, P. Zajac, C. Fimognari, G.C. Spagnoli, et al., Induction of hypoxia and necrosis in multicellular tumor spheroids is associated with resistance to chemotherapy treatment, Oncotarget 8(1) (2017) 1725-1736.

[154] O.I. Hoffmann, C. Ilmberger, S. Magosch, M. Joka, K.W. Jauch, B. Mayer, Impact of the spheroid model complexity on drug response, J Biotechnol 205 (2015) 14-23.

[155] D.L. Priwitaningrum, J.G. Blonde, A. Sridhar, J. van Baarlen, W.E. Hennink, G. Storm, S. Le Gac, J. Prakash, Tumor stroma-containing 3D spheroid arrays: A tool to study nanoparticle penetration, J Control Release 244(Pt B) (2016) 257-268.

[156] T. Courau, J. Bonnereau, J. Chicoteau, H. Bottois, R. Remark, L. Assante Miranda, A. Toubert, M. Blery, T. Aparicio, et al., Cocultures of human colorectal tumor spheroids with immune cells reveal the therapeutic potential of MICA/B and NKG2A targeting for cancer treatment, J Immunother Cancer 7(1) (2019) 74.

[157] H.R. Jung, H.M. Kang, J.W. Ryu, D.S. Kim, K.H. Noh, E.S. Kim, H.J. Lee, K.S. Chung, H.S. Cho, et al., Cell Spheroids with Enhanced Aggressiveness to Mimic Human Liver Cancer In Vitro and In Vivo, Sci Rep-Uk 7 (2017).

[158] G.N. Li, L.L. Livi, C.M. Gourd, E.S. Deweerd, D. Hoffman-Kim, Genomic and morphological changes of neuroblastoma cells in response to three-dimensional matrices, Tissue Eng 13(5) (2007) 1035-47.

[159] C.B. Mitchell, G.M. O'Neill, Cooperative cell invasion: matrix metalloproteinase-mediated incorporation between cells, Mol Biol Cell 27(21) (2016) 3284-3292.

[160] C.B. Mitchell, G.M. O'Neill, Rac GTPase regulation of 3D invasion in neuroblastomas lacking MYCN amplification, Cell Adhes Migr 11(1) (2017) 68-79.

[161] C. Curtin, J.C. Nolan, R. Conlon, L. Deneweth, C. Gallagher, Y.J. Tan, B.L. Cavanagh, A.Z. Asraf, H. Harvey, et al., A physiologically relevant 3D collagen-based scaffold-neuroblastoma cell system exhibits chemosensitivity similar to orthotopic xenograft models, Acta Biomater 70 (2018) 84-97.

[162] K.A. Fitzgerald, J.F. Guo, E.G. Tierney, C.M. Curtin, M. Malhotra, R. Darcy, F.J. O'Brien, C.M. O'Driscoll, The use of collagen-based scaffolds to simulate prostate cancer bone metastases with potential for evaluating delivery of nanoparticulate gene therapeutics, Biomaterials 66 (2015) 53-66.

[163] K. Stock, M.F. Estrada, S. Vidic, K. Gjerde, A. Rudisch, V.E. Santo, M. Barbier, S. Blom, S.C. Arundkar, et al., Capturing tumor complexity in vitro: Comparative analysis of 2D and 3D tumor models for drug discovery, Sci Rep-Uk 6 (2016) 28951.

[164] J. Kazantseva, R. Ivanov, M. Gasik, T. Neuman, I. Hussainova, Graphene-Augmented Nanofiber Scaffolds Trigger Gene Expression Switching of Four Cancer Cell Types, Acs Biomater Sci Eng 4(5) (2018) 1622-1629.

[165] M. Mitra, C. Mohanty, A. Harilal, U.K. Maheswari, S.K. Sahoo, S. Krishnakumar, A novel in vitro three-dimensional retinoblastoma model for evaluating chemotherapeutic drugs, Mol Vis 18(142-45) (2012) 1361-1378.

[166] E.L.S. Fong, S.E. Lamhamedi-Cherradi, E. Burdett, V. Ramamoorthy, A.J. Lazar, F.K. Kasper, M.C. Farach-Carson, D. Vishwamitra, E.G. Demicco, et al., Modeling Ewing sarcoma tumors in vitro with 3D scaffolds, P Natl Acad Sci USA 110(16) (2013) 6500-6505.

[167] A. Marturano-Kruik, A. Villasante, K. Yaeger, S.R. Ambati, A. Chramiec, M.T. Raimondi, G. Vunjak-Novakovic, Biomechanical regulation of drug sensitivity in an engineered model of human tumor, Biomaterials 150 (2018) 150-161.

[168] A. Villasante, K. Sakaguchi, J. Kim, N.K. Cheung, M. Nakayama, H. Parsa, T. Okano, T. Shimizu, G. Vunjak-Novakovic, Vascularized Tissue-Engineered Model for Studying Drug Resistance in Neuroblastoma, Theranostics 7(17) (2017) 4099-4117.

[169] P. Yeung, H.S. Sin, S. Chan, G.C.F. Chan, B.P. Chan, Microencapsulation of Neuroblastoma Cells and Mesenchymal Stromal Cells in Collagen Microspheres: A 3D Model for Cancer Cell Niche Study, Plos One 10(12) (2015).

[170] C.W. Yeung, K. Cheah, D. Chan, B.P. Chan, Effects of Reconstituted Collagen Matrix on Fates of Mouse Embryonic Stem Cells Before and After Induction for Chondrogenic Differentiation, Tissue Eng Pt A 15(10) (2009) 3071-3085.

[171] H. Wang, M. La Russa, L.S. Qi, CRISPR/Cas9 in Genome Editing and Beyond, Annu Rev Biochem 85 (2016) 227-64.

[172] M.P. Calos, Genome Editing Techniques and Their Therapeutic Applications, Clin Pharmacol Ther 101(1) (2017) 42-51.

[173] H. Yin, K.J. Kauffman, D.G. Anderson, Delivery technologies for genome editing, Nat Rev Drug Discov 16(6) (2017) 387-399.

[174] J.H. Park, M. Szemes, G.C. Vieira, Z. Melegh, S. Malik, K.J. Heesom, L. Von Wallwitz-Freitas, A. Greenhough, K.W. Brown, et al., Protein arginine methyltransferase 5 is a key regulator of the MYCN oncoprotein in neuroblastoma cells, Mol Oncol 9(3) (2015) 617-627.
[175] S. Ambrosio, S. Amente, C.D. Sacca, M. Capasso, R.A. Calogero, L. Lania, B. Majello, LSD1 mediates MYCN control of epithelial-mesenchymal transition through silencing of metastatic suppressor NDRG1 gene, Oncotarget 8(3) (2017) 3854-3869.
[176] J. Shen, S. Najafi, S. Stable, J. Fabian, E. Koeneke, F.R. Kolbinger, J.K. Wrobel, B. Meder, M. Distel, et al., A kinome-wide RNAi screen identifies ALK as a target to sensitize neuroblastoma cells for HDAC8-inhibitor treatment, Cell Death Differ 25(12) (2018) 2053-2070.
[177] L. Chen, G. Alexe, N.V. Dharia, L. Ross, A.B. Iniguez, A.S. Conway, E.J. Wang, V. Veschi, N. Lam, et al., CRISPR-Cas9 screen reveals a MYCN-amplified neuroblastoma dependency on EZH2, J Clin Invest 128(1) (2018) 446-462.
[178] C.E. Mahoney, D. Pirman, V. Chubukov, T. Sleger, S. Hayes, Z.P. Fan, E.L. Allen, Y. Chen, L. Huang, et al., A chemical biology screen identifies a vulnerability of neuroendocrine cancer cells to SQLE inhibition, Nat Commun 10(1) (2019) 96.
[179] M. Michaelis, B. Agha, F. Rothweiler, N. Loschmann, Y. Voges, M. Mittelbronn, T. Starzetz, P.N. Harter, B.A. Abhari, et al., Identification of flubendazole as potential anti-neuroblastoma compound in a large cell line screen, Sci Rep-Uk 5 (2015).

Chapter 3: Development of a silk-based neuroblastoma model for studying the effects of hypoxia and scaffolded growth

3.1. Introduction

Neuroblastoma (NB) is the most common extracranial childhood tumor [1]. It is an extremely heterogeneous disease with low-risk patients having a high survival rate and high-risk patients exhibiting an event free survival rate of less than 50% [2, 3]. Patients with high-risk NB undergo intense multimodal treatment, but still exhibit high levels of relapse [4, 5]. This may be due to the disease heterogeneity, lack of clear genetic markers/drivers, and frequency of metastasis [2, 3, 6]. Many changes within the tumor microenvironment, including hypoxia, are associated with poor disease outcomes and metastasis [7, 8].

Hypoxia, the presence of oxygen tensions below physiologic levels, is frequently found in solid tumors. In normal tissues, the oxygen concentration typically ranges from 4.5-9%, while hypoxic tissues frequently exhibit oxygen concentrations of less than 2% [9, 10]. Low oxygen tensions in tumors results in activation of a complex cascade involving the HIF, PI3K, MAPK, and NFκB pathways [11-15], which can lead to increased angiogenesis, altered cell metabolism, resistance to therapy, and metastasis [8, 16-19]. In NB, a hypoxic signature has been associated with poor clinical outcomes [7]. Few *in vitro* models of NB are available, and those that do exist fail to capture relevant heterogeneity of the tumors.

In vitro tumor models are used to identify potential therapeutic strategies and to understand disease progression [20-22]. The most common tumor models consist of monolayer cultured cells adhered to polystyrene dishes. These models, while informative and simple to use, are limited as they lack essential components of the tumor microenvironment [23]. These microenvironment components include 3D cell-cell interactions and gradients of oxygen and nutrients [24-26]. Various methods of 3D cultures have been employed to address these limitations, including spheroids, hydrogels, and scaffolds [20, 23, 26-28]. These methods achieve oxygen tension gradients closer to that of tumor physiology. Additionally, methods of inducing hypoxia, such as low oxygen incubators or chemical induction of hypoxia through upregulation of HIF-1 have been used to elucidate the specific effects of hypoxic pathways [29].

Scaffolds and hydrogels for 3D cell growth can be fabricated from a number of materials, both biological and synthetic [30-32]. Synthetic materials, such as poly(vinyl alcohol), polylactide, polyglycolides, and poly(ethylene glycol) are advantageous as they are typically easy to process and highly tunable [32-34]. Commonly used biological materials include collagen, fibrin, Matrigel®, chitosan, and alginate. Biological materials typically have higher levels of biocompatibility and bioactive moiety for cell attachments and functionality [24, 31, 32, 35-39]

Silk fibroin, a natural biomaterial, can be fabricated into porous scaffolds through lyophilization [40, 41]. Silk fibroin is advantageous as all aqueous processing methods are utilized for scaffold and hydrogel fabrication [42]. Additionally, it demonstrates excellent biocompatibility, lacks immune activation, and exhibits long-term stability in a range of temperature and pH [40, 41, 43-45]. Cells have been demonstrated to adhere to and proliferate on silk, likely due to a combination of roughness and electrostatic interactions with soluble factors present in culture medium (serum) [46, 47]. Several types of cancer such as breast, prostate, and adenocarcinoma have been successfully modeled using silk fibroin scaffolds [48-50]. However, cell-driven microenvironments have not been investigated using silk fibroin scaffolds.

As there are limited preclinical models capable of characterizing the impact of hypoxia and 3D growth, development of one such system is needed. The present study utilizes high cell density cultures of NB cells inside silk scaffolds to generate a scaffolded NB model with cell-driven microenvironment changes. Computational and experimental studies were performed to characterize these changes. Scaffolded NB cultured under ambient oxygen and low oxygen conditions were utilized to determine changes resulting because of low oxygen versus scaffolding in general. Monolayer cultures under ambient oxygen and low oxygen conditions were used as controls to verify low oxygen-driven effects. Responsiveness to therapeutics was evaluated to demonstrate potential applications of testing preclinical treatment strategies for NB, and this system could be applied to study additional cancer types. Collectively, these results present a high cell density scaffolded tumor model that incorporates controlled 3D, spatial features of the tumor microenvironment integrate for drug screening to treat cancer.

3.2. Materials and Methods

3.2.1. Cell culturing

KELLY NB cells (Millipore Sigma, St. Louis, MO) were maintained in Roswell Park Memorial Institute 1640 (RPMI) medium supplemented with 10% v/v fetal bovine serum, 100 U/mL penicillin, 100 µg/mL streptomycin, and 2 mM L-glutamine (Fisher Scientific, Hampton, NH). SK-N-AS NB cells (ATCC, Manassas, VA) were maintained in Dulbecco's Modified Eagle Medium (DMEM) supplemented with 10% v/v fetal bovine serum, 100 U/mL penicillin, 100 µg/mL streptomycin, 2 mM L-glutamine, and 0.1 mM NEAA (Fisher Scientific, Hampton, NH). SH-SY-5Y cells (ATCC, Manassas, VA) were maintained in DMEM/F12 50:50 supplemented with 10% v/v fetal bovine serum, 100 U/mL penicillin, 100 µg/mL streptomycin, 2mM L-glutamine, and 0.1 mM NEAA. All cells were maintained at 37°C and 5% CO_2 in a humidified environment and passaged using 0.25% trypsin-EDTA when 70-80% confluence. For low oxygen cultures a 37°C, 5% CO_2, 1% O_2 incubator was used.

3.2.2. Silk fibroin extraction

Silk fibroin from *Bombyx mori* silkworm cocoons (Tajima Shoji Co Yokohama, Japan), kindly provided by Dr. David L. Kaplan at Tufts University, was extracted as previously described [40]. Briefly, 5 g of cocoons were cut into approximately 1 cm x 1 cm pieces. Cocoons were then boiled in 0.02 M Na2CO3 for 30 min to extract the sericin and allowed to dry overnight. The dried fibers were then dissolved in 20 mL of 9.3 M LiBr at 60°C for 3 h. The dissolved silk fibroin was dialyzed in 3,500 MWCO dialysis tubing (Fisher Scientific, Hampton, NH) against ultrapure water for 2 d with a minimum of 6 water changes. The aqueous silk fibroin (referred to as silk from here on) solution was stored at 4°C.

3.2.3. Silk scaffold fabrication

Silk scaffolds were fabricated using 2 mL of 5% (w/v) silk solutions in 5.6 mm cylindrical molds. Lyophilization was performed using a shelf lyophilizer with controlled temperature (Labconco, Kansas City, MO). Samples were equilibrated at 20°C for 30 min followed by rate-controlled freezing (-0.5°C/min) to -45°C with a 2 h hold. Samples were then ramped to -25°C (0.5°C/min) for primary drying for 30 h. Secondary drying was performed with a 2 h hold at -4°C (ramp at 1°C/min), followed by ramping up to 20°C (1°C/min). The vacuum was held at 0.210 Torr for both primary and secondary drying. To render the materials insoluble, scaffolds were steam-treated via autoclaving. Scaffolds were vibratome sectioned to a thickness of 200 µm and biopsy punched with a 6 mm diameter biopsy punch. Scaffolds were autoclaved in ultrapure water and then soaked overnight in complete medium prior to cell studies.

3.2.4. Seeding of cells on scaffolds

SK-N-AS, KELLY, and SH-SY-5Y cells grown as described above were made into a single cell suspension. For seeding studies, 10 µL of cells at a range of cell concentrations from 1.25 x 10^7 cells/mL-4.0 x 10^8 cells/mL were used. For all other studies, a concentration of 1 x 10^8 cells/mL were used with a volume of 10 µL. Cells were seeded by applying a volume of 5 µL of to the scaffold. After 10 minutes, the scaffold was rotated 180° and the remaining 5 µL was applied. The cell-seeded scaffolds were allowed to incubate at 37°C, 5% CO_2, and 21% O_2 for 4 h before moving to medium. For cell seeding studies, scaffolds were cultured for 24 h at 21% O_2 in 2 mL of medium in a 24-well pate**.** For all other studies cells/scaffolds were grown in 6-well plates with 3 mL of medium in 21% O_2 or 1% O_2; monolayer cultured cells were seeded at a concentration of 5 x 10^5 cells/well.

3.2.5. DNA content analysis

DNA content was analyzed using a Quant-iT™ PicoGreen™ dsDNA Assay Kit (Fisher Scientific, Hampton, NH) according to the manufacturer's protocol. Samples were lysed with 0.5% Triton X-100 in Tris-EDTA buffer for 20 min at room temperature. All samples were passed through a freeze-thaw cycle (-20 °C) prior to analysis. After thawing, the samples were mixed, centrifuged, and diluted 1:5 with TE buffer. The samples were incubated at room temperature for 5 min in a 200-fold dilution of the PicoGreen™ dye. The full protocol can be found in **Appendix X**. The DNA concentration was determined by measuring the fluorescence at an excitation wavelength of 480 nm and an emission wavelength of 520 nm (Victor Multilabel Plate Reader, Perkin Elmer, Waltham, MA) and comparing to a standard curve of lambda DNA.

3.2.6. Histology

Scaffolds were frozen in OCT and cryosectioned to 20 µm. Sections were fixed in 100% methanol at 4 °C for 5 minutes, followed by 25% methanol for 5 minutes. Sections were then washed in PBS for 10 minutes and stained with Harris hematoxylin and eosin using a standard protocol **(Appendix V**).

3.2.7. Pimonidazole staining

Cultures were treated with 300 µM pimonidazole-hcl (Hypoxyprobe, Burlington, MA) for 24 h prior to the end of the study. Scaffolds were fixed in 10% formalin, frozen in OCT, and cryosectioned to a thickness of 20 µm. Sections were hydrated in PBS for 10 minutes, then blocked and permeabilized in 5% normal goat serum with 0.1% Triton X-100 for 1 h. Blocked and permeabilized sections were incubated overnight with secondary antibody (HP-RedAPC-Mab, Hypoxyprobe, Burlington, MA) at a dilution of 1:50 in PBS at 4°C. Sections were washed and counter stained with Hoechst 33342 (1:5,000) to visualize cell nuclei. Scaffolds that were not treated with pimonidazole were used as a negative control (**Appendix IV**).

3.2.8. Ki-67 immunostaining

Cell seeded scaffolds were fixed in 10% formalin, frozen in OCT, and cryosectioned to a thickness of 20 µm. Sections were hydrated in PBS for 10 minutes, then blocked and permeabilized in 5% normal goat serum with 0.1% Triton X-100 for 1 h. Blocked and permeabilized sections were incubated overnight with primary antibody (1:100) at 4°C in 1% BSA + 0.3% Triton X-100. Secondary antibody (goat anti rabbit 594) was incubated overnight at a dilution of 1:250 in PBS. Sections were washed and counter stained with Hoechst 33342 (1:5,000) to visualize cells and nuclei respectively. Sections without ki67 antibody applied were used as a negative control (**Appendix IV**).

3.2.9. TUNEL staining

TUNEL staining was performed on 20 μm thick cryosections using a DeadEnd™ Fluorometric TUNEL system (Promega, Madison, WI) according to the manufacturer's protocol. Briefly, sections were hydrated in PBS, permeabilized, and treated with equilibrium buffer. The positive control sample was treated with DNASE I (Millipore Sigma, St. Louis, MO) (**Appendix IV**). Sections were then incubated with fluorescently-labeled nucleotides and terminal deoxynucleotide transferase which catalyzed the polymerization of nucleotides to the 3'-OH terminal end of the DNA fragments. Sections treated with nucleotides but not terminal deoxynucleotide transferase were used as a negative control (**Appendix IV**). The sections were then counterstained with Hoechst 33342 (1:5,000) for 10 min at room temperature.

3.2.10. Whole-mount immunostaining

Full scaffolds were stained with Adipored (1:500), Hoechst 33342 (1:5,000), and phalloidin (1:40) in 5% BSA + 0.1% Triton X-100 PBS overnight at 4 °C. Samples were washed in PBS before imaging.

3.2.11. Periodic acid-Schiff base staining

Scaffolds were fixed in 10% formalin, frozen in OCT, and cryosectioned to a thickness of 20 μm. Cryosections were brought to room temperature and rinsed with distilled water to remove OCT. Slides were then treated with periodic acid solution for 7 minutes and rinsed in distilled water for 10 minutes. The cells were then treated with Schiff reagent (VWR, Radnor, PA) for 15 minutes and rinsed in tap water for 10 minutes. Slides were brought to xylene and mounted with cytoseal. The full protocol can be found in **Appendix VI**.

3.2.12. Scanning electron microscopy

The cells morphology on the scaffold surface was visualized using scanning electron microscopy (SEM). Samples were fixed in 4% paraformaldehyde and chemically dried using sequentially increasing concentrations of ethanol followed by hexamethyldisilazane (Millipore Sigma, St. Louis, MO). The dry samples were sputter coated with gold (25 mA, 60s) and imaged with a Phenom G1 SEM (Thermo Fisher Scientific, Waltham, MA) using a 5-kV electron beam.

3.2.13. Brightfield imaging

Brightfield imaging of histology was performed in bright field an upright microscope (Nikon Eclipse E600, Tokyo, Japan) with a digital camera (Spot Insight CMOS 5.1, Sterling Heights, MI).

3.2.14. Confocal imaging

Whole mount confocal imaging was performed using a confocal microscope (Leica TCS SP5, Wetzlar, Germany).

3.2.15. Fluorescent imaging

Fluorescent imaging was performed used an Axiovert 200M Zeiss inverted epi-fluor microscope (Oberkochen, Germany). Exposure time was determined based on negative controls (highest possible exposure where negative control failed to exhibit positive staining) for ki67 and pimonidazole. For TUNEL staining exposure time was determined based on positive visualization of the DNASE treated positive control and lack of positive staining in the negative control sample.

3.2.16. Whole scaffold brightfield imaging

Whole scaffold stitched imaging of histology was performed an automated inverted microscope (Lionheart FX, BioTek, Winooski, VT). Scaffold images were stitched together using the auto stitch function.

3.2.17. Cytokine secretion-dot blot

Medium was collected and centrifuged to remove cell debris. All medium went through one freeze-thaw cycle to ensure consistent treatment. A human cytokine array (AAH-CYT-1000-2; Raybiotech, Peachtree Corners, GA) was performed on the medium following the manufacturer's protocol. The protocol can be found in **Appendix VII.** Blot images were acquired using a Gel Doc imaging system (Biorad, Hercules, CA). Following acquisition of the images, blots were analyzed and normalized to determine relative change in cytokine secretion (**Appendix II**). Briefly, the blot was inputted into a custom image processing GUI that defined the region of interest as a ring in the center of each dot. The background was then detected using a second ring with a radius 3x the size of the dot selection ring. The dots were then normalized by subtracting the background intensity from each dot intensity using MATLAB. Each blot was then normalized to its own internal controls and to its dsDNA content as determined using a Quant-iT™ PicoGreen™ Assay. Each secreted factor was normalized to the monolayer ambient oxygen (2D 21%) condition for its respective cell line.

3.2.18. Enzyme-linked immunosorbent assays (ELISAs)

ELISAs to validate individual targets were performed using commercially available kits for VEGF-A, MCP-3, GM-CSF, and IL-8 (R&D Systems, Minneapolis, MN) following the manufacturer's protocol. The protocol can be found in **Appendix IX**. Data was collected at wavelengths of 450 nm and 540 nm (background control) using a SpectraMax 250 (Molecular

Devices, San Jose, CA). Each sample was normalized to its dsDNA content as determined using a Quant-iT™ PicoGreen™ Assay.

3.2.19. Gene expression

Total RNA was isolated after 3 d of culture using a TRIzol reagent (Fisher Scientific, Hampton, NH) according to the manufacturer's instructions. RNA was dissolved in ultrapure molecular grade water and the concentration determined using an absorbance of 260 nm using a spectrophotometer (Nanodrop 2000, Thermo Scientific). Complement DNA (cDNA) was synthesized using High-Capacity cDNA Reverse Transcription Kit (Applied Biosystems, Foster City, CA). Real-time PCR was performed on a 7500 Real Time PCR System (Applied Biosystems, Foster City, CA) using SYBR™ Green master mix (Applied Biosystems, Foster City, CA). SDHA was used as a reference gene, and the level or expression was calculated using the ΔΔCt method. Data is presented as relative to monolayer ambient oxygen (2D 21%). The PCR primers are listed in **(Table 3.1)**.

3.2.20. Cell sensitivity to cytotoxic drugs

Scaffolds seeded as described above were cultured in 12-well plates for 3 d in 2 mL of medium. Monolayer culture was seeded at 75,000 cells/well in a 12-well plate. After 3 d medium was replaced with fresh medium (control), medium containing etoposide (Selleckchem, Houston, TX) at a concentration of 1 µm or 10 µm, or medium containing tirapazamine (Millipore Sigma, St. Louis, MO) at a concentration 2 µg/mL or 20 µg/mL. Cells were treated for 3 d. After 3 d, cell viability was determined using the Quant-iT™ PicoGreen™ dsDNA Assay Kit as described above.

3.2.21. Mathematical modeling of oxygen concentrations

Mathematical modeling was utilized to model oxygen gradients within the scaffolds. Simulated oxygen diffusion and consumption was run on a commercially available finite element platform (COMSOL, Burlington, MA). Three-dimensional axisymmetric modeling was used based on a standard 6-well plate containing 3 mL of medium and one scaffold with a diameter of 6 mm and a thickness of 200 µm, seeded with 500,000 cells. These models were run through a "transport of diluted species" module incorporating both diffusion and consumption rate (modeled using Michaelis-Menten kinetics) available from literature [51-55].

Oxygen diffusion coefficient, $D = 2.6 \times 10^{-9}\ m^2\ s^{-1}$

Oxygen consumption rate, $OCR = -3.09 \times 10^{-4}\ mol\ m^{-3}s^{-1}$

Michaelis-Menten coefficient, $MM = 0.0046\ mol\ m^{-3}$

Initial concentration of oxygen at the surface of the culture $C = 0.21\ mol\ m^{-3}$

The model utilizes the following equations:

Rate of Oxygen Consumption, $R = -\frac{OCR * C}{MM + C}$

Transport of diluted species: $\frac{dc_i}{dt} + \nabla \cdot (-D_i \nabla c_i) = R_i$

Initial concentration of oxygen at the surface of the culture, $C_0 = 0.21\ mol\ m^{-3}$ for ambient oxygen or $0.01\ mol\ m^{-3}$ for 1% O_2

Uniform oxygen consumption was assumed within the scaffold. It was also assumed that the scaffold did not limit oxygen diffusion. Culture medium as well as the scaffolds were modeled as water.

3.2.22. Statistical analysis

Data is presented as mean ± SEM for all gene expression, cytokine secretion data, and cell seeding data. Data is presented as mean ± SD for all other data. All data is presented as the mean of three biological replicates. Statistical significance was determined by one-way ANOVA followed by Tukey honestly significant differences test in GraphPad Prism (version 5.0; San Diego, CA. Significance was determined at $P < 0.05$. Statistics on ELISA data were performed on the $\log_{10}$-transformed data as has been previously described [56, 57].

3.3. Results

3.3.1. Fabrication and cell seeding on silk scaffolds

Next, we sought to confirm cell attachment to the silk scaffolds. Silk scaffolds were fabricated through the lyophilization followed by autoclaving of the silk to induce β-sheet formation and render the material insoluble (**Figure 3.1 A, B**). Scaffolds were then vibratome sectioned to a thickness of 200 µm and biopsy punched to width of 6 mm (**Figure 3.1 C)**. The thickness of 200 µm was chosen due to the cells ability to penetrate the entire scaffold, whereas thicker scaffolds contained an area in the middle of the scaffold that lacked cells (data not shown). SEM analysis of the silk scaffold demonstrated a microporous structure with pore sizes comparable to previously demonstrated results (70-90 µm) (**Figure 3.1 C)**. Cell seeding analysis demonstrated that approximately 50% of the cells seeded adhered to the scaffolds after 1 day (**Figure 3.1 D**).

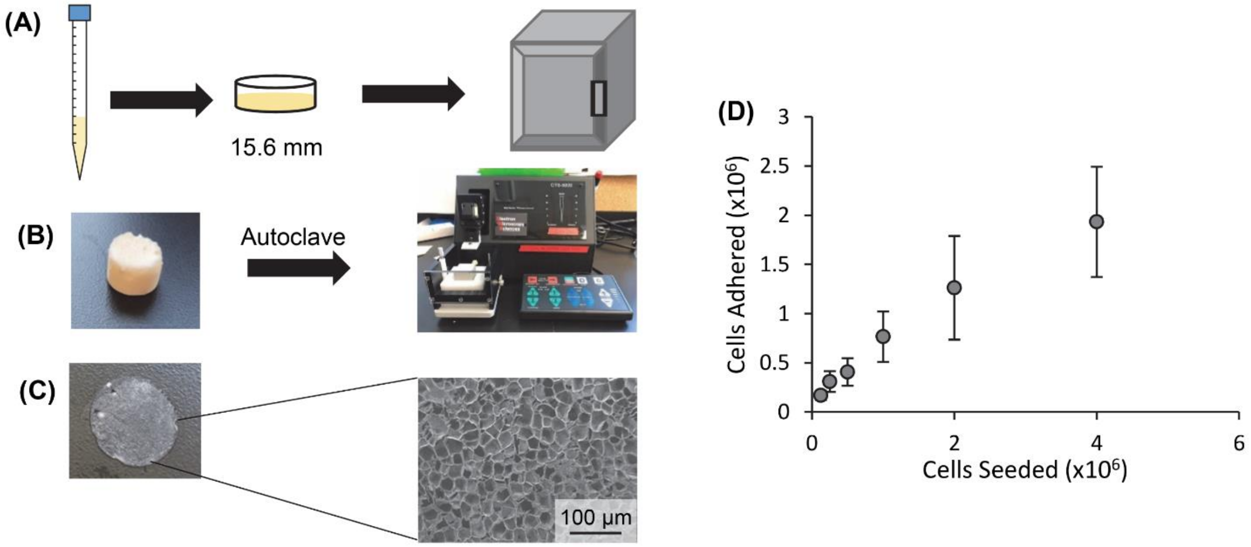

Figure 3.1. Fabrication of lyophilized silk fibroin scaffolds and seeding of cells. (A) Silk scaffolds were fabricated 5% silk fibroin in a 15.6 mm diameter mold, lyophilized with rate-controlled freezing. (B) Lyophilized silk fibroin cylinders were removed from the cylindrical molds and autoclaved to render material insoluble, then vibratome sectioned to desired thickness. (C) Silk fibroin sections were biopsy punched to 6 mm in diameter to remove edge effects. SEM imaging confirms presence of micropores throughout the scaffold. (D) Cell seeding of SK-N-AS cells on silk scaffolds as determined by DNA quantification. Data is presented as mean ± SEM for three independent experiments.

3.3.2. Mathematical modeling of oxygen concentration throughout the scaffolded NB model

We first sought to determine to what extent low oxygen conditions could occur due to cell-driven oxygen consumption. Mathematical modeling of scaffolded culture in ambient and low oxygen was performed (**Figure 3.2**). These models demonstrated a significant drop in oxygen concentration within the scaffold at both ambient and low oxygen when modeled with 0.5 x 10^6 cells. In ambient oxygen, oxygen concentrations within the scaffold decreased to below 5%, with the very interior of the scaffold reaching oxygen concentrations less than 1% (**Figure 3.2 A**). In low oxygen, the interior of the scaffold reached concentrations close to 0.1% (**Figure 3.2 B**). As the median oxygen concentration of untreated tumors ranges from 0.3% to 4.5%, this suggests that the oxygen concentrations exhibited in the scaffolds fall into a physiologically relevant range. Subsequent experiments were performed using a seeding density of 1 x 10^6 cells/scaffold assuming approximately 50% cell attachment.

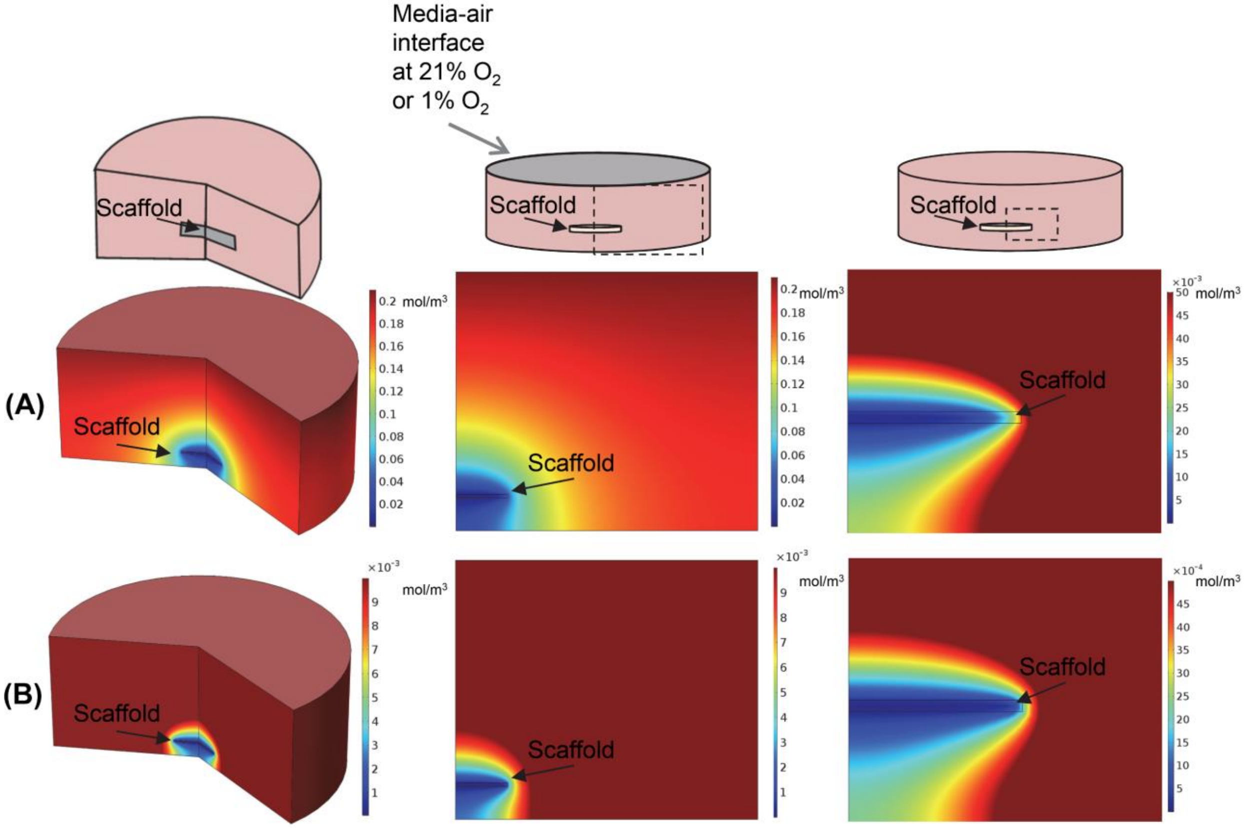

Figure 3.2. Mathematical modeling of oxygen gradients in scaffolded culture.
COMSOL Multiphysics software was used to model potential oxygen gradients in (A) scaffolded ambient oxygen culture (21% O_2) and (B) scaffolded low oxygen culture (1% O_2). Diffusion and consumption of oxygen was modeled using 3D axiosymmetric modeling of a 6-well plate, with a total cell number of 5 x 10^5 cells in the scaffold. The media air interface was assumed to be at ambient (21%) or low (1%) oxygen. Uniform consumption of oxygen within the scaffold was assumed, all materials were assumed to have the properties of water at 37°C.

3.3.3. Cell distribution throughout the silk scaffolds

To understand cell distribution throughout the silk scaffolds, a series of image-based analysis were performed. Cells grown on the scaffold in ambient (21%) and low oxygen (1%) conditions for 3 d were visualized through confocal imaging (surface), SEM (surface), and histology of the vertical cross section of the scaffold (**Figure 3.3**). In both ambient and low oxygen conditions, cells adhered to the scaffolds, with pockets of cells forming inside of the silk pores. This was demonstrated through confocal and SEM images of the surface (**Figure 3.3**). Cells attached to the silk, forming a robust layer of cells at the surface of the scaffold. Hematoxylin and eosin staining of scaffold cross sections confirmed a uniform distribution of cells throughout the scaffold (**Figure 3.3**). No major differences in cell morphology were observed between cells cultured in ambient and low oxygen.

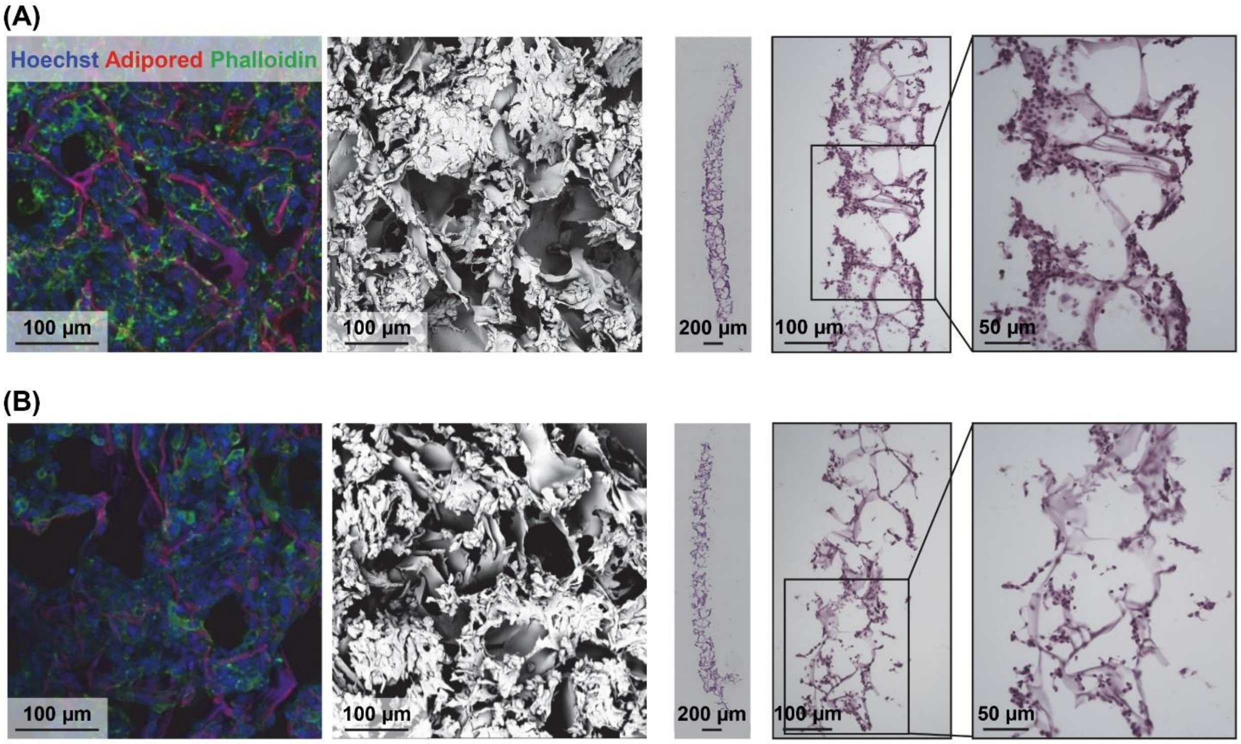

Figure 3.3. Morphology of cells grown on silk scaffolds.
(A) ambient (21%) and (B) low (1%) oxygen scaffolded SK-N-AS NB cells grown for 3 d. Images left to right: whole mount confocal imaging of scaffold surface, SEM imaging of scaffold surface, hematoxylin and eosin stain of a vertical section of the scaffold.

3.3.4. Viability of cells under different culture conditions

To determine the impact of scaffolded culturing on cell viability, scaffolds were evaluated for dsDNA content, proliferation (ki67), and apoptosis (TUNEL). After 3 d of culture cells in different culture conditions were analyzed for DNA content using a PicoGreen™ assay (**Figure 3.4 A)**. Analysis of dsDNA demonstrated no significant differences in DNA content based on culture condition. However, the DNA content did follow a trend where monolayer culture contained a higher level of DNA as compared to scaffolded culture, and ambient oxygen culture conditions had a higher level of dsDNA as compared to low oxygen cultures. In both ambient and low oxygen culture, positive staining for proliferation was observed (**Figure 3.4 B, C**). In addition, limited apoptosis was observed in scaffolded ambient and low oxygen (**Figure 3.4 D, E**). This suggests the presence of viable cells grown on scaffolds in both ambient and low oxygen.

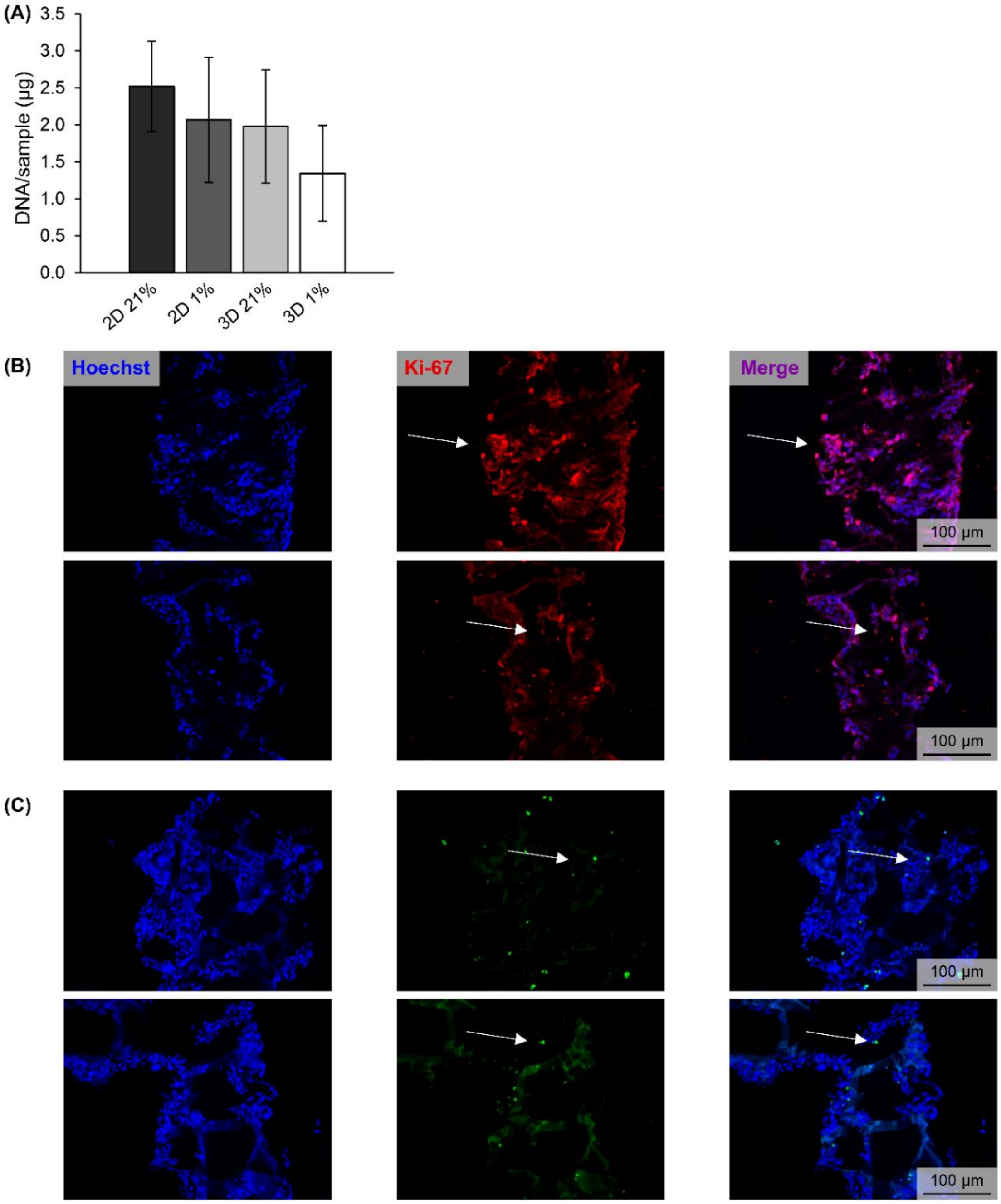

Figure 3.4. Analysis of cells under different growth conditions.

(A) Quantification of DNA content in each culture conditions after 3 d. Data is presented as mean ± SD for three independent experiments. SK-N-AS seeded scaffolds after 3 d of growth in scaffolded culture under (B) ambient (21%) and (C) low (1%) oxygen evaluated for Ki-67 expression. SK-N-AS seeded scaffolds after 3 d of growth in scaffolded culture under (D) ambient (21%) and (E) low (1%) oxygen evaluated apoptosis using a TUNEL stain. Arrows denote areas of positive staining.

3.3.5. Impact of scaffolded and low oxygen culturing on hypoxia-induced genes

To understand the role of hypoxia in scaffolded culture, hypoxia-related gene expression was evaluated after cell growth in monolayer and scaffolded culture in both ambient and low oxygen culture for 3 d. Known hypoxia-induced genes, *VEGF*, *CAIX*, *GLUT1*, *IGFBP3*, and *MMP9*, were evaluated (**Figure 3.5 A)**. Low oxygen culturing in monolayer upregulated *VEGF*, *CAIX*, *GLUT1*, and *IGFBP3* (8.6, 1122.1, 8.3, and 7.5-fold, respectively), with a non-significant trend toward increased *MMP9* expression (2.41-fold). Scaffolded ambient oxygen culture significant increased *VEGF*, *CAIX*, *GLUT1*, and *MMP9* (5.7, 444.2, 5.6, and 35.0-fold, respectively). These increases, while significant, were less robust than the monolayer low oxygen culture for all genes except *MMP9*. A non-significant increase in *IGFBP3* was also observed (5.2-fold). These increases suggest hypoxic conditions developing in the scaffolded culture. Cells grown in scaffolded, low oxygen cultures exhibited the greatest upregulation of hypoxia related genes. *VEGF*, *CAIX*, *GLUT1*, *IGFBP3*, and *MMP9* were all significantly upregulated (21.0, 2152.8, 13.8, 70.7, and 312.9-fold, respectively). This data followed an increasing trend from scaffolded ambient, monolayer low, to scaffolded low oxygen cultures, for all genes except *MMP9* where the monolayer low oxygen culture did not exhibit increased expression. Other evaluated genes can be found in **Appendix III**. Similar trends in hypoxia related genes were observed in KELLY and SH-SY5Y NB cells (**Figure 3.6**). KELLY cells in scaffolded low oxygen culture exhibited significant increases in *VEGF*, *CAIX*, *GLUT1*, *IGFBP3*, and *MMP9* (8.5, 320.1, 5.9, 11.1, 13.9-fold respectively) (**Figure 3.6 A**). SH-SY5Y cells grown in scaffolded low oxygen culture also demonstrated similar results with increases of 3.0, 153.7, 3.0, and 5. 4-fold in *VEGF*, *CAIX*, *GLUT1*, and *MMP9*, respectively (**Figure 3.6 B**). SH-SY5Y cells exhibited a limited response as compared to KELLY and SKNAS cells. This is as expected as SH-SY5Y cells have been demonstrated to have a suppressed hypoxia response [58].

3.3.1. Presence of hypoxia in scaffolded cultures

Next we sought to verify regions of hypoxia in scaffolded culture. Scaffolds were treated with pimonidazole for the final 24 h of culture at a concentration of 300 µM. Pimonidazole binds to thiol-containing proteins only stable under hypoxic conditions and has previously been used to identify hypoxia *in vitro* and *in vivo* [35, 59, 60]. Scaffolded SK-N-AS cells in both ambient and low oxygen demonstrated positive pimonidazole staining (**Figure 3.5 B, C**). These results were consistent with the observed hypoxia-related genes expression changes. In addition, cells on the scaffolds stained positive for glycogen accumulation, a metabolic adaptation common in tumor cells and promoted by hypoxia (**Figure 3.7 A, B**).

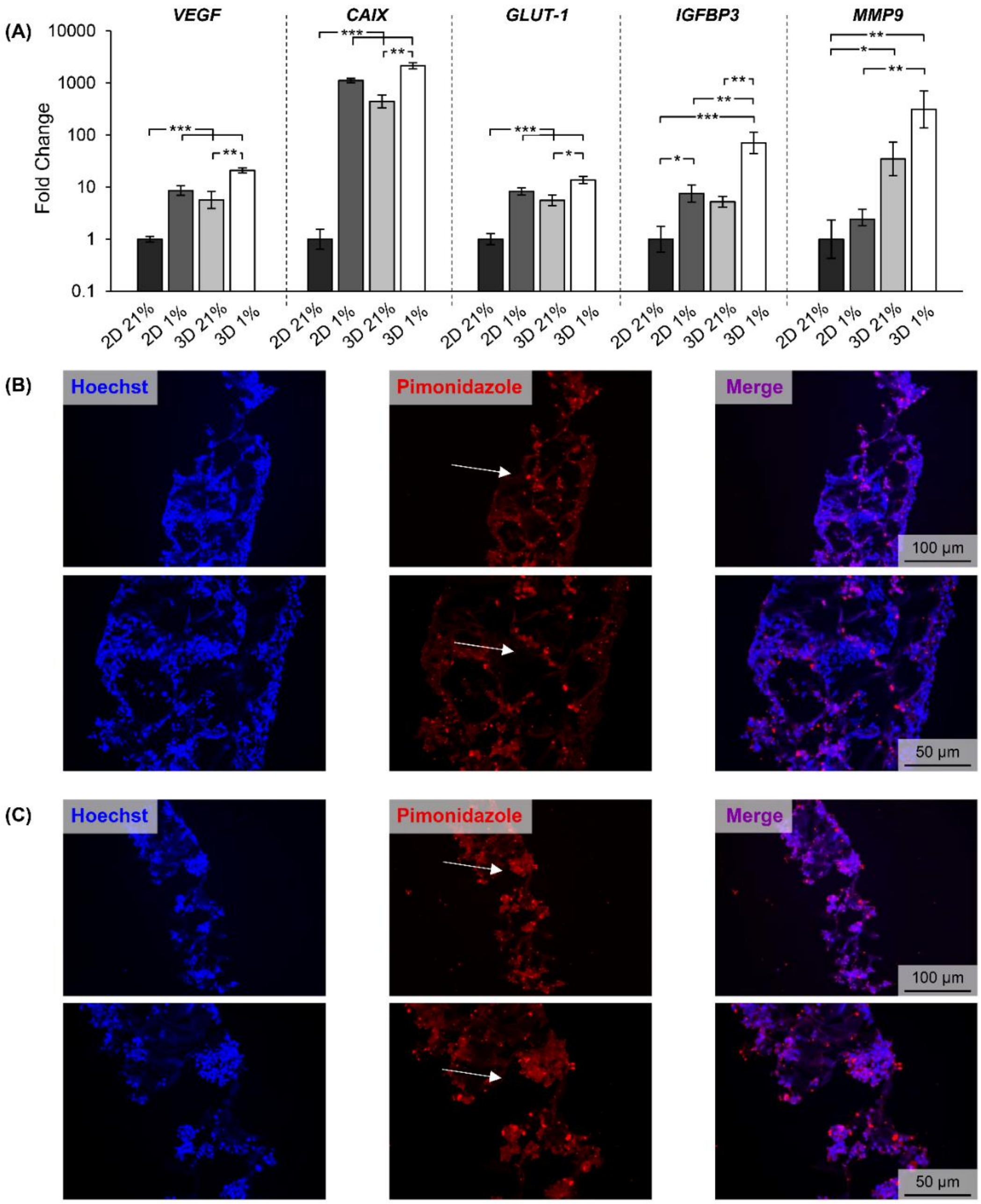

Figure 3.5. Impact of scaffolded growth and hypoxia on hypoxia related genes and presence of hypoxia in 3D.

(A) Hypoxia related gene expression of SK-N-AS NB cells grown for 3 d in monolayer (2D) or silk scaffolds (3D) in ambient (21%) oxygen or low (1%) oxygen, normalized to 2D 21% condition. Data is presented as mean ± SEM of minimum of three independent experiments. Asterisk indicate statistical significance between the groups (*$p < 0.05$, **$p < 0.01$, ***$p < 0.001$). SK-N-AS seeded scaffolds after 3 d of growth in scaffolder culture under (B) ambient (21%) oxygen or (C) low (1%) oxygen stained for pimonidazole to confirm regions of hypoxia. Arrows denote areas of positive staining.

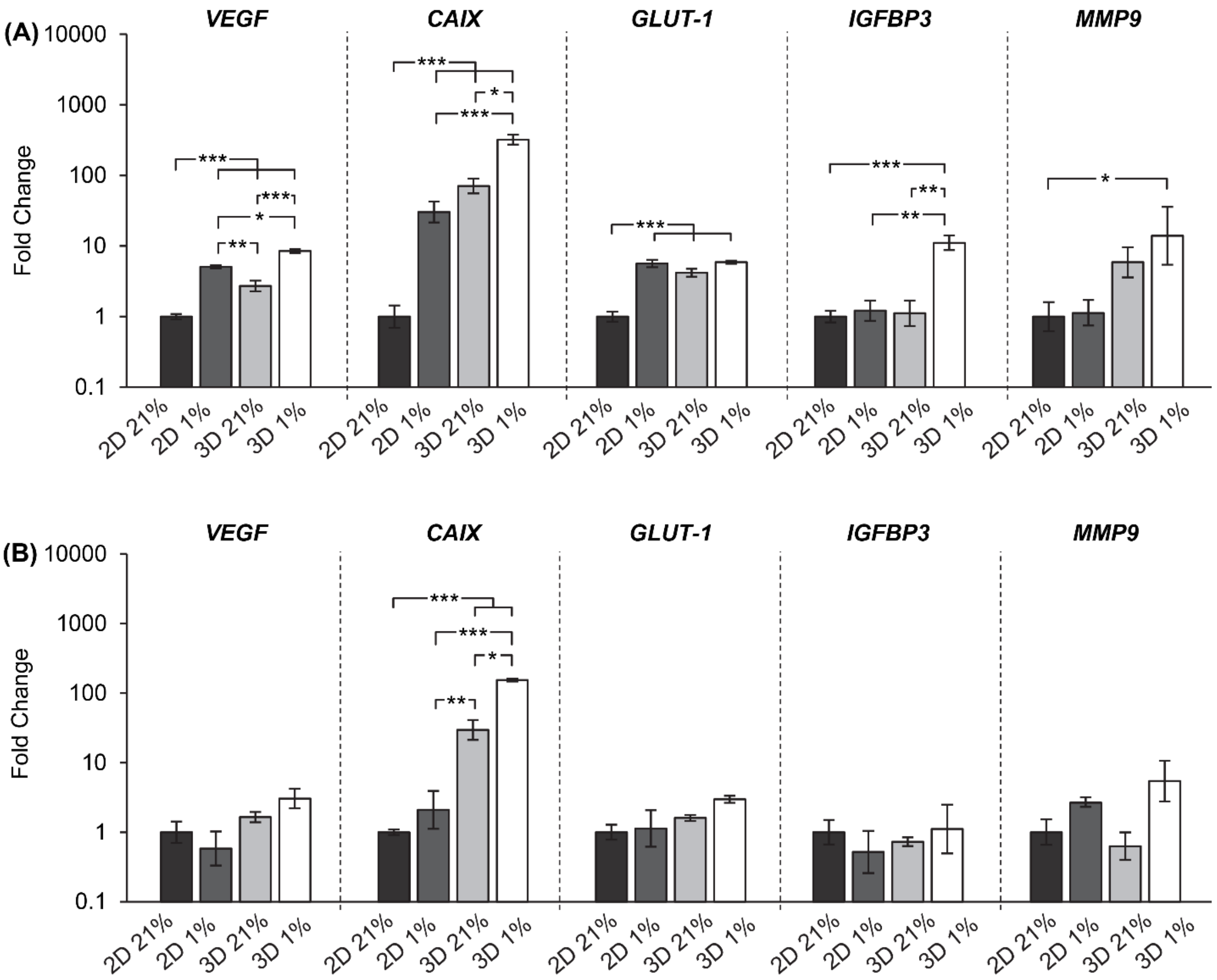

Figure 3.6. Impact of scaffolded growth and hypoxia on hypoxia related genes in other NB cell lines.

Hypoxia related gene expression of (A) KELLY NB cells or (B) SH-SY5Y NB cells for 3 d in monolayer or silk scaffolds in 21% oxygen or 1% oxygen, normalized to 2D 21% condition. Data is presented as mean ± SD for three independent experiments. Asterisk indicate statistical significance between the groups (*p < 0.05, **p < 0.01, ***p < 0.001).

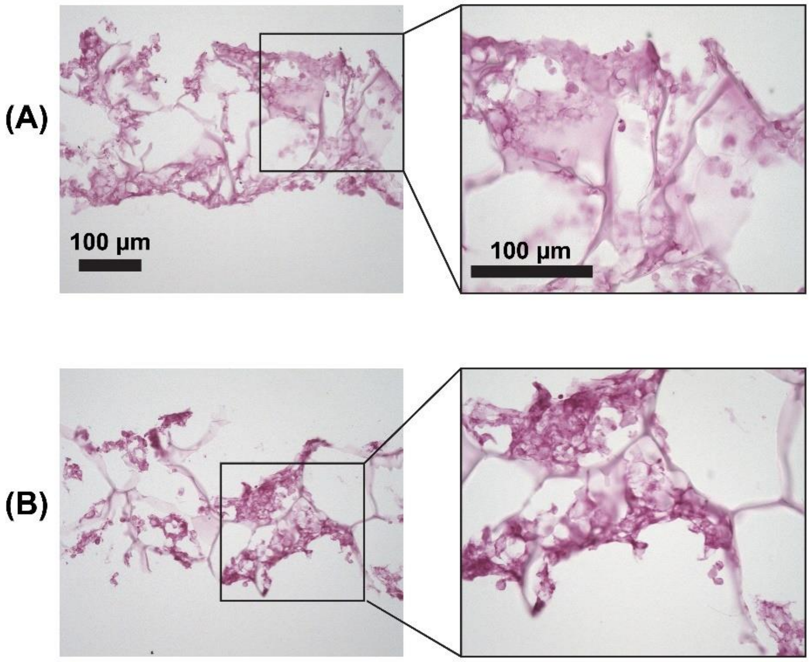

Figure 3.7. Presence of glycogen in scaffolded culture.
SK-N-AS seeded scaffolds after 3 d of growth under (A) ambient (21%) and (B) low oxygen stained for glycogen accumulation using PAS.

3.3.2. Impact of scaffolded and low oxygen culturing on cytokine secretion

Next, we examined the impact of oxygen concentration and scaffolded culture on cytokine secretion. A cytokine array was used to examine cytokine secretion in the medium of monolayer and scaffolded cultures at low and ambient oxygen after 3 d of culture (**Figure 3.8 A, B , Table 3.2**). Scaffolded NB and low oxygen monolayer cultures secreted increased levels of ITAC, VEGF-A, MIF, MIP, CCL3, and uPAR. Scaffolded NB exhibited increased secretion of pro-inflammatory cytokines GM-CSF, IL-8, and MCP-3 as compared to ambient and hypoxic monolayer cultures suggesting that 3D culturing independently contributes to changes in cytokine secretion. Dot blot hits of IL-8, GM-CSF, MCP-3, and VEGF-A were confirmed through ELISAs (**Figure 3.8 C)**. Secretion profiles of hypoxic and scaffolded culture consistent with that of the dot blot with were observed. Specifically, secretion of VEGF increased with similar increases observed in monolayer low oxygen and scaffolded ambient culture and with the highest secretion observed in scaffolded low oxygen. Secretion of MCP-3, GM-CSF, and IL-8 demonstrated large increases in both scaffolded culture conditions similar with the results observed on the dot blot.

To confirm dot blot results, gene expression for the inflammatory markers *IL-8*, *GM-CSF*, *MCP-3*, and *ITAC* was evaluated (**Figure 3.8 D)**. Monolayer cultures under low oxygen did not increase *IL-8, GM-CSF*, *MCP-3*, and *ITAC* expression. Scaffolded ambient oxygen culture significantly increased *IL-8*, *GM-CSF*, *MCP-3*, and *ITAC* expression (138.6, 24.4, 32.9, 21.7 fold, respectively). Similar results were observed in scaffolded low oxygen cultures, with increased *IL-8*, *GM-CSF, MCP-3*, and *ITAC* (247.0, 32.7, 45.2, and 17.8 fold, respectively) (**Figure 3.8 D**). No differences were observed between scaffolded ambient and scaffolded low oxygen. Additional dot blot hits such as G-CSF were also evaluated. However, a subset of them including G-CSF, CCL3, and IL-6, all of which have been clinically linked to poor prognosis in NB failed to amplify consistently in all conditions with the exception of scaffolded low oxygen culture [61-68]. This further indicates that scaffolded culture with regions of hypoxia is necessary to mimic clinical NB. A full table of clinical correlation between gene and cytokine changes can be found in **Appendix VII.**

Cytokine secretion of KELLY NB cell was evaluated to compare secretion profiles between cell lines (**Figure 3.9 A, B, Table 3.3**). KELLY NB cells demonstrate limited changes in cytokine secretion under scaffolded culture and low oxygen. Hypoxia (scaffolded and monolayer) related increases in VEGFA were confirmed via ELISA assay (**Figure 3.9 C**). Visual analysis of the dot blots suggested lower overall levels of secretion in KELLY cells as compared to SK-N-AS cells. This could be due differences in NB pathways and heterogeneity between tumor cell lines.

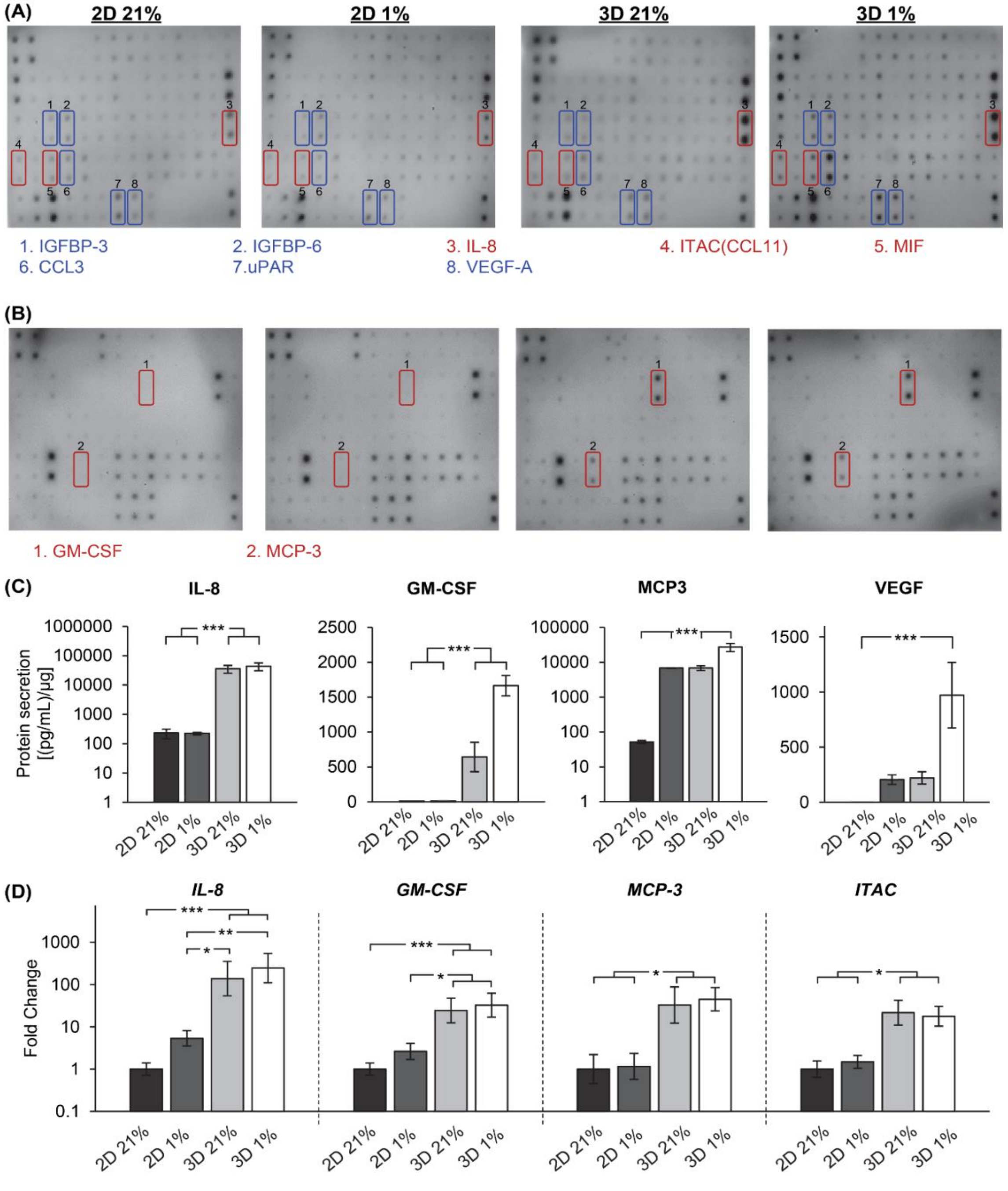

Figure 3.8. Impact of scaffolded growth and hypoxia on SK-N-AS cytokine secretion. (A), (B) Dot blot images of conditioned SK-N-AS media after 3 d of culture in monolayer (2D) and scaffolded (3D) culture in ambient (21%) or low (1%) oxygen (A: Array C7; B: Array C6 from RayBiotech Human Cytokine Array C1000). Blue and red boxes represented changes driven by hypoxic conditions and scaffolded culturing, respectively, as determined by protein secretion and/or gene expression changes. (C) ELISA validation of select dot blot hits normalized to DNA content of each sample. (D) Gene expression validation of select dot blot hits. Data is presented as mean ± SEM for three independent experiments. Asterisk indicate statistical significance between the groups (*$p < 0.05$, **$p < 0.01$, ***$p < 0.001$).

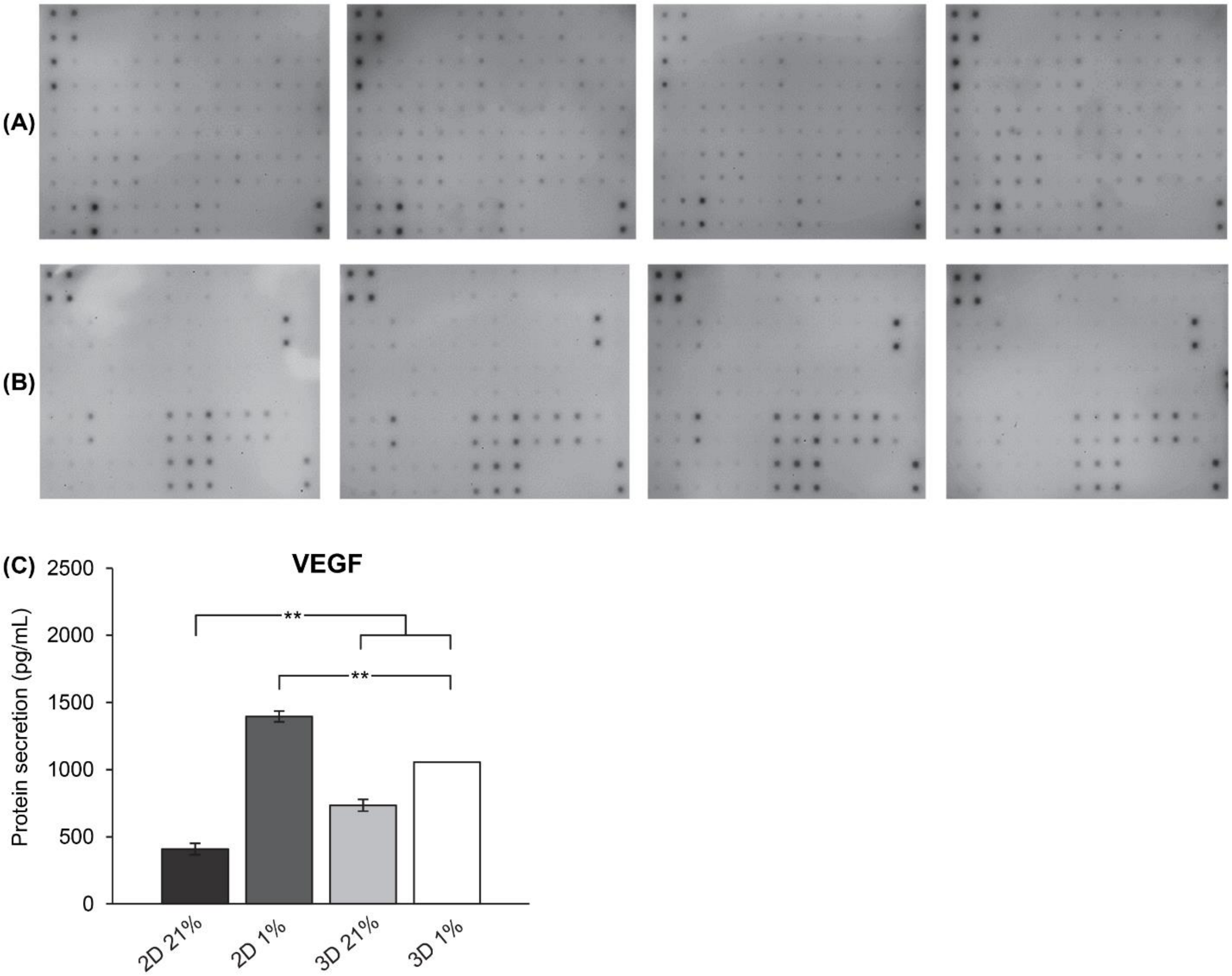

Figure 3.9. Impact of scaffolded growth and hypoxia on KELLY cytokine secretion. (A), (B) Dot blot images of conditioned KELLY NB cell media after 3 d of culture in monolayer (2D) and scaffolded (3D) culture in ambient (21%) or low (1%) oxygen (A: Array C7; B: Array C6 from RayBiotech Human Cytokine Array C1000). (C) KELLY NB cell VEGF secretion via ELISA assay. Data is presented as mean ± SD for three independent experiments. Asterisk indicate statistical significance between the groups (**$p < 0.01$).

3.3.3. Impact of scaffolded growth and hypoxia on *MYCN* gene expression

Previous work has demonstrated that hypoxia contributes to aggressive tumor phenotypes [7, 10, 14, 58, 69, 70]. Amplified MYCN is considered one of the hallmarks of aggressive NB [71-75]. The impact of hypoxic culture as well as scaffolded growth on *MYCN* expression was examined in three different cell lines (**Figure 3.10**). Scaffolded low oxygen culture of SK-N-AS (non-amplified MYCN) cells significantly increased *MYCN* expression. In KELLY NB cells (amplified MYCN) no difference in *MYCN* expression was observed in scaffolded and/or hypoxic culture. This is likely due to the higher baseline *MYCN* expression, as can be seen when comparing Ct values (**Table 3.4**). Interestingly, in SH-SY5Y (non-amplified MYCN) no increases were observed. While these cells demonstrated similar Ct values to SK-N-AS cells, they also contain a mutation in anaplastic lymphoma kinase [76] and have been demonstrated to be less responsive to hypoxia, both in literature and our analysis of hypoxic genes (**Figure 3.6 B**) [58].

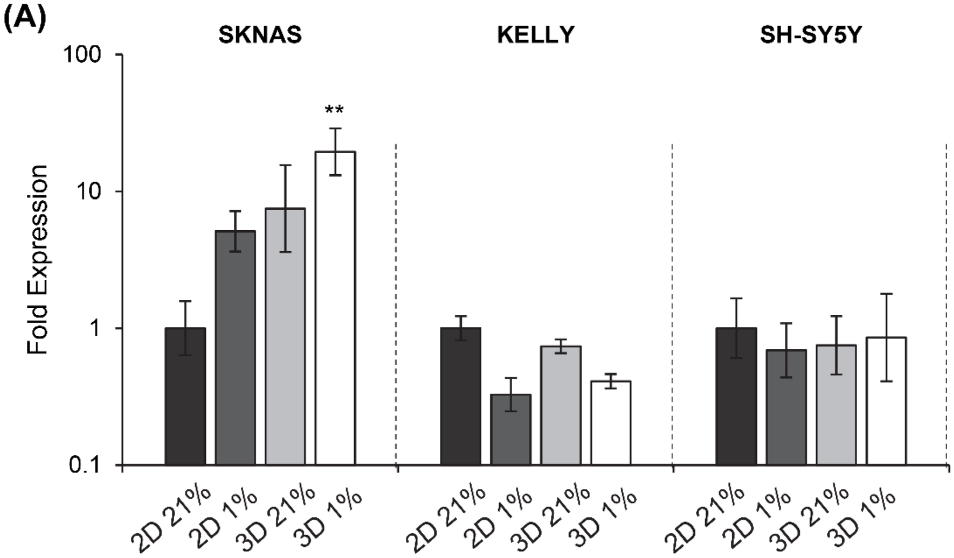

Figure 3.10. Impact of scaffolded growth and hypoxia on MYCN expression.
MYCN expression by three different NB cell lines after 3 d of culture in monolayer (2D) and scaffolded (3D) in ambient (21%) or low (1%) oxygen. Data is presented as mean ± SEM for three independent experiments. Asterisk indicate statistical significance between the groups (**$p < 0.01$).

3.3.4. Cell sensitivity to cytotoxic drugs

To determine the impact of scaffolded and low oxygen culture on therapeutic sensitivity, we evaluated the cell response to etoposide, a chemotherapy drug, and tirapazamine, a hypoxia-responsive drug (**Figure 3.11**). Monolayer cultured SK-N-AS cells exhibited similar sensitive to etoposide between ambient and low oxygen conditions when treated with 1 µM and 10 µM etoposide (viabilities of 55.2 ± 14.2% vs. 50.9 ± 8.6 % and 27.3 ± 8.9% vs. 20.5 ± 4.1% viability, respectively) (**Figure 3.11 A**). Culturing NB cells under ambient and low oxygen scaffolded conditions reduced cell sensitivity to 1 µM and 10 µM (viabilities of 96.6 ± 7.8% and 88.9 ± 13.0% and 85.7 ± 5.1% and 78.6 ± 19.7% viability, respectively) suggesting that cells grown in scaffolds are less responsive to etoposide than cells grown in monolayer(**Figure 3.11 A**).

Monolayer cultured SK-N-AS cells in low oxygen demonstrated a greater response to tirapazamine, an inhibitor that is selectively activated in hypoxia as compared to ambient oxygen culture when treated with 2 µg/mL and 20 µg/mL tirapazamine (viabilities of 87.0 ± 15.9% vs. 43.2 ± 13.4% and 62.0 ± 14.4% vs. 10.0 ± 5.6% viability, respectively) (**Figure 3.11 B**). Culturing cells under scaffolded low oxygen conditions demonstrated a similar response to monolayer low oxygen to 2 µg/mL and 20 µg/mL tirapazamine (viabilities of 58.0 ± 20.4% and 16.3 ± 3.7%, respectively) (**Figure 3.11 B**). While there were no significant differences observed in 2D monolayer low oxygen culture as compared to scaffolded 3D low oxygen, differences were observed under ambient oxygen culture conditions. Scaffolded 3D culture showed increased sensitivity to 20 µg/mL tirapazamine as compared to monolayer 2D culture under ambient oxygen conditions (31.7 ± 13.4% and 88.0 ± 16.2% viability, respectively). At a lower dose of 2 µg/mL tirapazamine, there was no significant difference in response from scaffolded 3D versus monolayer 2D culture under ambient oxygen conditions. This suggests that the hypoxic regions within cell seeded scaffolds can be targeted therapeutically by hypoxia-sensitive therapies.

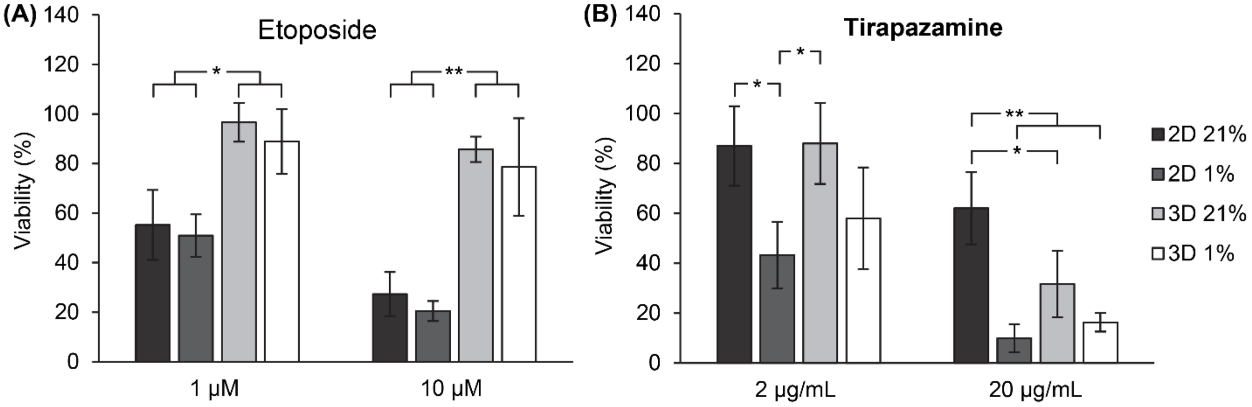

Figure 3.11. Differential response of cells grown in scaffolded culture and hypoxia to therapeutics.
Response of cells to (A) etoposide and (B) tirapazamine in monolayer (2D) and scaffolded (3D) culture in ambient (21%) or low oxygen (1%). Viability is determined via comparison of dsDNA content. All conditions were normalized to an untreated control. Data is presented as mean ± SD for three independent experiments. Asterisk indicate statistical significance between the groups (*p < 0.05, **p < 0.01).

3.4. Discussion

NB is a heterogeneous disease with limited treatment options and poor prognosis [3, 77]. The current models used to assess therapeutics and identify critical pathways are limited. Specifically, they lack cell-cell interacts as well as oxygen and nutrient gradients present *in vivo.* Here we present the development of a model system that incorporates 3D culturing as well as low oxygen conditions to better mimic the tumor microenvironment and bridge the gap between traditional monolayer cultures and preclinical murine models.

In this work, a scaffolded *in vitro* NB model was developed using lyophilized silk scaffolds. Silk fibroin is a versatile, non-immunogenic biomaterial that can be processed into a porous structure capable of sustaining cell growth using lyophilization [41, 45]. Our studies demonstrate that cells grew throughout the silk scaffolds under different oxygen conditions. Cells attached to the silk scaffold and grew throughout the pores, exhibiting cell-cell interactions as well as cell-material interaction. It has been well established in literature that 100 µm is a critical thickness for oxygen and nutrients *in vivo* furthermore, *in vitro* spheroids typically begin to demonstrate hypoxia when they reach a radius of 100 µm [78]. To allow for cell growth throughout the scaffold and cell-driven oxygen gradients, a scaffold thickness of 200 µm was utilized. . While the scaffold and seeding properties (i.e. scaffold thickness, number of cells seeded) allowed for fabrication of cell driven gradients using highly metabolic NB cancer cells, scaffold properties could be tuned for different cancer types to support cell-driven gradient formation. Additional properties of the silk scaffolds that could be varied include pore size, stiffness, and chemical properties to further impact cell responses and better understand the role each property plays in tumor aggressiveness.

In our system we demonstrate that silk scaffolds can sustain viable cells in both ambient and low oxygen. This was demonstrated through quantification of dsDNA after 3 d of culture as well as ki67 (proliferation) and TUNEL staining. Quantification of dsDNA demonstrated a trend in DNA content where cells grown in low oxygen (both in monolayer and scaffolded conditions) demonstrated reduced dsDNA as compared to cells grown their ambient oxygen counterparts. In many cancer types hypoxia has been demonstrated to reduce cell proliferation, as proliferation with a high number of metabolic cells would exacerbate hypoxic stress [79, 80]. Positive staining for proliferation (Ki-67) was observed. While typically observed as a nuclear stain, our cells exhibited a mixture of nuclear and cytoplasmic staining. Previous literature using other cancer cell types have reported this observation, though the reason for cytoplasmic Ki-67 protein is not fully understood [81-83]. Limited TUNEL staining was observed suggesting that at 3 d, hypoxia within the scaffolds is not causing a high level of apoptosis.

Hypoxia is a critical factor in tumor progression and prognosis. Traditional monolayer *in vitro* cultures fail to accurately mimic hypoxic regions present in the tumor environment. In this study, hypoxia was induced by cell-driven oxygen consumption and controlled for using a low oxygen incubator. The presence of hypoxic regions in the scaffolds was confirmed through COMSOL modeling, upregulation of hypoxia-related genes and positive pimonidazole staining. COMSOL modeling suggests that scaffolded low oxygen culture exhibited the highest amount of hypoxia, followed by monolayer low oxygen culture and scaffolded ambient oxygen culture. Furthermore, COMSOL modeling suggested physiologically relevant oxygen gradients. Modeling of scaffolded, ambient oxygen cultures demonstrated regions of hypoxia (<1%) as well as physiologic oxygen levels (3-5%) Thus, COMSOL modeling suggest that scaffolded ambient oxygen culture may be similar to the gradient exhibited within the tumor that ranges from 4% to hypoxic levels.

Gene expression changes corroborated the COMSOL modeling, with consistent upregulation of known hypoxia markers. This included HIF down-stream target VEGF, which is known to contribute to tumor survival and invasion [16]. CAIX expression has been demonstrated to be induced by hypoxia [69, 84]. It functions to regulate pH by accelerating the conversion of CO_2 and H_2O to HCO_3^- and H^+, helping to maintain a more alkaline intracellular pH [84]. GLUT1 expression has been demonstrated to be upregulated under hypoxic conditions as part of an altered metabolic pathway and correlated to high malignant potential and poor prognosis[85]. Clinically, increased GLUT1, CAIX, and VEGF have been correlated with advanced NB [69, 85-87]. In addition to directly transcribing VEGF, CAIX, and GLUT1 as transcription targets, HIF has been demonstrated to function as parts of key pathways such as PI3K, MAPK, and NFκB. For example, VEGF has been demonstrated to stimulate MAPK, and MMP9 activity is promoted by ERK and

PI3K activity. In addition, we observed glycogen accumulation in the scaffolded culture. Glycogen accumulation has been observed in hypoxia in multiple cancer types [88-92]. Metabolically, GLUT1 can increase uptake of the accumulated glycogen to promote cell survival in oxygen deprovision [88]. The impact of both hypoxia and scaffolded culture on downstream targets of these pathways specific to individual tumors could be elucidated utilizing this system. Previous work using monolayer cells under 1% O_2 conditions, identified hypoxia-related changes in *VEGF*, *CAIX*, *GLUT1*, and *MMP9* in NB. However, previous studies did not directly compare scaffolded culturing (that likely contain low oxygen regions) to monolayer culturing in low oxygen. These direct comparisons allow for a more complex understanding of the impact on 3D culture as compared to changes driven by hypoxia.

In the tumor microenvironment, low levels of oxygen and nutrients can recruit immune cells and stromal cells, induce cell transformation, and promote malignancy through increased cytokine secretion [93, 94]. It is well established that significant differences in cytokines exist between the *in vivo* tumor microenvironment and traditional monolayer *in vitro* culture [95, 96]. In this work, we demonstrated differential cytokine secretion based on both hypoxia and scaffolded growth. The proinflammatory cytokines IL-8, GM-CSF, MCP-3, and ITAC exhibited significant upregulation in scaffolded conditions. Clinically, the pro-angiogenic cytokine IL-8 expression has been demonstrated in tumor samples, as compared to minimal expression in the near-by adrenal tissue, suggesting it is a relevant part of the tumor microenvironment [97]. GM-CSF, a commonly used cytokine in NB therapy has been demonstrated to have both a stimulatory and suppressive effect in tumors [98]. It functions as an immunomodulator, stimulating dendritic, monocyte, and macrophage activity [99]. Studies have also demonstrated that GM-CSF stimulates tumor growth and metastasis in several cancers [98]. MCP3 (CCL7) has not yet been clinically linked to NB.

However, in other cancers MCP3 has been linked with a decreased in relapse-free survival, increased numbers of cancer associated fibroblasts, recruitment of macrophages, and enhanced tumor metastasis [100-102]. ITAC ligand for the receptor CXCR3 and a chemotactic for activated T-cells. In other cancers, ITAC has been demonstrated to attract CD8+ lymphocytes and macrophages, as well as enhancing tumor cell growth and metastasis [103]. Taken together, these cytokine changes suggest that scaffolded NB culture provides a more physiologically relevant tumor microenvironment, as compared to monolayer hypoxic culture.. Further, many cytokines that were upregulated in hypoxic culture such as uPAR, CCL3, and VEGF demonstrated similar upregulation in scaffolded culture. To better mimic the tumor phenotype, a combination of cell-driven oxygen gradients and the scaffolded NB approaches well as 3D culture (cell-cell interactions) is necessary.

Hypoxia, both cell-driven due to scaffolded culture and induced through low oxygen conditions, induced secretion of cytokines. However, a subset of cytokines was induced in scaffolded culture, but not in monolayer, low oxygen culture. This suggests that scaffolded culture and cell driven gradients were able to induce secretion of cytokines that hypoxia alone was not able to induce. This suggests that scaffolded culture is capable of secreting hypoxia-related cytokines, but hypoxic culture (not in 3D) does not exhibit the same secretome profile as scaffolded cells.

Differences were observed between different NB cell lines and cytokine secretion. While secretion of hypoxia-related cytokines such as VEGF was conserved between monolayer ambient and low oxygen culture across cell lines, there were large differences in inflammatory cytokine secretion. These differences exhibited between cell lines, would likely be observed with patient tumors due to the heterogenous nature of this cancer [104]. Differences in gene expression and cytokine secretion could be evaluated in patient-derived tumor samples to understand the aggressive tumor microenvironment in the hypoxic tumor core to develop patient-specific treatment strategies. Our studies were performed with three established NB cell lines, SK-N-AS, KELLY, and SH-SY5Y. These changes include MYCN amplification, characterized by extra copies of MYCN. KELLY cells exhibit MYCN amplification, while SH-SY5Y and SK-N-AS do not [105]. This allowed for understanding of how our system responded to heterogeneity in NB. Further, SH-SY5Y has been previously demonstrated to a limited hypoxic response, potentially due to pathway expression or degree of differentiation [58].

The goal of understanding different tumor properties is to develop more effective therapeutics for individual tumor subtypes and patients. It has been well established that response of cells to therapeutics in monolayer culture is not indicative of clinical response [25, 106, 107]. This is due to differences in pathway activation, diffusion barriers, and resistance developed by the cell microenvironment. In this study, cells grown in scaffolded cultures, both in ambient oxygen and hypoxia, demonstrated resistance to the clinically used chemotherapeutic etoposide as compared to monolayer culture. Tirapazamine, which is activated to a toxic radical in hypoxia, was tested to determine if this trend was conserved with other therapeutics. In monolayer culture, hypoxia was able to significantly enhance the toxicity of tirapazamine. Scaffolded low oxygen cultures also demonstrated similar toxicity. Interestingly, when treated with 20 µg/mL of tirapazamine, scaffolded culture in ambient oxygen demonstrated increased responsiveness as compared to monolayer cultures under ambient oxygen conditions. This suggests that testing of therapeutics both in 3D and at different oxygen levels may represent an improved platform for preclinical drug screening.

3.5. Conclusions

This work establishes a scaffolded tumor model using lyophilized silk scaffolds capable of mimicking physiologically relevant oxygen gradients. Use of controlled oxygen incubators in combination with this scaffolding method has the potential to drive fundamental understanding of pathway changes relevant to scaffolded culture and hypoxia. Examination of cytokine secretion and gene expression suggests a more physiologically relevant tumor microenvironment with the scaffolded culture. NB grown within the scaffolded 3D cultures exhibited changes in critical oncogenic pathways such as MYCN, as well as resistance to clinically used chemotherapeutics. This culture method represents an initial link between physiological tumor and *in vitro* culture. However, while this model captures critical signaling pathways present in the tumor microenvironment, there is still a high degress of cell heterogeneity present in the tumor microenvironment. In the future, this platform could be expanded to incorporate other integral cells of the tumor microenvironment such as stromal and immune cells to enhance the complexity of the model and expanded to study additional tumor types.

3.6. Acknowledgements

The authors wish to thank Katelyn Mistretta for her work with the SH-SY5Y cells, Emily Newman for assistance in performing the dotblots, writing the dotblot analysis software, and assistance with cell seeding studies, and Coulter Ralston for his assistance with the cell seeding studies.

Table 3.1. List of primers used for qRT-PCR in Aim 1

Gene	Sequence
CAIX	F - GGGTGTCATCTGGACTGTGTT R - CTTCTGTGCTGCCTTCTCATC
GLUT1	F - CCTGCAGTTTGGCTACAACA R - GTGGACCCATGTCTGGTTG
GM-CSF	F - GGGAGCATGTGAATGCCATC R- GGCTCCTGGAGGTCAAACAT
IGFBP3	F - TCTGCGTCAACGCTAGTGC R - GCTCTGAGACTCGTAGTCAACT
IL-8	F - AAGACATACTCCAAACCTTTCCACC R - CTTCAAAAACTTCTCCACAACCCT
ITAC	F - GACGCTGTCTTTGCATAGGC R - GGATTTAGGCATCGTTGTCCTTT
MCP-3	F - TCTCATGTGGAAGCCCATGC R - GTATTAATCCCAACTGGCTGAGCA
MMP9	F - TTCTGCCCGGACCAAGGATA R - ATGCCATTCACGTCGTCCTT
MYCN	F - CGACCACAAGGCCCTCAGT R - TGACCACGTCGATTTCTTCCT
VEGF	F - AGGAGGAGGGCAGAATCATCA R - CTCGATTGGATGGCAGTAGCT
SDHA (housekeeper)	F - TGGGAACAAGAGGGCATCTG R - CCACCACTGCATCAAATTCATG

Table 3.2. Analysis of cytokine section by SK-N-AS cells

Secreted Factor	2D 1%[a]	3D 21%[a]	3D 1%[a]
1-309 (CCL1)	0.76	0.63	0.00
Adiponectin (ACRP30)	1.86	2.04	2.32
AgRP	1.69	1.28	2.10
Angiogenin	0.83	0.56	0.50
ANGPT2	2.27	2.66	2.83
AR	2.25	2.44	2.80
Axl	2.85	2.39	3.55
BDNF	0.96	1.63	0.53
beta-NGF	2.81	3.45	3.49
bFGF	3.12	3.87	3.89
BLC (CXCL13)	1.17	0.95	0.69
BMP-4	0.64	1.25	0.93
BMP-6	0.90	0.50	0.58
BTC	3.05	2.18	3.79
CCL28 [108]	2.53	2.26	3.15
CK beta 8-1 (CCl23)	0.18	1.12	0.92
CNTF	1.10	1.03	1.01
CTACK (CCL27)	1.19	1.87	1.48
Dtk	0.96	1.36	1.19
EGF	1.01	0.65	1.27
EGFR	1.51	2.04	1.87
ENA-78 (CXCL15)	1.89	2.48	2.35
Eotaxin-1 (CCL11)	0.93	2.31	1.47
Eotaxin-2 (CCL24)	0.65	1.03	0.21
Eotxin-2 (CCL26)	0.94	0.95	0.67
Fas (Apo-1)	2.59	3.42	3.22
FGF-4	2.32	2.76	2.88
FGF-6	0.83	1.05	0.60
FGF-7 (KGF)	1.10	0.83	0.34
FGF-9	2.23	2.65	2.77
Fit-3 Ligand	0.72	1.02	0.44
Fractalkine (CX3CL1)	0.70	0.90	0.49
GCP-2 (CXCL6)	0.76	0.82	0.61
G-CSF	3.59	3.70	4.47
GDNF	0.54	1.13	0.59
GITR (TNFRSF18)	2.48	2.88	3.08
GITR Ligand (TNFSF18)	2.54	2.69	3.16
GM-CSF	0.75	65.65	51.42
gp130	3.32	3.66	4.13

GRO	4.44	6.35	5.53
GRO alpha (CXCL1)	4.27	4.73	5.31
HCC4 (CCL16)	3.57	3.67	4.44
HGF	2.11	2.45	2.62
ICAM-1 (CD54)	1.69	4.19	2.10
ICAM-3 (CD50)	2.52	3.12	3.14
IFN-gamma	0.52	0.72	1.09
IGF-1	0.48	0.89	0.65
IGF-1R	2.84	4.19	3.53
IGFBP-1	0.00	1.02	0.55
IGFBP-2	0.62	0.94	1.18
IGFBP-3	2.47	3.77	3.07
IGFBP-4	1.11	0.38	0.37
IGFBP-6	3.28	2.09	4.08
IL_1 beta (IL-1 F2)	0.87	0.90	0.73
IL_12 p40	2.98	4.47	3.70
IL-1 alpha (IL-1 F1)	1.62	1.44	1.19
IL-1 ra (IL-1 F3)	0.64	1.26	0.80
IL-10	0.00	11.98	4.88
IL-11	2.36	2.87	2.94
IL-12 p70	3.49	4.63	4.34
IL-13	0.03	0.00	0.01
IL-15	0.88	1.09	0.87
IL-16	0.88	0.92	0.74
IL-17A	3.86	5.93	4.81
IL-1R1	2.98	4.10	3.71
IL-1R4 (ST2)	2.80	3.71	3.48
IL-2	0.75	0.94	0.34
IL-2 R alpha	3.41	5.12	4.24
IL-3	0.99	1.55	1.13
IL-4	0.89	1.73	1.22
IL-5	7.99	0.00	0.00
IL-6	0.00	1.22	2.35
IL-6R	3.74	5.09	4.65
IL-7	17.23	0.00	0.00
IL-8 (CXCL8)	3.66	20.80	4.55
I-TAC (CXCL11)	3.31	5.74	4.12
Leptin	0.50	1.00	0.70
LIGHT (TNSF14)	0.80	1.52	1.08
Lymphotactin	3.16	4.09	3.93
MCP-1 (CCL2)	0.84	1.70	1.01
MCP-2 (CCL8)	0.39	3.32	1.00

MCP-3 (MARC/CCL7)	1.16	14.19	9.78
MCP-4 (CCL13)	0.90	1.14	0.67
M-CSF	0.76	1.19	0.71
MDC (CCL22)	0.66	1.10	0.68
MIF	2.94	3.60	3.66
MIG (CXCL9)	0.64	0.99	0.82
MIP-1 delta (CCL15)	0.73	1.19	1.17
Mip-1-alpha (CCL3)	3.06	5.47	3.81
MIP-1-beta (CCL4)	2.96	4.57	3.68
MIP-3 alpha (CCL20)	0.65	1.26	1.54
MIP-3-beta (CCL19)	2.27	5.06	2.82
MSP (alpha/beta)	3.46	5.42	4.31
NAP-2 (CXCL7)	0.60	1.18	1.34
NT-3	0.63	0.91	0.94
NT-4	2.65	4.32	3.30
OPG (TNFRSF11B)	2.72	4.98	3.38
OSM	3.41	4.97	4.25
PARC (CCL18)	1.81	0.51	0.02
PDGF-BB	0.56	1.19	0.00
PLGF	3.95	6.77	4.91
RANTES (CCL15)	0.78	1.74	1.42
SCF	1.14	1.47	0.57
SDF-1 Alpha	0.57	1.33	0.47
TARC (CCL17)	0.51	1.20	0.66
TECK(CCL25)	1.94	3.83	2.41
TGF Beta 1	0.79	1.02	0.20
TGF Beta 3	0.62	1.40	1.09
TIMP-1	1.81	2.55	2.25
TIMP-2	2.51	2.95	3.12
TNF Alpha	0.50	1.08	1.01
TNF Beta	0.50	1.09	1.08
TNFRI (TNFRSF1A)	5.29	7.47	6.59
TNFRII (TNFRSF1B)	3.84	4.55	4.78
TPO	4.90	6.72	6.10
TRAIL R3	3.36	4.54	4.17
TRAIL R4	0.29	0.44	0.36
uPAR	2.87	2.68	3.57
VEGF-A	3.57	7.04	4.45
VEGF-D	2.57	3.66	3.20

[a]Fold Change Relative to 2D 21%

Table 3.3. Analysis of cytokine section by KELLY cells

Secreted Factor	**2D 1%**[a]	**3D 21%**[a]	**3D 1%**[a]
1-309 (CCL1)	1.40	0.61	1.17
Adiponectin (ACRP30)	2.33	1.62	2.52
AgRP	2.12	1.65	2.19
Angiogenin	1.08	0.69	0.65
ANGPT2	2.18	1.46	2.58
AR	2.08	1.89	2.72
Axl	1.68	1.49	2.64
BDNF	0.96	0.65	0.77
beta-NGF	0.00	0.00	0.00
bFGF	2.47	2.15	3.59
BLC (CXCL13)	0.91	0.67	0.92
BMP-4	1.13	0.67	0.93
BMP-6	0.49	1.05	1.29
BTC	0.81	1.68	2.58
CCL28 [108]	0.10	0.36	1.30
CK beta 8-1 (CCl23)	1.24	0.65	1.16
CNTF	1.47	0.75	1.58
CTACK (CCL27)	2.12	1.71	3.35
Dtk	2.01	1.96	2.59
EGF	1.43	0.98	1.99
EGFR	1.90	1.63	2.49
ENA-78 (CXCL15)	2.04	1.03	3.72
Eotaxin-1 (CCL11)	0.00	0.61	1.07
Eotaxin-2 (CCL24)	1.26	1.32	1.36
Eotxin-2 (CCL26)	1.00	0.93	1.01
Fas (Apo-1)	2.31	1.10	2.60
FGF-4	2.49	1.67	2.29
FGF-6	1.74	1.56	1.86
FGF-7 (KGF)	1.07	0.86	1.06
FGF-9	2.53	2.09	2.79
Fit-3 Ligand	0.72	0.44	0.28
Fractalkine (CX3CL1)	0.95	0.55	0.77
GCP-2 (CXCL6)	0.98	0.54	0.54
G-CSF	3.40	1.75	1.48
GDNF	1.35	0.65	0.70
GITR (TNFRSF18)	2.37	2.22	2.38
GITR Ligand (TNFSF18)	2.46	1.71	2.49
GM-CSF	2.05	0.00	1.95
gp130	2.39	1.63	2.63
GRO	2.32	1.41	1.82
GRO alpha (CXCL1)	2.85	1.95	3.37
HCC4 (CCL16)	1.82	1.79	2.43
HGF	1.18	1.22	1.18

ICAM-1 (CD54)	2.30	2.50	4.96
ICAM-3 (CD50)	4.10	3.62	5.65
IFN-gamma	1.15	0.45	1.56
IGF-1	1.31	0.95	0.48
IGF-1R	2.19	1.66	2.88
IGFBP-1	1.12	0.67	2.82
IGFBP-2	1.03	0.85	1.38
IGFBP-3	2.54	2.26	3.77
IGFBP-4	12.72	3.79	6.62
IGFBP-6	2.79	1.94	4.46
IL_1 beta (IL-1 F2)	0.88	0.51	0.57
IL_12 p40	2.06	1.37	3.20
IL-1 alpha (IL-1 F1)	0.60	0.30	0.69
IL-1 ra (IL-1 F3)	1.40	0.95	0.63
IL-10	0.16	0.24	0.36
IL-11	1.90	1.66	3.35
IL-12 p70	2.01	1.88	2.19
IL-13	1.05	0.18	0.46
IL-15	1.64	0.93	0.65
IL-16	1.02	0.68	0.51
IL-17A	1.92	1.50	1.88
IL-1R1	2.48	1.90	3.07
IL-1R4 (ST2)	2.68	2.07	2.61
IL-2	0.93	0.96	1.01
IL-2 R alpha	2.12	1.74	2.44
IL-3	1.30	0.57	0.71
IL-4	1.40	1.18	1.74
IL-5	0.00	0.10	1.65
IL-6	1.78	0.50	1.26
IL-6R	2.26	1.66	1.90
IL-7	9.58	0.00	0.00
IL-8 (CXCL8)	3.85	2.42	2.93
I-TAC (CXCL11)	2.96	2.38	5.95
Leptin	1.28	0.76	0.60
LIGHT (TNSF14)	1.85	1.24	0.63
Lymphotactin	2.18	1.85	6.32
MCP-1 (CCL2)	1.73	1.01	0.30
MCP-2 (CCL8)	0.56	0.51	0.36
MCP-3 (MARC/CCL7)	0.99	0.63	0.68
MCP-4 (CCL13)	0.96	0.54	0.50
M-CSF	1.07	0.69	0.46
MDC (CCL22)	1.20	0.77	0.61
MIF	1.96	3.43	5.03
MIG (CXCL9)	1.13	0.71	0.46
MIP-1 delta (CCL15)	1.48	0.91	0.79
Mip-1-alpha (CCL3)	1.93	2.29	4.42

MIP-1-beta (CCL4)	2.61	2.30	5.17
MIP-3 alpha (CCL20)	2.04	1.34	1.91
MIP-3-beta (CCL19)	2.77	1.94	2.70
MSP (alpha/beta)	2.76	2.40	4.36
NAP-2 (CXCL7)	2.05	1.37	2.42
NT-3	2.38	1.85	4.00
NT-4	2.85	2.37	4.55
OPG (TNFRSF11B)	2.46	1.98	4.23
OSM	3.30	2.52	3.85
PARC (CCL18)	8.71	3.03	16.12
PDGF-BB	1.67	1.04	0.73
PLGF	2.07	1.79	2.47
RANTES (CCL15)	2.15	1.09	0.82
SCF	1.97	0.57	0.42
SDF-1 Alpha	1.30	0.47	0.50
TARC (CCL17)	1.91	0.58	0.58
TECK (CCL25)	2.90	1.68	3.68
TGF Beta 1	1.72	0.89	0.23
TGF Beta 3	1.11	0.58	0.56
TIMP-1	2.69	2.33	3.82
TIMP-2	1.52	1.88	1.70
TNF Alpha	1.34	0.82	0.65
TNF Beta	1.28	0.83	0.70
TNFRI (TNFRSF1A)	2.62	2.12	3.44
TNFRII (TNFRSF1B)	2.32	1.73	2.57
TPO	4.17	2.82	6.75
TRAIL R3	3.22	2.92	5.32
TRAIL R4	0.53	5.54	0.49
uPAR	6.51	5.32	9.55
VEGF-A	5.02	4.06	7.50
VEGF-D	2.36	2.07	3.32

[a]Fold Change Relative to 2D 21%

Table 3.4. Average Ct values for MYCN

	MYCN			*SDHA*		
	SK-N-AS	**KELLY**	**SH-SY5Y**	**SK-N-AS**	**KELLY**	**SH-SY5Y**
2D 21%	33.57	19.11	27.59	23.86	19.11	27.59
2D 1%	31.79	20.40	28.82	24.24	20.40	28.82
3D 21%	32.27	21.18	28.05	25.22	21.18	28.05
3D 1%	30.82	22.64	28.12	25.37	22.64	28.12

3.7. References

[1] J.M. Maris, M.D. Hogarty, R. Bagatell, S.L. Cohn, Neuroblastoma, Lancet 369(9579) (2007) 2106-20.
[2] V. Boeva, C. Louis-Brennetot, A. Peltier, S. Durand, C. Pierre-Eugene, V. Raynal, H.C. Etchevers, S. Thomas, A. Lermine, et al., Heterogeneity of neuroblastoma cell identity defined by transcriptional circuitries, Nat Genet 49(9) (2017) 1408-+.
[3] G.M. Brodeur, A. Nakagawara, Molecular basis of clinical heterogeneity in neuroblastoma, Am J Pediatr Hematol Oncol 14(2) (1992) 111-6.
[4] K.K. Matthay, J.G. Villablanca, R.C. Seeger, D.O. Stram, R.E. Harris, N.K. Ramsay, P. Swift, H. Shimada, C.T. Black, et al., Treatment of high-risk neuroblastoma with intensive chemotherapy, radiotherapy, autologous bone marrow transplantation, and 13-cis-retinoic acid. Children's Cancer Group, N Engl J Med 341(16) (1999) 1165-73.
[5] S.B. Whittle, V. Smith, E. Doherty, S. Zhao, S. McCarty, P.E. Zage, Overview and recent advances in the treatment of neuroblastoma, Expert Rev Anticancer Ther 17(4) (2017) 369-386.
[6] T. Ara, Y.A. DeClerck, Mechanisms of invasion and metastasis in human neuroblastoma, Cancer Metastasis Rev 25(4) (2006) 645-57.
[7] P. Fardin, A. Barla, S. Mosci, L. Rosasco, A. Verri, R. Versteeg, H.N. Caron, J.J. Molenaar, I. Ora, et al., A biology-driven approach identifies the hypoxia gene signature as a predictor of the outcome of neuroblastoma patients, Mol Cancer 9 (2010).
[8] E.B. Rankin, J.M. Nam, A.J. Giaccia, Hypoxia: Signaling the Metastatic Cascade, Trends Cancer 2(6) (2016) 295-304.
[9] J.A. Bertout, S.A. Patel, M.C. Simon, The impact of O2 availability on human cancer, Nat Rev Cancer 8(12) (2008) 967-75.
[10] B. Muz, P. de la Puente, F. Azab, A.K. Azab, The role of hypoxia in cancer progression, angiogenesis, metastasis, and resistance to therapy, Hypoxia (Auckl) 3 (2015) 83-92.
[11] F. Agani, B.H. Jiang, Oxygen-independent regulation of HIF-1: novel involvement of PI3K/AKT/mTOR pathway in cancer, Curr Cancer Drug Targets 13(3) (2013) 245-51.
[12] R. Courtnay, D.C. Ngo, N. Malik, K. Ververis, S.M. Tortorella, T.C. Karagiannis, Cancer metabolism and the Warburg effect: the role of HIF-1 and PI3K, Mol Biol Rep 42(4) (2015) 841-51.
[13] A.C. Koong, E.Y. Chen, A.J. Giaccia, Hypoxia Causes the Activation of Nuclear Factor Kappa-B through the Phosphorylation of I-Kappa-B-Alpha on Tyrosine Residues, Cancer Res 54(6) (1994) 1425-1430.
[14] L. D'Ignazio, M. Batie, S. Rocha, Hypoxia and Inflammation in Cancer, Focus on HIF and NF-kappaB, Biomedicines 5(2) (2017).
[15] E. Minet, T. Arnould, G. Michel, I. Roland, D. Mottet, M. Raes, J. Remacle, C. Michiels, ERK activation upon hypoxia: involvement in HIF-1 activation, Febs Letters 468(1) (2000) 53-58.
[16] A. Zimna, M. Kurpisz, Hypoxia-Inducible Factor-1 in Physiological and Pathophysiological Angiogenesis: Applications and Therapies, Biomed Res Int 2015 (2015) 549412.
[17] C.R. Justus, E.J. Sanderlin, L.V. Yang, Molecular Connections between Cancer Cell Metabolism and the Tumor Microenvironment, Int J Mol Med 16(5) (2015) 11055-11086.
[18] M.R. Horsman, J. Overgaard, The impact of hypoxia and its modification of the outcome of radiotherapy, J Radiat Res 57 Suppl 1 (2016) i90-i98.

[19] G. Jimenez-Valerio, O. Casanovas, Angiogenesis and Metabolism: Entwined for Therapy Resistance, Trends Cancer 3(1) (2017) 10-18.
[20] A. Nyga, U. Cheema, M. Loizidou, 3D tumour models: novel in vitro approaches to cancer studies, J Cell Commun Signal 5(3) (2011) 239-48.
[21] A. Ocana, A. Pandiella, L.L. Siu, I.F. Tannock, Preclinical development of molecular-targeted agents for cancer, Nat Rev Clin Oncol 8(4) (2011) 200-209.
[22] M.E. Katt, A.L. Placone, A.D. Wong, Z.N.S. Xu, P.C. Searson, In Vitro Tumor Models: Advantages, Disadvantages, variables, and Selecting the Right Platform, Front Bioeng Biotech 4 (2016).
[23] M. Kapalczynska, T. Kolenda, W. Przybyla, M. Zajaczkowska, A. Teresiak, V. Filas, M. Ibbs, R. Blizniak, L. Luczewski, et al., 2D and 3D cell cultures - a comparison of different types of cancer cell cultures, Arch Med Sci 14(4) (2018) 910-919.
[24] C. Curtin, J.C. Nolan, R. Conlon, L. Deneweth, C. Gallagher, Y.J. Tan, B.L. Cavanagh, A.Z. Asraf, H. Harvey, et al., A physiologically relevant 3D collagen-based scaffold-neuroblastoma cell system exhibits chemosensitivity similar to orthotopic xenograft models, Acta Biomater 70 (2018) 84-97.
[25] N. Baek, O.W. Seo, M. Kim, J. Hulme, S.S.A. An, Monitoring the effects of doxorubicin on 3D-spheroid tumor cells in real-time, Oncotargets and Therapy 9 (2016) 7207-7218.
[26] J.A. Hickman, R. Graeser, R. de Hoogt, S. Vidic, C. Brito, M. Gutekunst, H. van der Kuip, I.P. Consortium, Three-dimensional models of cancer for pharmacology and cancer cell biology: capturing tumor complexity in vitro/ex vivo, Biotechnol J 9(9) (2014) 1115-28.
[27] J.B. Kim, Three-dimensional tissue culture models in cancer biology, Semin Cancer Biol 15(5) (2005) 365-377.
[28] K. Stock, M.F. Estrada, S. Vidic, K. Gjerde, A. Rudisch, V.E. Santo, M. Barbier, S. Blom, S.C. Arundkar, et al., Capturing tumor complexity in vitro: Comparative analysis of 2D and 3D tumor models for drug discovery, Sci Rep-Uk 6 (2016) 28951.
[29] D. Wu, P. Yotnda, Induction and testing of hypoxia in cell culture, J Vis Exp (54) (2011).
[30] F.J. O'Brien, Biomaterials & scaffolds for tissue engineering, Materials Today 14(3) (2011) 88-95.
[31] S.J. Hollister, Porous scaffold design for tissue engineering, Nat Mater 4(7) (2005) 518-24.
[32] D.W. Hutmacher, Scaffold design and fabrication technologies for engineering tissues--state of the art and future perspectives, J Biomater Sci Polym Ed 12(1) (2001) 107-24.
[33] Y.K. Girard, C. Wang, S. Ravi, M.C. Howell, J. Mallela, M. Alibrahim, R. Green, G. Hellermann, S.S. Mohapatra, et al., A 3D fibrous scaffold inducing tumoroids: a platform for anticancer drug development, PLoS One 8(10) (2013) e75345.
[34] S. Moscato, F. Ronca, D. Campani, S. Danti, Poly(vinyl alcohol)/gelatin Hydrogels Cultured with HepG2 Cells as a 3D Model of Hepatocellular Carcinoma: A Morphological Study, J Funct Biomater 6(1) (2015) 16-32.
[35] A. Voissiere, E. Jouberton, E. Maubert, F. Degoul, C. Peyrode, J.M. Chezal, E. Miot-Noirault, Development and characterization of a human three-dimensional chondrosarcoma culture for in vitro drug testing, PLoS One 12(7) (2017) e0181340.
[36] C.W. Yeung, K. Cheah, D. Chan, B.P. Chan, Effects of Reconstituted Collagen Matrix on Fates of Mouse Embryonic Stem Cells Before and After Induction for Chondrogenic Differentiation, Tissue Eng Pt A 15(10) (2009) 3071-3085.

[37] P. Yeung, H.S. Sin, S. Chan, G.C.F. Chan, B.P. Chan, Microencapsulation of Neuroblastoma Cells and Mesenchymal Stromal Cells in Collagen Microspheres: A 3D Model for Cancer Cell Niche Study, Plos One 10(12) (2015).

[38] G.N. Li, L.L. Livi, C.M. Gourd, E.S. Deweerd, D. Hoffman-Kim, Genomic and morphological changes of neuroblastoma cells in response to three-dimensional matrices, Tissue Eng 13(5) (2007) 1035-47.

[39] G. Xu, F. Yin, H. Wu, X. Hu, L. Zheng, J. Zhao, In vitro ovarian cancer model based on three-dimensional agarose hydrogel, J Tissue Eng 5 (2014) 2041731413520438.

[40] D.N. Rockwood, R.C. Preda, T. Yucel, X. Wang, M.L. Lovett, D.L. Kaplan, Materials fabrication from Bombyx mori silk fibroin, Nat Protoc 6(10) (2011) 1612-31.

[41] J. Rnjak-Kovacina, L.S. Wray, K.A. Burke, T. Torregrosa, J.M. Golinski, W. Huang, D.L. Kaplan, Lyophilized Silk Sponges: A Versatile Biomaterial Platform for Soft Tissue Engineering, Acs Biomater Sci Eng 1(4) (2015) 260-270.

[42] J.J. Morton, G. Bird, Y. Refaeli, A. Jimeno, Humanized Mouse Xenograft Models: Narrowing the Tumor-Microenvironment Gap, Cancer Res 76(21) (2016) 6153-6158.

[43] C. Correia, S. Bhumiratana, L.P. Yan, A.L. Oliveira, J.M. Gimble, D. Rockwood, D.L. Kaplan, R.A. Sousa, R.L. Reis, et al., Development of silk-based scaffolds for tissue engineering of bone from human adipose-derived stem cells, Acta Biomater 8(7) (2012) 2483-92.

[44] B. Panilaitis, G.H. Altman, J.S. Chen, H.J. Jin, V. Karageorgiou, D.L. Kaplan, Macrophage responses to silk, Biomaterials 24(18) (2003) 3079-3085.

[45] L.S. Wray, J. Rnjak-Kovacina, B.B. Mandal, D.F. Schmidt, E.S. Gil, D.L. Kaplan, A silk-based scaffold platform with tunable architecture for engineering critically-sized tissue constructs, Biomaterials 33(36) (2012) 9214-24.

[46] N. Minoura, S. Aiba, Y. Gotoh, M. Tsukada, Y. Imai, Attachment and Growth of Cultured Fibroblast Cells on Silk Protein Matrices, J Biomed Mater Res 29(10) (1995) 1215-1221.

[47] N. Minoura, S.I. Aiba, M. Higuchi, Y. Gotoh, M. Tsukada, Y. Imai, Attachment and Growth of Fibroblast Cells on Silk Fibroin, Biochem Biophys Res Co 208(2) (1995) 511-516.

[48] E. Dondajewska, W. Juzwa, A. Mackiewicz, H. Dams-Kozlowska, Heterotypic breast cancer model based on a silk fibroin scaffold to study the tumor microenvironment, Oncotarget 9(4) (2018) 4935-4950.

[49] A. Backer, O. Erhardt, L. Wietbrock, N. Schel, B. Goppert, M. Dirschka, P. Abaffy, T. Sollich, A. Cecilia, et al., Silk scaffolds connected with different naturally occurring biomaterials for prostate cancer cell cultivation in 3D, Biopolymers 107(2) (2017) 70-79.

[50] B. Subia, T. Dey, S. Sharma, S.C. Kundu, Target specific delivery of anticancer drug in silk fibroin based 3D distribution model of bone-breast cancer cells, ACS Appl Mater Interfaces 7(4) (2015) 2269-79.

[51] S. Raghavan, P. Mehta, E.N. Horst, M.R. Ward, K.R. Rowley, G. Mehta, Comparative analysis of tumor spheroid generation techniques for differential in vitro drug toxicity, Oncotarget 7(13) (2016) 16948-61.

[52] P. Buchwald, FEM-based oxygen consumption and cell viability models for avascular pancreatic islets, Theor Biol Med Model 6 (2009) 5.

[53] R.H. Swerdlow, E. Lezi, D. Aires, J.H. Lu, Glycolysis-respiration relationships in a neuroblastoma cell line, Bba-Gen Subjects 1830(4) (2013) 2891-2898.

[54] J.J. Casciari, S.V. Sotirchos, R.M. Sutherland, Mathematical modelling of microenvironment and growth in EMT6/Ro multicellular tumour spheroids, Cell Prolif 25(1) (1992) 1-22.

[55] P. Han, D.M. Bartels, Temperature dependence of oxygen diffusion in H2O and D2O, J Phys Chem-Us 100(13) (1996) 5597-5602.

[56] T. Opriessnig, P.F. Gerber, C.T. Xiao, P.G. Halbur, S.R. Matzinger, X.J. Meng, Commercial PCV2a-based vaccines are effective in protecting naturally PCV2b-infected finisher pigs against experimental challenge with a 2012 mutant PCV2, Vaccine 32(34) (2014) 4342-8.

[57] W.J. Maskill, N. Crofts, E. Waldman, D.S. Healey, T.S. Howard, C. Silvester, I.D. Gust, An evaluation of competitive and second generation ELISA screening tests for antibody to HIV, J Virol Methods 22(1) (1988) 61-73.

[58] A. Jogi, I. Ora, H. Nilsson, A. Lindeheim, Y. Makino, L. Poellinger, H. Axelson, S. Pahlman, Hypoxia alters gene expression in human neuroblastoma cells toward an immature and neural crest-like phenotype, Proc Natl Acad Sci U S A 99(10) (2002) 7021-6.

[59] M.A. Varia, D.P. Calkins-Adams, L.H. Rinker, A.S. Kennedy, D.B. Novotny, W.C. Fowler, Jr., J.A. Raleigh, Pimonidazole: a novel hypoxia marker for complementary study of tumor hypoxia and cell proliferation in cervical carcinoma, Gynecol Oncol 71(2) (1998) 270-7.

[60] A.S. Truong, M.R. Lockett, Oxygen as a chemoattractant: confirming cellular hypoxia in paper-based invasion assays, Analyst 141(12) (2016) 3874-82.

[61] S. Agarwal, A. Lakoma, Z. Chen, J. Hicks, L.S. Metelitsa, E.S. Kim, J.M. Shohet, G-CSF Promotes Neuroblastoma Tumorigenicity and Metastasis via STAT3-Dependent Cancer Stem Cell Activation, Cancer Res 75(12) (2015) 2566-79.

[62] D.M. Hsu, S. Agarwal, A. Benham, C. Coarfa, D.N. Trahan, Z. Chen, P.N. Stowers, A.N. Courtney, A. Lakoma, et al., G-CSF receptor positive neuroblastoma subpopulations are enriched in chemotherapy-resistant or relapsed tumors and are highly tumorigenic, Cancer Res 73(13) (2013) 4134-46.

[63] E.S. Kim, S. Agarwal, J.M. Shohet, G-CSF Is a Cancer Stem Cell-Specific Growth Factor-Response, Cancer Res 75(18) (2015) 3992.

[64] H. Russell, J.M. Shohet, Pediatric oncology: G-CSF counteracts chemotherapy toxicity in neuroblastoma, Nat Rev Clin Oncol 8(1) (2011) 6-8.

[65] S.J. Xiong, Y.J. Wang, H.J. Li, X.F. Zhang, Low Dose of Bisphenol A Activates NF-kappa B/IL-6 Signals to Increase Malignancy of Neuroblastoma Cells, Cell Mol Neurobiol 37(6) (2017) 1095-1103.

[66] T. Ara, R. Nakata, M.A. Sheard, H. Shimada, R. Buettner, S.G. Groshen, L.Y. Ji, H. Yu, R. Jove, et al., Critical Role of STAT3 in IL-6-Mediated Drug Resistance in Human Neuroblastoma, Cancer Res 73(13) (2013) 3852-3864.

[67] L. Zhang, H. Yeger, B. Das, M.S. Irwin, S. Baruchel, Tissue microenvironment modulates CXCR4 expression and tumor metastasis in neuroblastoma, Neoplasia 9(1) (2007) 36-46.

[68] S.J. Coniglio, Role of Tumor-Derived Chemokines in Osteolytic Bone Metastasis, Front Endocrinol (Lausanne) 9 (2018) 313.

[69] H.M. Ameis, A. Drenckhan, M. Freytag, J.R. Izbicki, C.T. Supuran, K. Reinshagen, S. Holland-Cunz, S.J. Gros, Influence of hypoxia-dependent factors on the progression of neuroblastoma, Pediatr Surg Int 32(2) (2016) 187-92.

[70] S. Daster, N. Amatruda, D. Calabrese, R. Ivanek, E. Turrini, R.A. Droeser, P. Zajac, C. Fimognari, G.C. Spagnoli, et al., Induction of hypoxia and necrosis in multicellular tumor spheroids is associated with resistance to chemotherapy treatment, Oncotarget 8(1) (2017) 1725-1736.

[71] S. Ambrosio, S. Amente, C.D. Sacca, M. Capasso, R.A. Calogero, L. Lania, B. Majello, LSD1 mediates MYCN control of epithelial-mesenchymal transition through silencing of metastatic suppressor NDRG1 gene, Oncotarget 8(3) (2017) 3854-3869.
[72] N. Braekeveldt, C. Wigerup, D. Gisselsson, S. Mohlin, M. Merselius, S. Beckman, T. Jonson, A. Borjesson, T. Backman, et al., Neuroblastoma patient-derived orthotopic xenografts retain metastatic patterns and geno- and phenotypes of patient tumours, Int J Cancer 136(5) (2015) E252-E261.
[73] A.J. Cheng, N.C. Cheng, J. Ford, J. Smith, J.E. Murray, C. Flemming, M. Lastowska, M.S. Jackson, C.S. Hackett, et al., Cell lines from MYCN transgenic murine turnours reflect the molecular and biological characteristics of human neuroblastorna, Eur J Cancer 43(9) (2007) 1467-1475.
[74] L. Chesler, D.D. Goldenberg, I.T. Seales, R. Satchi-Fainaro, M. Grimmer, R. Collins, C. Struett, K.N. Nguyen, G. Kim, et al., Malignant progression and blockade of angiogenesis in a murine transgenic model of neuroblastoma, Cancer Res 67(19) (2007) 9435-9442.
[75] W.A. Weiss, K. Aldape, G. Mohapatra, B.G. Feuerstein, J.M. Bishop, Targeted expression of MYCN causes neuroblastoma in transgenic mice, Embo J 16(11) (1997) 2985-2995.
[76] H.R. Kumar, X. Zhong, D.J. Hoelz, F.J. Rescorla, R.J. Hickey, L.H. Malkas, J.A. Sandoval, Three-dimensional neuroblastoma cell culture: proteomic analysis between monolayer and multicellular tumor spheroids, Pediatr Surg Int 24(11) (2008) 1229-34.
[77] J.R. Park, A. Eggert, H. Caron, Neuroblastoma: biology, prognosis, and treatment, Hematol Oncol Clin North Am 24(1) (2010) 65-86.
[78] S.R. McKeown, Defining normoxia, physoxia and hypoxia in tumours-implications for treatment response, Br J Radiol 87(1035) (2014) 20130676.
[79] M.E. Hubbi, G.L. Semenza, Regulation of cell proliferation by hypoxia-inducible factors, Am J Physiol-Cell Ph 309(12) (2015) C775-C782.
[80] K.L. Eales, K.E.R. Hollinshead, D.A. Tennant, Hypoxia and metabolic adaptation of cancer cells, Oncogenesis 5 (2016).
[81] D. Faratian, A. Munro, C. Twelves, J.M.S. Bartlett, Membranous and cytoplasmic staining of Ki67 is associated with HER2 and ER status in invasive breast carcinoma, Histopathology 54(2) (2009) 254-257.
[82] L. Chierico, L. Rizzello, L. Guan, A.S. Joseph, A. Lewis, G. Battaglia, The role of the two splice variants and extranuclear pathway on Ki-67 regulation in non-cancer and cancer cells, PLoS One 12(2) (2017) e0171815.
[83] Y.J. Kim, S.H. Lee, J. Lee, H.J. Kuh, Non-nuclear localization of Ki-67 in human colorectal cancer cells grown as multicellular layers, Arch Pharm Res 36(5) (2013) 634-640.
[84] J. Chiche, K. Ilc, J. Laferriere, E. Trottier, F. Dayan, N.M. Mazure, M.C. Brahimi-Horn, J. Pouyssegur, Hypoxia-inducible carbonic anhydrase IX and XII promote tumor cell growth by counteracting acidosis through the regulation of the intracellular pH, Cancer Res 69(1) (2009) 358-68.
[85] P. Ramani, A. Headford, M.T. May, GLUT1 protein expression correlates with unfavourable histologic category and high risk in patients with neuroblastic tumours, Virchows Arch 462(2) (2013) 203-9.
[86] E.G. Skoldenberg, A. Larsson, A. Jakobson, F. Hedborg, P. Kogner, R.H. Christofferson, F. Azarbayjani, The angiogenic growth factors HGF and VEGF in serum and plasma from neuroblastoma patients, Anticancer Res 29(8) (2009) 3311-9.

[87] M. Fakhari, D. Pullirsch, K. Paya, D. Abraham, R. Hofbauer, S. Aharinejad, Upregulation of vascular endothelial growth factor receptors is associated with advanced neuroblastoma, J Pediatr Surg 37(4) (2002) 582-7.

[88] M. Vyas, N. Patel, R. Celli, N. Wajapeyee, D. Jain, X. Zhang, Glucose Metabolic Reprogramming and Cell Proliferation Arrest in Colorectal Micropapillary Carcinoma, Gastroenterology Res 12(3) (2019) 128-134.

[89] W. Sun, Z.Y. Shen, H. Zhang, Y.Z. Fan, W.Z. Zhang, J.T. Zhang, X.S. Lu, C. Ye, Overexpression of HIF-1 alpha in primary gallbladder carcinoma and its relation to vasculogenic mimicry and unfavourable prognosis, Oncol Rep 27(6) (2012) 1990-2002.

[90] J. Pelletier, G. Bellot, P. Gounon, S. Lacas-Gervais, J. Pouyssegur, N.M. Mazure, Glycogen Synthesis is Induced in Hypoxia by the Hypoxia-Inducible Factor and Promotes Cancer Cell Survival, Front Oncol 2 (2012) 18.

[91] S. Riffle, R.S. Hegde, Modeling tumor cell adaptations to hypoxia in multicellular tumor spheroids, J Exp Clin Cancer Res 36(1) (2017) 102.

[92] S. Riffle, R.N. Pandey, M. Albert, R.S. Hegde, Linking hypoxia, DNA damage and proliferation in multicellular tumor spheroids, Bmc Cancer 17(1) (2017) 338.

[93] T. Monkkonen, J. Debnath, Inflammatory signaling cascades and autophagy in cancer, Autophagy 14(2) (2018) 190-198.

[94] P. Nallasamy, S. Chava, S.S. Verma, S. Mishra, S. Gorantla, D.W. Coulter, S.N. Byrareddy, S.K. Batra, S.C. Gupta, et al., PD-L1, inflammation, non-coding RNAs, and neuroblastoma: Immuno-oncology perspective, Semin Cancer Biol 52(Pt 2) (2018) 53-65.

[95] L.G. Griffith, M.A. Swartz, Capturing complex 3D tissue physiology in vitro, Nat Rev Mol Cell Biol 7(3) (2006) 211-24.

[96] X. Xu, M.C. Farach-Carson, X. Jia, Three-dimensional in vitro tumor models for cancer research and drug evaluation, Biotechnol Adv 32(7) (2014) 1256-1268.

[97] F.A. Ferrer, A.G. Pantschenko, L.J. Miller, K. Anderson, M. Grunnet, P.H. McKenna, D. Kreutzer, Angiogenesis and neuroblastomas: interleukin-8 and interleukin-8 receptor expression in human neuroblastoma, J Urol 164(3 Pt 2) (2000) 1016-20.

[98] I.S. Hong, Stimulatory versus suppressive effects of GM-CSF on tumor progression in multiple cancer types, Exp Mol Med 48(7) (2016) e242.

[99] D.R. Barreda, P.C. Hanington, M. Belosevic, Regulation of myeloid development and function by colony stimulating factors, Dev Comp Immunol 28(5) (2004) 509-54.

[100] J.K. Thomas, H. Mir, N. Kapur, S. Bae, S. Singh, CC chemokines are differentially expressed in Breast Cancer and are associated with disparity in overall survival, Sci Rep-Uk 9 (2019).

[101] Y. Liu, Y. Cai, L. Liu, Y. Wu, X. Xiong, Crucial biological functions of CCL7 in cancer, PeerJ 6 (2018) e4928.

[102] E. Farmaki, V. Kaza, A.G. Papavassiliou, I. Chatzistamou, H. Kiaris, Induction of the MCP chemokine cluster cascade in the periphery by cancer cell-derived Ccl3, Cancer Lett 389 (2017) 49-58.

[103] N. Reynders, D. Abboud, A. Baragli, M.Z. Noman, B. Rogister, S.P. Niclou, N. Heveker, B. Janji, J. Hanson, et al., The Distinct Roles of CXCR3 Variants and Their Ligands in the Tumor Microenvironment, Cells 8(6) (2019).

[104] T.J. Pugh, O. Morozova, E.F. Attiyeh, S. Asgharzadeh, J.S. Wei, D. Auclair, S.L. Carter, K. Cibulskis, M. Hanna, et al., The genetic landscape of high-risk neuroblastoma, Nat Genet 45(3) (2013) 279-84.

[105] J.L. Harenza, M.A. Diamond, R.N. Adams, M.M. Song, H.L. Davidson, L.S. Hart, M.H. Dent, P. Fortina, C.P. Reynolds, et al., Transcriptomic profiling of 39 commonly-used neuroblastoma cell lines (vol 4, 170033, 2017), Sci Data 4 (2017).

[106] O.I. Hoffmann, C. Ilmberger, S. Magosch, M. Joka, K.W. Jauch, B. Mayer, Impact of the spheroid model complexity on drug response, J Biotechnol 205 (2015) 14-23.

[107] T. Teitz, J.J. Stanke, S. Federico, C.L. Bradley, R. Brennan, J.K. Zhang, M.D. Johnson, J. Sedlacik, M. Inoue, et al., Preclinical Models for Neuroblastoma: Establishing a Baseline for Treatment, Plos One 6(4) (2011).

[108] C.S. Branda, S.M. Dymecki, Talking about a revolution: The impact of site-specific recombinases on genetic analyses in mice, Dev Cell 6(1) (2004) 7-28.

Chapter 4: Development of a stacked neuroblastoma model

4.1. Introduction

Many solid tumors demonstrate regions of reduced oxygen tension, otherwise known as hypoxia [1-5]. In tumors, rapid proliferation and high levels of oxygen consumption yield to depleted levels of oxygen, particularly in cells far from vasculature [6]. Rapid growth in tumors without adequate vasculature leads to gradients of oxygen, nutrients, and pH [7]. Cancer cells that are under hypoxic stress have an altered metabolic pathway, relying instead on glycolysis [1, 2, 8]. Hypoxic stress has also been demonstrated to cause adaptations in tumor cells that promote a more aggressive tumor phenotype [9, 10]. These changes include promotion of migration, invasion, resistance to apoptosis, and increased angiogenesis [3, 4, 11-13].

As neuroblastoma is an orphan disease there are few preclinical *in vitro* models available for disease modeling. Current NB hypoxia models have relied on chemical induction of hypoxia using DMOG (HIF-1 activator) or $CoCl_2$ (mimics HIF-1 activation) or use of low oxygen incubators [14]. In NB cell lines, use of low oxygen incubators and DMOG has been shown to confer important pathway changes, which persisted when cells were implanted *in vivo* [15]. However, low oxygen incubators and DMOG are primarily useful at identifying cellular changes at the molecular level. In tumors is hypoxia is cell-driven, existing in a gradient with the highest oxygen tension close to vasculature and lowest oxygen tension distant from vasculature. Further, cells under hypoxia can impact surrounding tumor cells, having an impact on the tumor's responsiveness to therapeutics and metastatic potential.

Many current 3D *in vitro* models are capable of generating hypoxic regions. The commonly used spheroid models (cell aggregates) demonstrates a hypoxic core once the tumor has reached a size of greater than 200 µm [16-18]. Spheroids have been used to study therapeutic response to hypoxia as well as alterations in pathway expression [17, 19]. However, it is difficult to spatially control spheroids, and analysis of different regions of the spheroid is a challenge. Hydrogel systems have also been used to model hypoxia. For example, cells have been grown within hydrogels composed of collagen, agarose, and Matrigel [20-22]. Scaffold based approaches have also been used. These include polymer (natural and synthetic), paper (cellulose), and silk fibroin [23-26]. Scaffolds are advantageous as they allow for spatial control of cell distribution. This allows for control of where cells are located in the model, which is especially important when multiple cell types are incorporated. In comparison scaffold free approaches such as spheroids can be non-uniformly distributed and analysis of different areas of the model can be difficult.

In the previous aim, we demonstrated the use of silk scaffolds and low oxygen incubators to model different levels of oxygen tension of the tumor microenvironment. Further, we demonstrated changes in gene expression and cytokine secretion due to 3D culture and low oxygen. In the present study, we generated 3D models using stacked silk fibroin scaffolds. Silk fibroin has been demonstrated to be an effective material for tissue engineering due to its stability, biocompatibility, and lack of immunogenic response [27-30]. While many studies have been performed to engineer 3D tumor models (both using scaffolds and in spheroid form), few studies have developed systems with controlled oxygen gradients. To achieve this, we utilized a stacking method, which has been previously employed to evaluate cell invasion and for layered cell models [25, 31, 32]. COMSOL modeling was used to determine the impact of scaffold holder geometry on oxygen diffusion and number of scaffolds on oxygen gradients (as a result of oxygen consumption). Stacks of different thicknesses were evaluated for cell presence through dsDNA content and histology. Hypoxic gradients were characterized through gene expression and pimonidazole staining as compared to single scaffolds grown in ambient and low oxygen. This system has the potential to be applied to many different cancer types and to allow for improved understanding of tumor pathways as well as presenting a novel therapeutic testing platform.

4.2. Materials and Methods

4.2.1. Cell culturing

KELLY NB cells (Millipore Sigma, St. Louis, MO) were maintained in Roswell Park Memorial Institute 1640 (RPMI) medium supplemented with 10% v/v fetal bovine serum, 100 U/mL penicillin, 100 µg/mL streptomycin, and 2 mM L-glutamine (Fisher Scientific, Hampton, NH) at 37°C at 5% CO_2 in a humidified environment. SK-N-AS NB cells (ATCC, Manassas, VA) were maintained in Dulbecco's Modified Eagle Media (DMEM) supplemented with 10% v/v fetal bovine serum, 100 U/mL penicillin, 100 µg/mL streptomycin, 2mM L-glutamine, and 0.1 mM NEAA (Fisher Scientific, Hampton, NH) at 37°C at 5% CO_2 in a humidified environment. All cells were passaged using 0.25% trypsin-EDTA at 70-80% confluence. For low oxygen cultures a 37°C, 5% CO_2, 1% O_2 incubator was used.

4.2.2. Silk fibroin extraction

Silk fibroin from *Bombyx mori* silkworm cocoons (Tajima Shoji Co Yokohama, Japan), kindly provided by Dr. David L. Kaplan at Tufts University, was extracted as previously described [29]. Briefly, 5 g cocoons were cut into approximately 1 cm x 1 cm pieces and boiled for 30 min in 0.02 M Na_2CO_3 to extract the sericin. Silk fibers were then dried overnight. The dried silk fibroin fibers were dissolved in 9.3 M LiBr at 60°C for 3 h. The dissolved silk fibroin was dialyzed in 3,500 MWCO dialysis tubing (Fisher Scientific, Hampton, NH) against ultrapure water for 2 d with a minimum of 6 water changes. The aqueous silk fibroin (referred to as silk from here on) solution was stored at 4°C for future use.

4.2.3. Silk scaffold fabrication

Silk scaffolds were using 2 mL of 5% silk solution in 15.6 mm cylindrical molds. Lyophilization was performed using rate-control freezing with a 2 h hold at -45°C followed by lyophilization for 30 h at -25°C. Secondary drying was performed with a 2 h hold at -4°C, followed by ramping up to 20°C. All steps before lyophilization were performed at a rate of 0.5°C/min, all steps following engagement of the vacuum were performed at 1°C/min. To render the materials insoluble, scaffolds were autoclaved following removal from the lyophilizer. Once the materials were rendered insoluble, scaffolds were vibratome sectioned to a thickness of 200 µm and biopsy punched with a 6 mm diameter biopsy punch. Scaffolds were sterilized via autoclaving in ultrapure water.

4.2.4. Seeding of cells on scaffolds

Cells grown, as described above, were made into a single cell suspension. Cells were seeded at a concentration of 100,000 cells/µL. Seeding was performed by applying a volume of 5 µL of to the scaffold, waiting 10 minutes, vertically inverting the scaffold and applying the remaining 5 µL. The cell-seeded scaffolds were allowed to incubate at 37°C, 5% CO_2 for 4 h before moving to 3 mL of medium.

4.2.5. Stacking of scaffolds

Cell seeded scaffolds were allowed to grow at 21% O_2 for 3 d. After 3 d, the scaffolds were stacked using a PTFE (Polytetrafluoroethylene) scaffold holder into stacks of two, four, six, or eight scaffolds in 8 mL of medium. As a control, single scaffolds were maintained in 3 mL of medium at both 21% and 1% oxygen. Stacks were grown for 3 d on a rotating shaker at a speed of 75 rpm.

4.2.6. DNA content analysis

Scaffolds were lysed with 0.5% Triton X-100 in Tris-EDTA buffer for 20 min at room temperature. All samples were passed through a freeze-thaw cycle (-20°C) prior to analysis. DNA content was analyzed using a Quant-iT™ PicoGreen™ dsDNA Assay Kit (Fisher Scientific, Hampton, NH) according to the manufacturer's protocol. The full protocol can be found in **Appendix X**. After thaw, the samples were centrifuged and diluted 1:5 with TE buffer. The samples were incubated at room temperature for 5 min in a 200-fold dilution of the PicoGreen™ dye. The DNA concentration was determined by measuring the fluorescence at an excitation wavelength of 480 nm and an emission wavelength of 520 nm (Victor Multilabel Plate Reader, Perkin Elmer, Waltham, MA) and comparing to a standard curve of lambda DNA (0 µg/mL to 2 µg/mL).

4.2.7. Histology

Cell seeded scaffolds or stacks of scaffolds were frozen in OCT and cryosectioned to a thickness of 20 µm. Sections were fixed in 100% methanol at 4°C for 5 minutes, followed by 25% methanol for 5 minutes. Sections were then hydrated in PBS for 10 minutes. Following hydration, sections were stained with Harris hematoxylin and eosin following standard procedures (**Appendix V**).

4.2.8. Pimonidazole staining

Prior to the termination of culture, scaffolds of stacks were treated with 300 µM pimonidazole (Hypoxyprobe, Burlington, MA) for 24 h, as previously described [25]. Scaffolds or stacks were fixed in 10% formalin, frozen in OCT, and cryosectioned to a thickness of 20 µm.

Sections were hydrated in PBS for 10 minutes, then blocked and permeabilized in 5% NGS with 0.1% Triton X-100 for 1 h. Pimonidazole secondary was applied at a dilution of 1:50 in PBS overnight at 4°C. Sections were counter stained with Hoechst (1:5000) to visualize cell nuclei. Scaffolds that were not treated with pimonidazole were used as negative controls (**Appendix IV**).

4.2.1. Brightfield imaging

Brightfield imaging of histology was performed in bright field an upright microscope (Nikon Eclipse E600, Tokyo, Japan) with a digital camera (Spot Insight CMOS 5.1, Sterling Heights, MI).

4.2.2. Fluorescent imaging

Fluorescent imaging was performed used an Axiovert 200M Zeiss inverted epi-fluor microscope (Oberkochen, Germany). Exposure time was determined based on negative controls (highest possible exposure where negative control failed to exhibit positive staining) for pimonidazole.

4.2.3. Gene expression

Stacks were separated based on distance from the medium source with the scaffolds on the exterior being combined, then the next layer being combined, until the two center most scaffolds were combined. Total RNA was isolated from scaffolds or stacks after 3 d of culture using a TRIzol reagent according to the manufacturer's instructions. RNA was dissolved in ultrapure molecular grade water and measured using an absorbance of 260 nm using a spectrophotometer (Nanodrop 2000, Thermo Scientific). cDNA was synthesized using High-Capacity cDNA Reverse Transcription Kit (Applied Biosystems, Foster City, CA). qRT-PCR was performed on a 7500 Real Time PCR System (Applied Biosystems, Foster City, CA) using SYBR Green qPCR master mix (Applied Biosystems, Foster City, CA). SDHA was used as an internal control as has been previously demonstrated in NB [10, 33-35]. The relative expression was quantified using the ΔΔ cycle threshold method. Data was normalized to the 2D 21% condition. **Table 4.1** lists the primer sequences used in this study.

Table 4.1. List of primers used for qRT-PCR in Aim 2.

Gene	Sequence
CAIX	F - GGGTGTCATCTGGACTGTGTT R - CTTCTGTGCTGCCTTCTCATC
GLUT1	F - CCTGCAGTTTGGCTACAACA R - GTGGACCCATGTCTGGTTG
IGFBP3	F – TCTGCGTCAACGCTAGTGC R - GCTCTGAGACTCGTAGTCAACT
VEGF	F - AGGAGGAGGGCAGAATCATCA R - CTCGATTGGATGGCAGTAGCT
SDHA (housekeeper)	F - TGGGAACAAGAGGGCATCTG R - CCACCACTGCATCAAATTCATG

4.2.4. Mathematical modeling of oxygen concentrations

Mathematical modeling was utilized to determine oxygen gradients within the scaffolds. Simulated oxygen diffusion and consumption was performed on a commercially available finite element platform (COMSOL, Burlington, MA). 3D axisymmetric modeling was utilized based on scaffolds grown in the holder. For preliminary modeling (original scaffold holder), an assumed oxygen concentration of 21% at interface of the holder well with media reservoir was used. For design of the final scaffold holder, an oxygen concentration of 21% at the interface of the PTFE piece touching the scaffold and media reservoir was assumed (based on mixing). These models were run through a "transport of diluted species" module incorporating both diffusion and consumption rates (modeled using Michaelis Menten kinetics) available from literature [36-40]. The following values were utilized in our model:

Oxygen diffusion coefficient, $D = 2.6 \times 10^{-9}\ m^2\ s^{-1}$

oxygen consumption rate, $OCR = -3.09 \times 10^{-4}\ mol\ m^{-3}s^{-1}$

Michaelis-Menten coefficient, $MM = 0.0046\ mol\ m^{-3}$

Initial concentration of oxygen at the surface of the culture $C = 0.21\ mol\ m^{-3}$

The model utilizes the following equations:

Rate of Oxygen Consumption, $R = -\frac{OCR*C}{MM+C}$

Transport of diluted species: $\frac{dc_i}{dt} + \nabla \cdot (-D_i \nabla c_i) = R_i$

Uniform oxygen consumption was assumed within the scaffold. It was also assumed that the scaffold did not limit oxygen diffusion. Culture medium as well as the scaffolds were modeled as water.

4.2.5. Statistical analysis

Data is presented as mean ± SEM for all gene expression data. Data is presented as mean ± SD for all other data. All data is presented as the mean of three biological replicates, except for the 200 µm vs. 600 µm study which is presented as the mean of three experimental replicates. Statistical significance was determined by one-way ANOVA followed by Tukey honestly significant differences test in GraphPad Prism (version 5.0; San Diego, CA). For comparison of only two groups statistics were determined using an unpaired t-test. Statistics for qRT-PCR were run using the delta CT (gene of interest-housekeeping gene) for each condition. Significance was determined at $P < 0.05$.

4.3. Results

4.3.1. Impact of scaffold thickness on cell proliferation and infiltration

First, we sought to understand the impact of scaffold thickness on cell growth and infiltration. Scaffolds (200 µm and 600 µm in thickness) were seeded with SK-N-AS and KELLY NB cells and were evaluated for cell proliferation based on dsDNA content (Picogreen) and metabolic activity (Resazurin) (**Figure 4.1, Figure 4.2**). Both 200 µm and 600 µm scaffolds supported cell proliferation as indicated by the increase in DNA content and metabolic activity. Specifically, both exhibited an initial drop in dsDNA from d 1 to d3 (**Figure 4.1 A**). Following this, dsDNA increased from 2.5 µg/scaffold (d 1) to a maximum dsDNA content of 4.7 µg/scaffold (d 10) for 200 µm and from 4.0 µg/scaffold (d 1) to a maximum dsDNA content of 4.5 µg/scaffold (d 10) for 600 µm. Similar results were observed with metabolic activity in KELLY and SK-N-AS cells with maximum increases of 1.69 fold (SK-N-AS, 200 µm, d 1 to d 14), 1.4 fold (SK-N-AS, 600 µm, d 1 to d 14), 2.4 fold (KELLY, 200 µm, d 1 to d 28), and 1.9 fold (KELLY, 600 µm, d 1 to d 28) (**Figure 4.2 A, B**). No differences in viability and DNA content were seen between 200 µm and 600 µm scaffolds after the initial 3 d of growth. As cells were seeded proportionally (1 million cells on 200 µm and 3 million cells on 600 µm scaffolds), this suggests that cells were less able to grow on thicker scaffolds. Examination of cell infiltration through H&E staining demonstrated presence of cells in the periphery of the scaffold in both 200 µm and 600 µm scaffolds (**Figure 4.1 B,C**). Over time, cells fully infiltrated the 200 µm scaffolds, creating an evenly distributed high number of cells within the scaffold. In comparison, the 600 µm scaffolds demonstrated limited cell distribution throughout the scaffold, even over time, with a confluent layer of cells on the outer surface, but limited cells in the center of the scaffold. The same response was observed with KELLY NB cells (**Figure 4.2 C, D**)This suggests that the interior of the scaffold was not conducive to cell growth, likely due to diffusion limitations for oxygen and nutrients. Based on these observations, subsequent experiments were performed with 200 µm scaffolds.

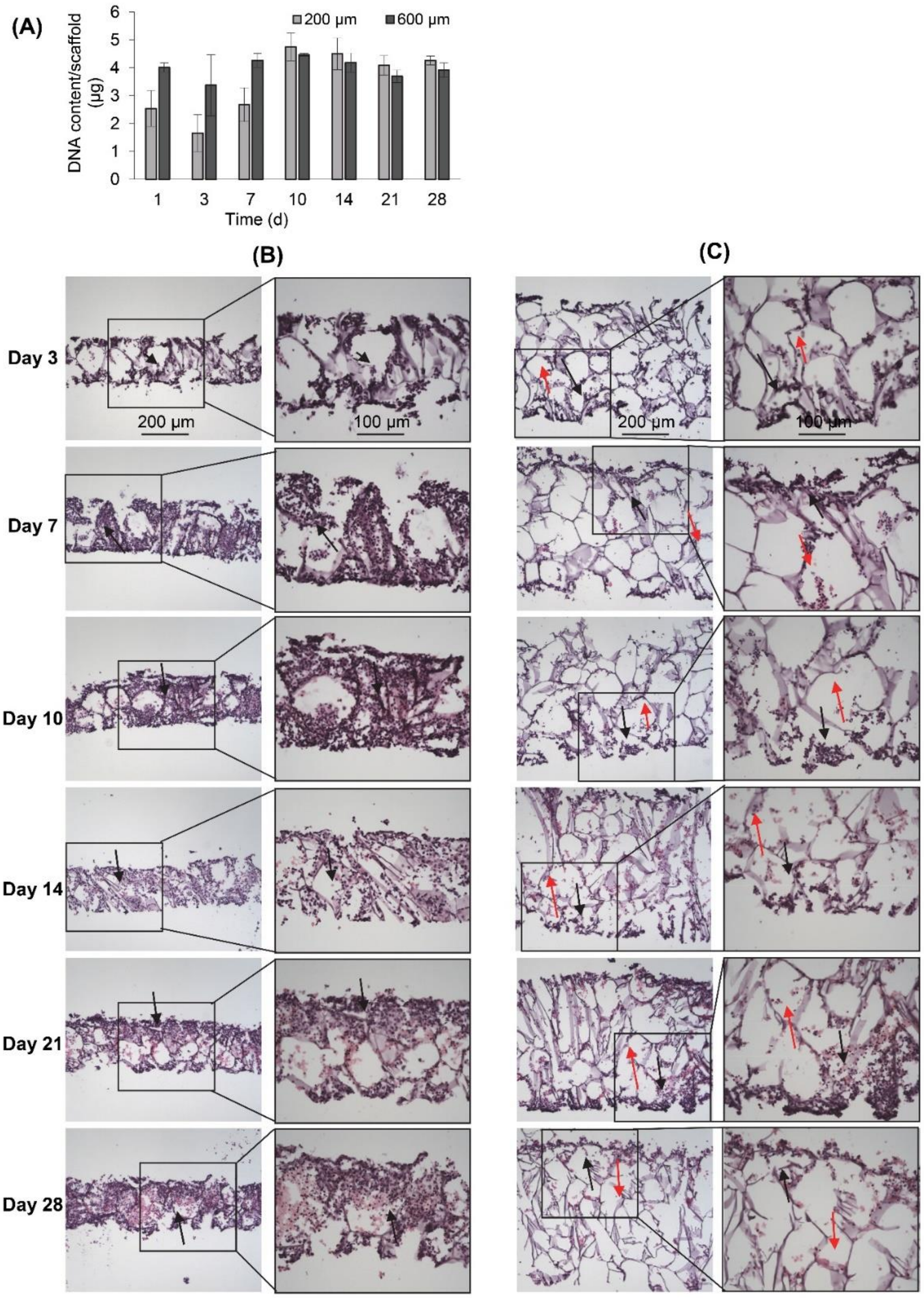

Figure 4.1. Impact of scaffold thickness on cell growth (DNA content) and distribution .
(A) Impact of scaffold thickness on SK-N-AS growth over time as determined by dsDNA content. Data is presented as mean ± SD of three individual samples. Hematoxylin and eosin staining to visualize SK-N-AS NB cell distribution throughout scaffolds over time in (B) 200 µm scaffolds and (C) 600 µm scaffolds. Black arrows indicate areas of high cell density, red arrows indicate areas of low cell density.

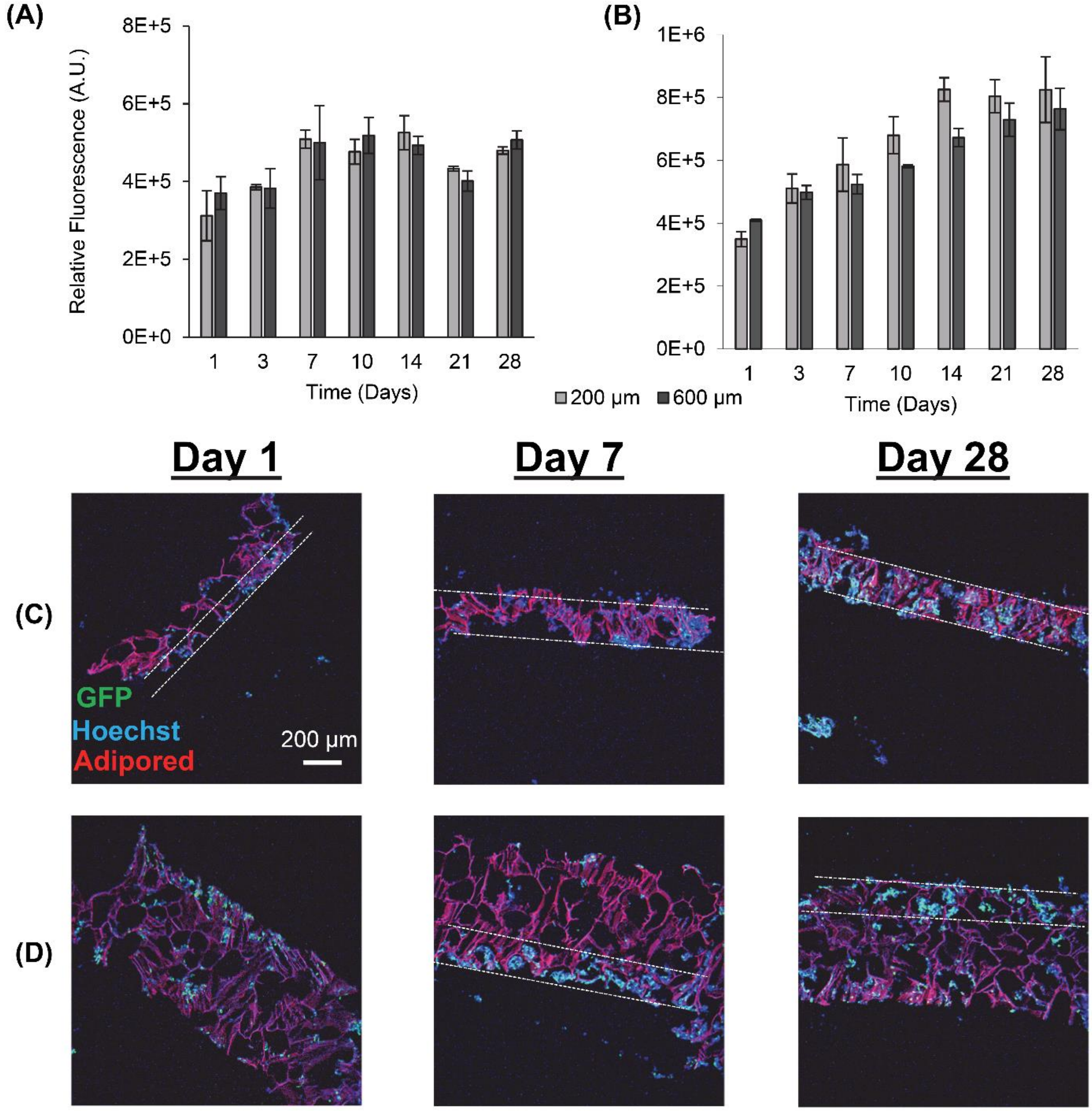

Figure 4.2. Impact of scaffold thickness on cell growth (metabolic) and distribution. Impact of scaffold thickness on (A) SK-N-AS and (B) KELLY NB grown over time (metabolic via Resazurin). Data is presented as mean ± SD of three individual samples. Fluorescent staining to visualize KELLY cell distribution over time in (C) 200 µm scaffolds and (D) 600 µm scaffolds.

4.3.2. Development of stacked culture system

To facilitate the stacking of 200 µm scaffolds, a holder was designed and fabricated out of PTFE. The first iteration of scaffold holders was designed to hold stacks of scaffolds between a solid piece of PTFE and a piece of PTFE with a hole for media to pass through (**Figure 4.3 A**). This would create a hypoxic gradient from the interface of the media to the solid PTFE bottom. However, analysis of stacks grown in this scaffold holder (gene expression and COMSOL modeling) demonstrated that the deep and narrow channel between the scaffold and the media reservoir cause the scaffolds to be in a hypoxic state (**Figure 4.3 B**). Analysis of gene expression of three stacked scaffolds grown in this system demonstrated no differences in *VEGF*, *CAIX*, or *GLUT1* (**Figure 4.3 C**). This is due to the metabolic nature of NB cells out competing the oxygen diffusion rate. Based on these preliminary results, we identified a key parameter of the scaffold holder, the depth of the channel between the media reservoir and the surface of the scaffolds, to evaluate further for optimizing oxygen tension at the scaffold surface.

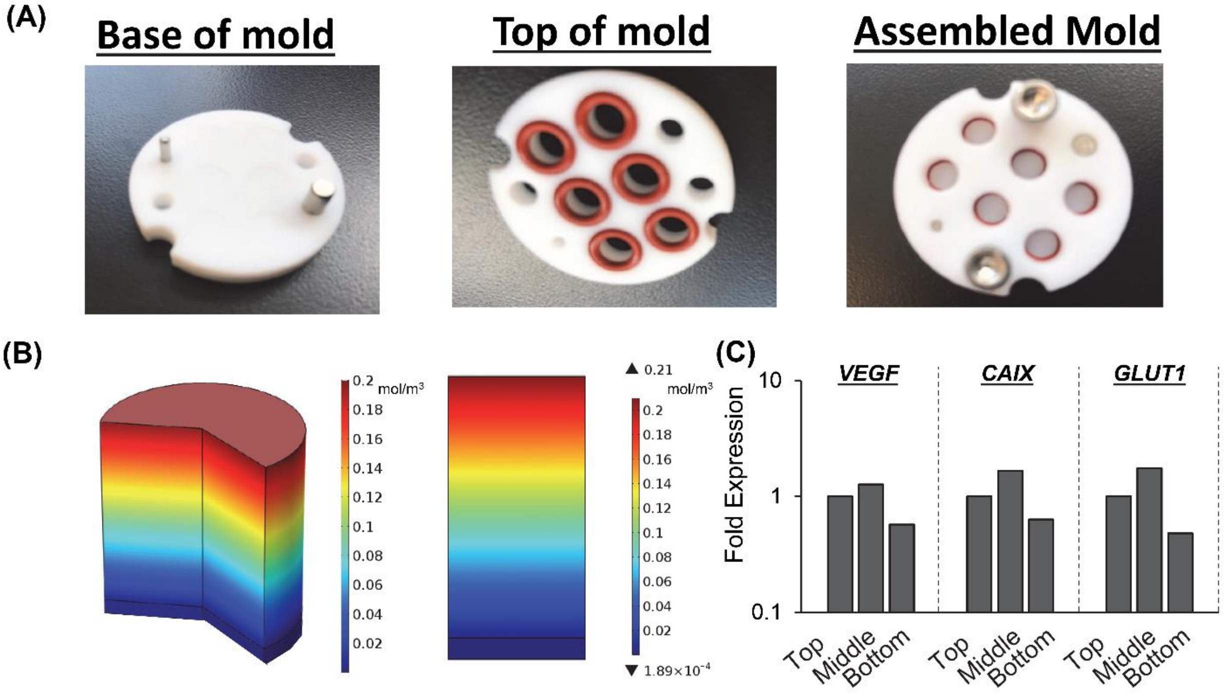

Figure 4.3. Original scaffold holder design and its impact on oxygen diffusion.
(A) Original scaffold holder design consisting of two PTFE plates with O-rings to hold scaffolds in place. (B) COMSOL modeling of the original scaffold holder with a single scaffold at the bottom of the well. (C) Hypoxia related gene expression for a stack of 3 scaffolds seeded with SK-N-AS cells within the original holder. Data is presented as mean of a single representative experiment.

COMSOL modeling was performed to identify the channel depth able to allow oxygen to diffuse at a fast enough rate to the scaffold (**Figure 4.4 A-D**). Channel depths of 5 mm, 2.5 mm, 1 mm, and 0.5 mm were modeled. Scaffold holders of 5 mm and 2.5 mm demonstrated hypoxic conditions within a single scaffold, suggesting that oxygen diffusion was too slow to the scaffold. Thicknesses 1 mm and 0.5 mm suggested scaffolds within the normal oxygen range for tissue, indicating enough oxygen was able to diffuse to overcome the high metabolic rate of the cells. This was further confirmed by calculating oxygen diffusion times using the equation: $t \approx \frac{x^2}{2D}$, with D= 2.6×10^{-9} m^2 s^{-1}.

The oxygen diffusion time through the modeled depths were 80 min, 20 min, 3 min and 1 min for 5 mm, 2.5 mm, 1 mm, and 0.5 mm, respectively. For subsequent work, 500 µm was selected for the channel depth as it allowed for the most oxygen to reach the scaffold (based on diffusion rate) and was on the lower end of the range that the PTFE could be machined.

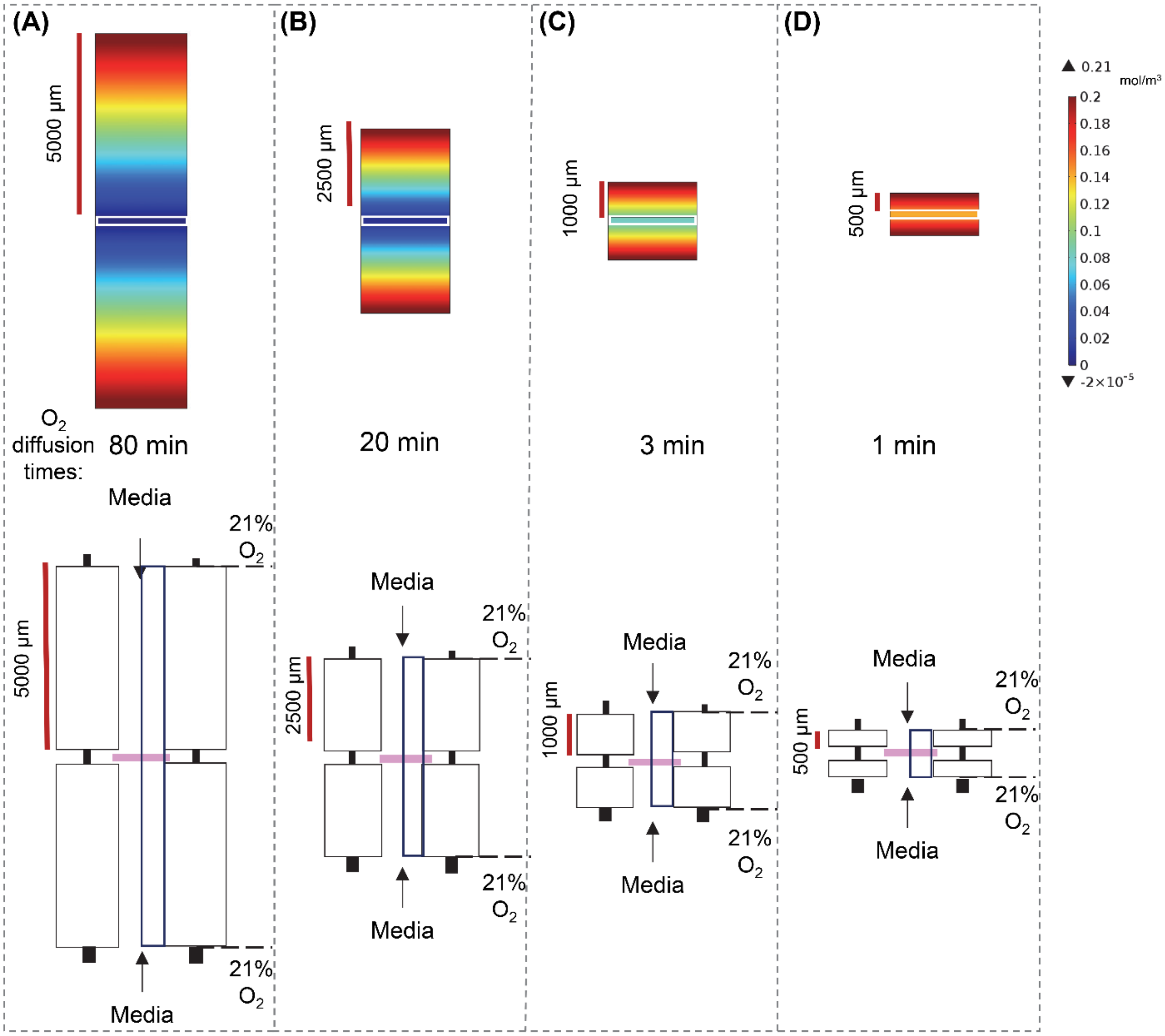

Figure 4.4. COMSOL modeling and oxygen diffusion times of scaffold holders with a single scaffold and varying channel depths.
COMSOL modeling of a scaffold holder with a depth of (A) 5,000 µm (5 mm), (B) 2,500 µm (2.5 mm), (C) 1,000 µm (1 mm), and (D) 500 µm (0.5 mm). Based on a single scaffold within the holder.

Scaffold holders were designed to be expandable (for stacks of different thicknesses) and fit within a standard 6-well plate (**Figure 4.5**). COMSOL modeling of scaffold holders demonstrated the potential for a range of oxygen gradients through a cell-laden scaffold **(Figure 4.6**). This modeling assumed an oxygen concentration of 21% at the edge of the PTFE piece in contact with the scaffold, due to the use of a shaker to enhance oxygen diffusion. Models of stacks with two scaffolds demonstrated an oxygen concentration of approximately 6-8% within the scaffold (**Figure 4.6 A**). Increased scaffold number in the stacks demonstrated lower concentrations of oxygen within the center of the stack. Modeling of four, six and eight scaffolds demonstrated a range of oxygen concentrations from 4-6% (exterior) to <2% (interior) (**Figure 4.6 B-D**). These oxygen levels are similar to those of physiological tumors, which have been shown to range from <0.7% to 4-5% [1, 41, 42].

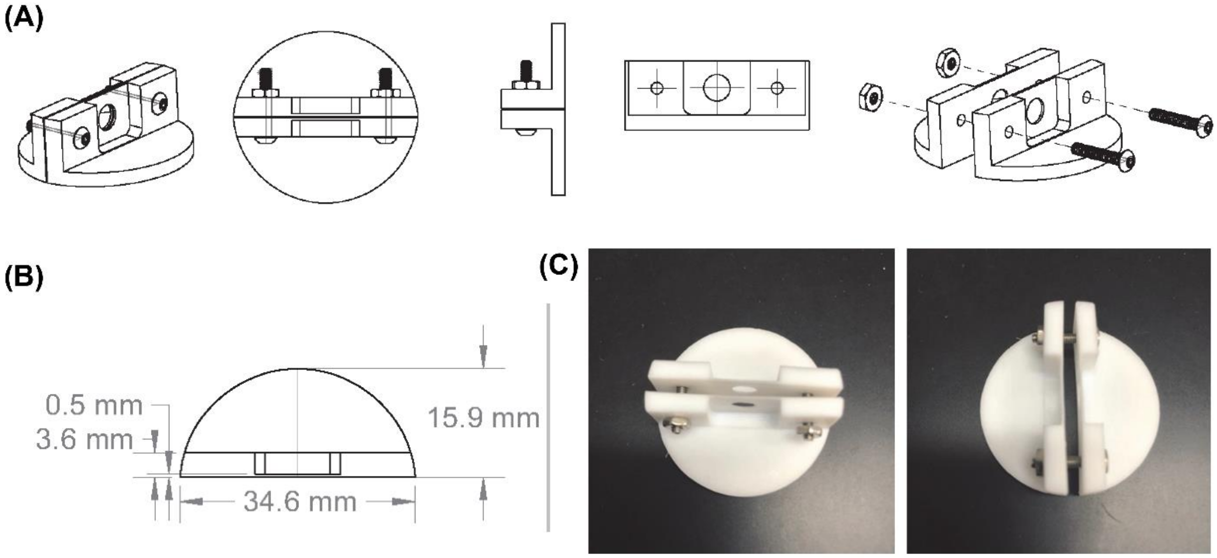

Figure 4.5. Final design of scaffold holder.

(4) CAD images of the final scaffold holder. (B) CAD drawing with dimensions of the final scaffold holder design. (C) Images of the fabricated PTFE scaffold holder.

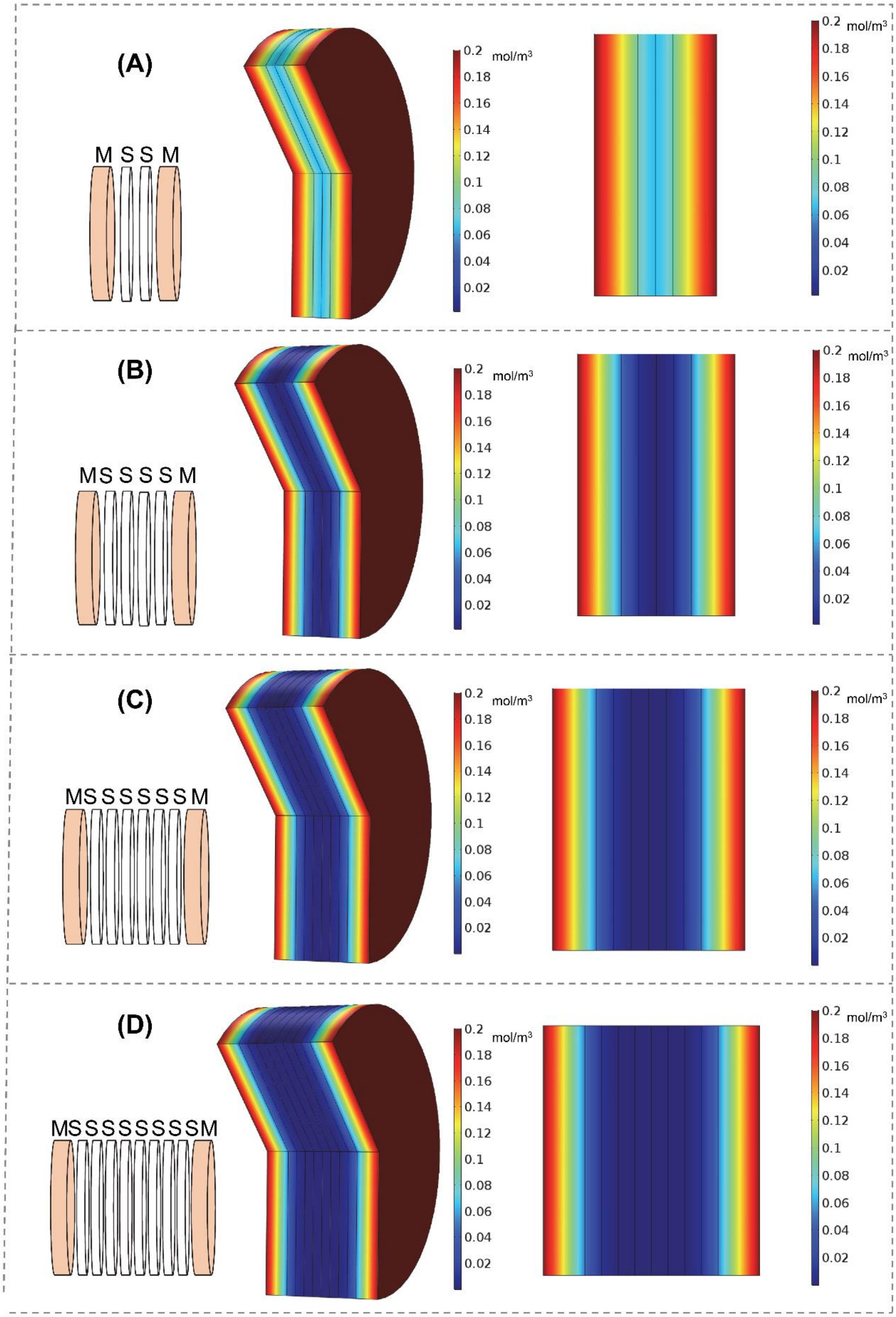

Figure 4.6. COMSOL modeling of different stack thicknesses.
COMSOL modeling of stacks of (A) two scaffolds (B) four scaffolds (B) six scaffolds and (D) eight scaffolds utilizing parameters from the final scaffold holder design.

4.3.3. Histology of stacked scaffolds

Utilizing the stacking system, we first sought to observe the impact of stacking scaffolds on cell distribution within the stacks. Scaffolds were grown in stacks of two, four, six, and eight scaffolds for 3 d on a shaker at ambient oxygen and compared to non-stacked scaffolds at ambient and low oxygen. Hematoxylin and eosin staining of stacks demonstrated that individual scaffolds as well as stacks of two scaffolds had cells present throughout the scaffold (**Figure 4.7 A-C**). In stacks of four scaffolds, cells were present throughout, although more cells were observed on the exterior as compared to the interior (**Figure 4.7 D**). Similar results were observed in the stacks of six and eight scaffolds where cells were distributed throughout with a higher concentration on the exterior (**Figure 4.7 E-F**).

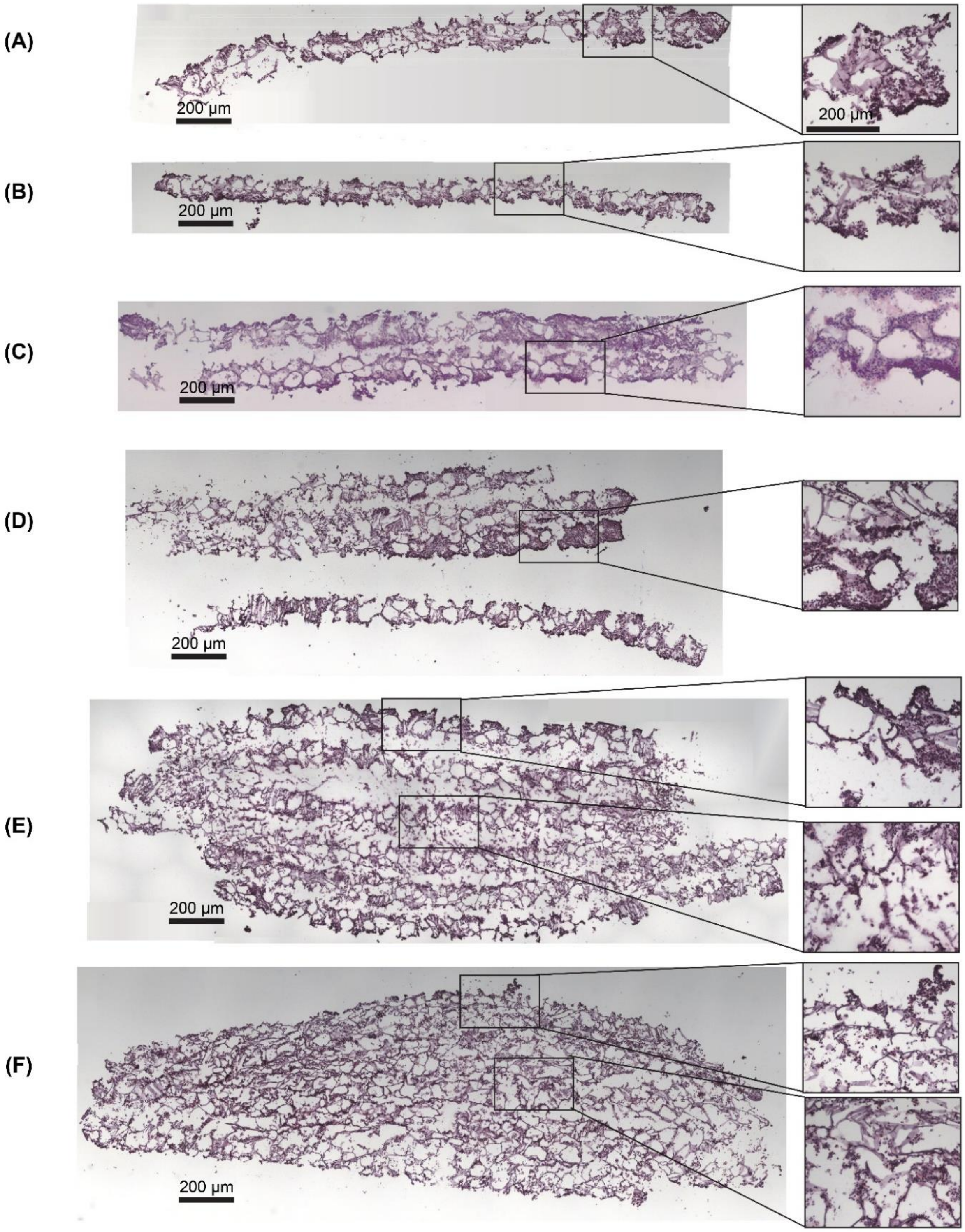

Figure 4.7. Visualization of cell distribution in stacked scaffolds.
Hematoxylin and eosin staining to visualize SK-N-AS NB cell distribution within stacks 3 d post stacking as compared to single scaffolds at ambient (A) and low (B) oxygen 3 d post stacking. Stack thicknesses of (C) two, (D) four, (E) six, and (F) eight (scaffolds) were examined.

4.3.4. Evaluation of scaffold DNA content

Next we sought to determine the impact of stacking on dsDNA content at each layer (**Figure 4.8**). Analysis of DNA content in ambient oxygen scaffolded conditions as compared to scaffolded conditions in low oxygen demonstrated a significant decrease in dsDNA from 3.2 µg/scaffold to 1.4 µg/scaffold (**Figure 4.8**). Analysis of a double stack of scaffolds demonstrated similar DNA content to scaffolds grown in ambient oxygen (3.7 µg/scaffold vs. 3.2 µg/scaffold) (**Figure 4.8**). In quadruple stacked scaffolds the interior of the stack resembled the single low oxygen scaffold in DNA content (1.2 µg/scaffold vs. 1.4 µg/scaffold, stacked and low oxygen respectively), while the exterior of the stack resembled the single ambient oxygen scaffold (3.3 µg/scaffold vs. 3.2 µg/scaffold, stacked and ambient oxygen respectively) (**Figure 4.8**). A similar trend was observed in sextuple stacked scaffolds where dsDNA content decreased from 2.8 µg/scaffold in the exterior vs. 2.2 µg/scaffold in the middle layer vs. 1.5 µg/scaffold in the interior (**Figure 4.8**). No significant differences were present between the single scaffolds grown in ambient oxygen and the exterior or middle of the stack. Similarly, no significant differences were present between single scaffolds at low oxygen and the middle or interior of the scaffold. Evaluation of dsDNA in the octuple stacked scaffolds demonstrated a lowered change in DNA content as compared to smaller stacks. The DNA content ranged from 3.3 µg/scaffold at the exterior to 2.0 µg/scaffold at the interior (**Figure 4.8**). No significant differences were present between any of the layers of the stack. This suggests that eight scaffolds may not be demonstrating a gradient of microenvironment.

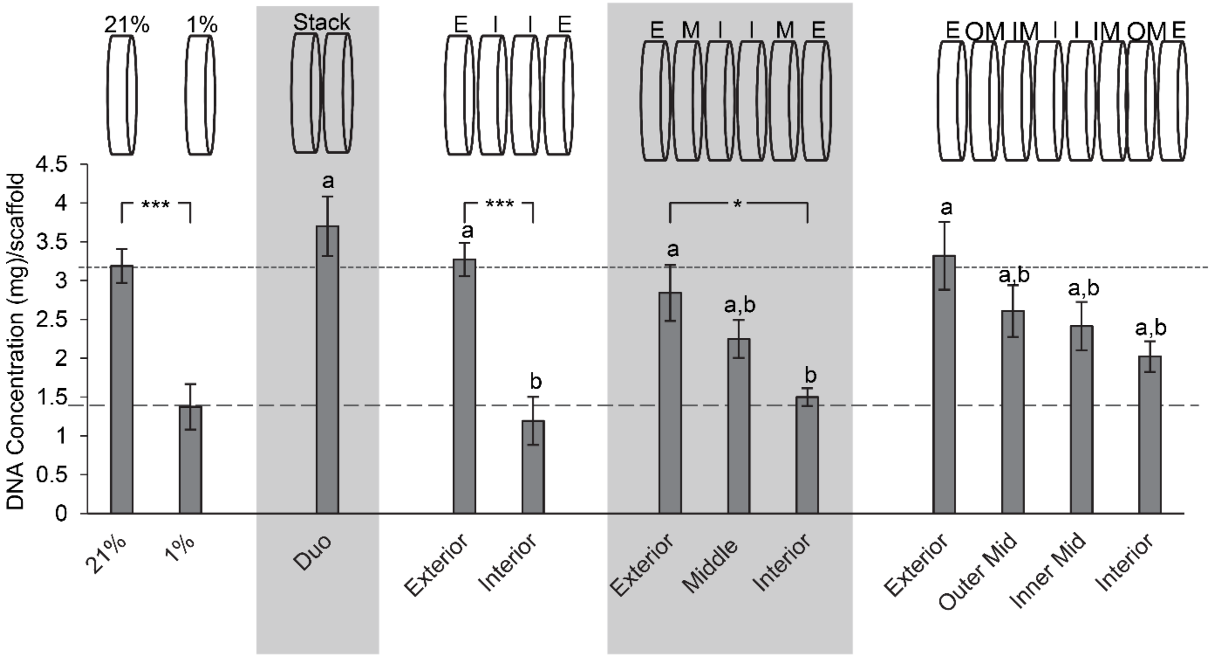

Figure 4.8. Impact of stacking on dsDNA content of scaffold layers.
Evaluation of dsDNA content of SK-N-AS NB stacked scaffolds at each individual layer 3 d post stacking. 21% (ambient) and 1% (low) represent single scaffolds grown at that oxygen concentration. Representation of each stacking thickness can be found above it on the graph. "E" corresponds to exterior, "I" corresponds to interior, "M" corresponds to the middle, "OM" corresponds to the outer middle, and "IM" corresponds to the inner middle. Data is presented as mean ± SD of three independent experiments. A denotes no statistical significance from single scaffolds grown at ambient oxygen, b denotes no statistical significance from single scaffolds grown at low oxygen. Asterisk indicate statistical significance between the groups (*** $p<0.001$, ** $p<0.01$, **$p<0.05$).

4.3.5. Evaluation of hypoxic gene expression in stacked culture

After determining differences in DNA content similar to that of single scaffolds cultured in low and ambient oxygen, we next sought to characterize the microenvironment of the stacks through gene expression. SK-N-AS NB scaffolds were grown for 3 d at ambient oxygen then moved to stacked culture, kept at 21% (ambient) O_2, or moved to 1% (low) O_2 for an additional 3 d. Gene expression of hypoxia-linked genes *VEGF*, *CAIX*, *GLUT1*, and *IGFBP3* was evaluated (**Figure 4.9**). All gene expression was compared to cells grown in monolayer culture at ambient oxygen. Scaffolds grown in ambient oxygen and low oxygen demonstrated increased expression of all markers as compared to monolayer ambient oxygen culture (**Figure 4.9)**. As compared to scaffolded ambient oxygen culture, scaffolded low oxygen cultures demonstrated significantly higher expression in all genes except for *IGFBP3*, which demonstrated a trend towards increasing expression. Stacks of different thickness were compared to scaffolds grown at ambient and low oxygen. Evaluation of double stacked scaffolds grown in the scaffold holder demonstrated similar expression of *VEGF* (11.1 vs. 9.3 fold expression, *CAIX* (883.0 vs. 1133.2 fold expression, *GLUT1* (8.1 vs. 8.0 fold expression), and *IGFBP3* (9.1 vs. 4.7 fold expression) to the scaffolded ambient oxygen condition (**Figure 4.9**). No significant differences were observed between the double stacked scaffolds and scaffolded ambient oxygen condition (**Figure 4.9**). Quadruple stacked scaffolds demonstrated a gradient of hypoxic gene expression (**Figure 4.9**). The interior of the stack demonstrated increased expression of hypoxic markers as compared to the exterior with changes in *VEGF* (22.4 vs. 14.1 fold expression), *CAIX* (1960.4 vs. 1066.5 fold expression), *GLUT1* (16.9 vs. 12.42 fold expression), and *IGFBP3* (37.8 vs. 7.9 fold expression). All of these gene expression changes were significant except for *VEGF* (**Figure 4.9**). Comparison of the interior of the stack with scaffolded low oxygen culture demonstrated no significant differences. Similarly, comparison of the exterior of the stack with scaffolded ambient oxygen culture was only significantly different in *IGFBP3*. This suggests the presence of an oxygen gradient where the exterior of the stacks resembled scaffolded ambient oxygen culture and the interior of the stacks resembled scaffolded low oxygen culture.

Analysis of sextuple stacked scaffolds also suggests the presence of hypoxic gradients in which the middle and interior of the stack demonstrated higher expression of hypoxic genes than the exterior (**Figure 4.9**). No significant differences in *VEGF* were observed among scaffolds within the stack, however, the middle and the interior of the stack demonstrated significant increases as compared to scaffolded ambient oxygen culture (12.4, 19.4, 18.7 fold expression for exterior, middle, and interior) (**Figure 4.9)**. *CAIX* expression was significantly increase in the middle and interior of the stack as compared to the exterior of the scaffold (915.1, 1957.5, 1328.5 fold expression for exterior, middle, and interior) (**Figure 4.9**). Similarly, *GLUT1* expression was significantly increase in the middle and interior of the stack as compared to the exterior of the scaffold (7.4, 14.7, 17.3 fold expression for exterior, middle, and interior) (**Figure 4.9)**. *IGFBP3* did not exhibit any significant increase in expression, however the middle and interior exhibited increased expression as compared to the exterior (12.6, 26.1, 22.7 fold expression for exterior, middle, and interior) (**Figure 4.9**).

Octuple stacked scaffolds demonstrated an interesting trend with an increase from the exterior scaffold to the adjacent (outer middle) layer, followed by a decrease in the two most interior layers (**Figure 4.9**). This trend was present in *VEGF*, *CAIX*, *GLUT1*, and *IGFBP3* expression. Significant increases between the exterior of the scaffold and the adjacent layer were present in VEGF and *GLUT1* expression (**Figure 4.9**). No significant differences were observed between the exterior and interior of the scaffold. This suggests that eight scaffolds may be ineffective for generating hypoxic gradients (**Figure 4.9**).

MMP9 expression was also evaluated in stacks (**Figure 4.10**). Previous results from Aim 1 demonstrated that MMP9 is mainly driven by 3D culture. However, a trend was still observed where scaffolds on the interior of the stacks more closely resembled low oxygen scaffolded growth and scaffolds on the exterior of the stacks more closely resembled ambient oxygen scaffolded growth for double, quadruple, and sextuple stacks.

Gene expression of quadruple stacked scaffolds was also evaluated using KELLY NB cells (**Figure 4.11**). Scaffolded culture in low oxygen and the interior of the stack demonstrated a significant increase in expression as compared to scaffolded culture in ambient oxygen. While no significant differences were observed between the interior and exterior of the stack, the interior demonstrated an increased expression of hypoxia markers *VEGF*, *CAIX*, *GLUT1*, and *IGFBP3* (**Figure 4.11**). *VEGF* and *IGFBP3* expression were highest in the interior of the stacks. *CAIX* expression was significantly increased in the interior of the stack as compared to scaffolded culture in ambient oxygen and followed the same trend for the exterior of the stack (as compared to scaffolded ambient oxygen) (**Figure 4.11**). Expression of *GLUT1* also followed the trend where scaffolded ambient oxygen culture was more similar to the exterior of the stack, and scaffolded low oxygen culture was more similar to the interior of the stack, although no significant differences were observed (**Figure 4.11**).

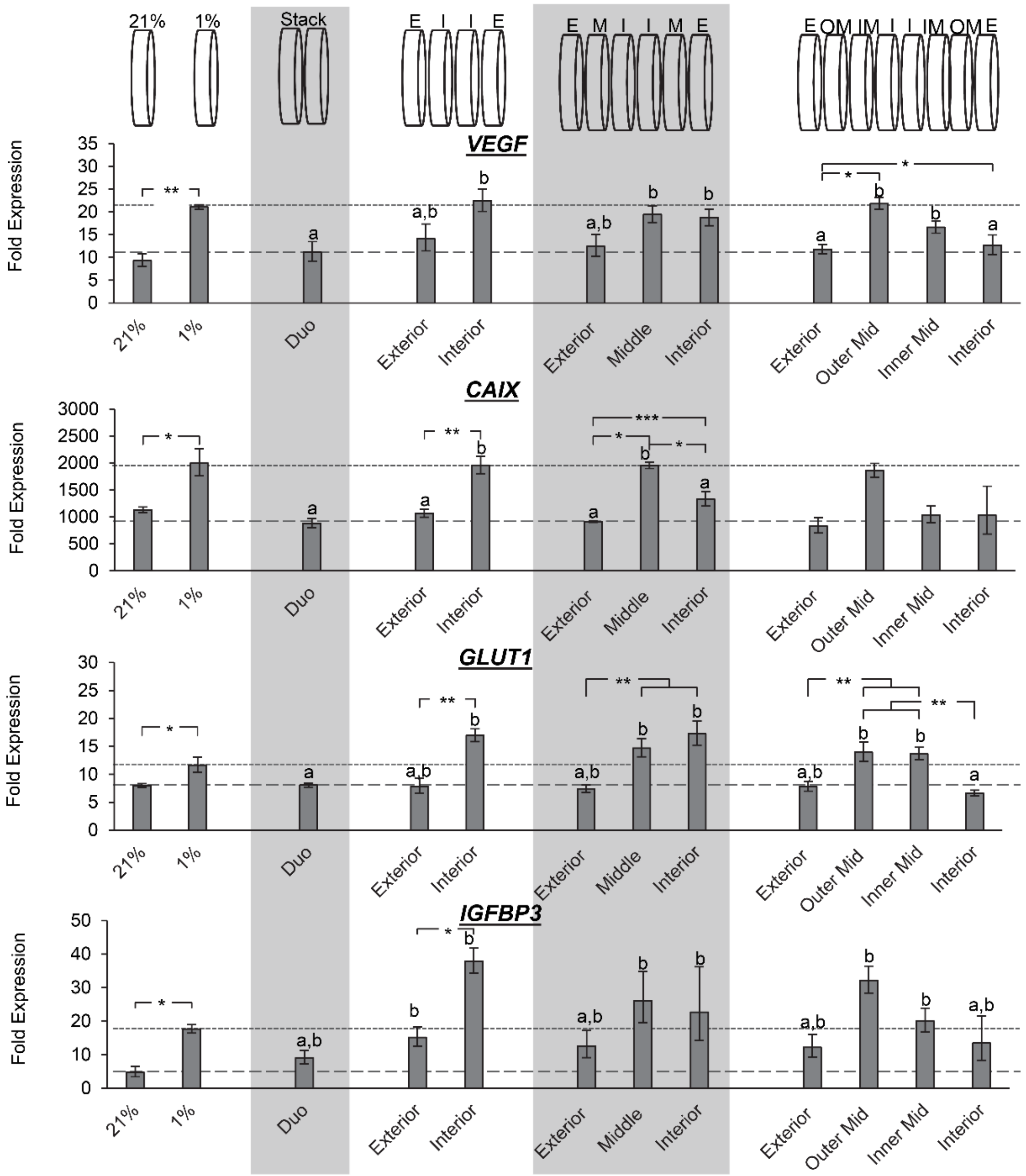

Figure 4.9. Evaluation of hypoxia related gene expression in stacked scaffolds.
Evaluation of hypoxia related gene expression of SK-N-AS NB stacked scaffolds at each individual layer as compared to monolayer ambient oxygen culture 3 d post stacking. 21% (ambient) and 1% (low) represent single scaffolds grown at that oxygen concentration. Representation of each stacking thickness can be found above it on the graph. “E” corresponds to exterior, “I” corresponds to interior, “M” corresponds to the middle, “OM” corresponds to the outer middle, and “IM” corresponds to the inner middle. Data is presented as mean ± SD of three independent experiments. a denotes no statistical significance from single scaffolds grown at ambient oxygen, b denotes no statistical significance from single scaffolds grown at low oxygen. All gene expression is normalized to a monolayer, ambient oxygen control. Asterisk indicate statistical significance between the groups (*** $p<0.001$, ** $p<0.01$, ** $p<0.05$).

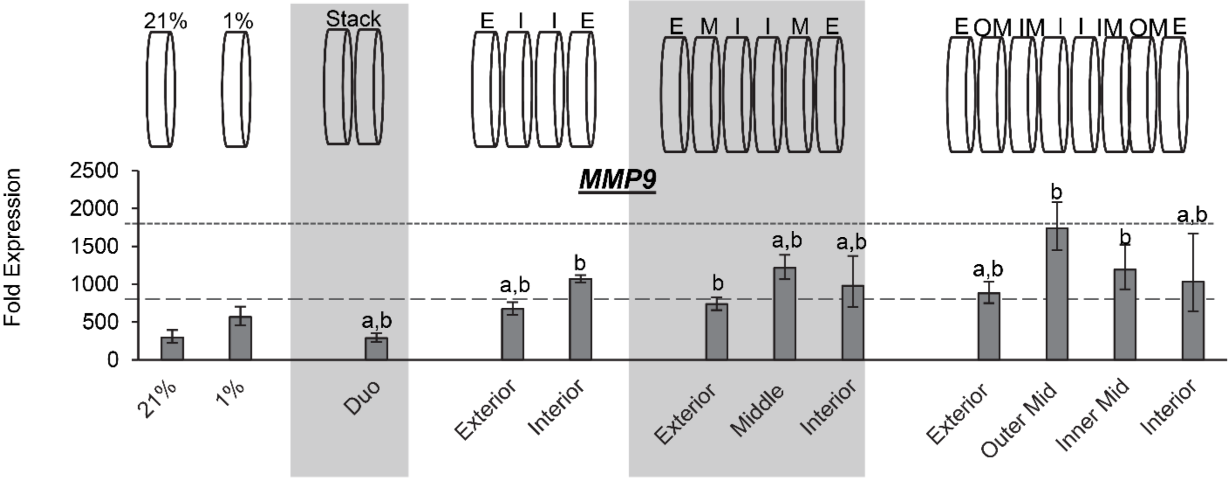

Figure 4.10. Evaluation of MMP9 expression of stacked scaffolds at each individual layer. Gene expression of MMP9 in SK-N-AS NB stacked scaffolds as compared to monolayer ambient oxygen culture 3 d post stacking. 21% (ambient) and 1% (low) represent single scaffolds grown at that oxygen concentration. Representation of each stacking thickness can be found above it on the graph. "E" corresponds to exterior, "I" corresponds to interior, "M" corresponds to the middle, "OM" corresponds to the outer middle, and "IM" corresponds to the inner middle. Data is presented as mean ± SD of three independent experiments. a denotes no statistical significance from single scaffolds grown at ambient oxygen, b denotes no statistical significance from single scaffolds grown at low oxygen. Asterisk indicate statistical significance between the groups (*** p<0.001, ** p<0.01, **p<0.05).

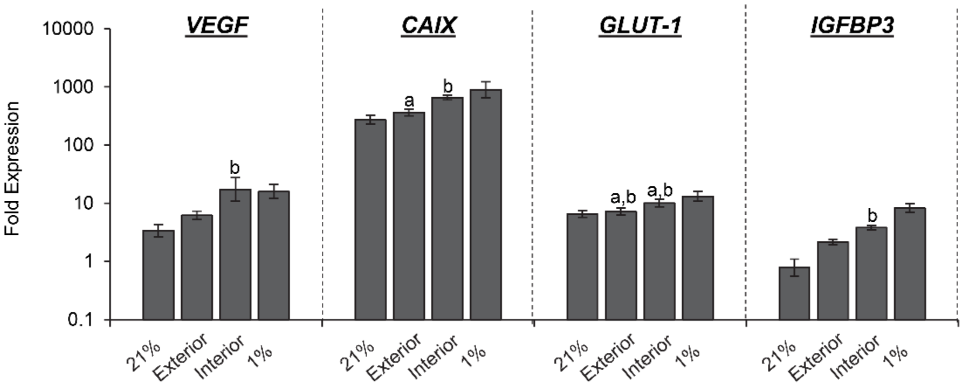

Figure 4.11. Evaluation of hypoxia related gene expression of KELLY NB stacked scaffolds. Evaluation of hypoxia related gene expression of KELLY quadruple stacked scaffolds 3 d post stacking. 21% (ambient) and 1% (low) represent single scaffolds grown at that oxygen concentration. All gene expression is normalized to a monolayer, ambient oxygen control. a denotes no statistical significance from single scaffolds grown at ambient oxygen, b denotes no statistical significance from single scaffolds grown at low oxygen. Data is presented as mean ± SD of three independent experiments.

4.3.6. Pimonidazole staining of stacks for hypoxia

To confirm hypoxic gradients SK-N-AS stacks of two, four, six, and eight, scaffolds were stained for pimonidazole after 3 d of culture (**Figure 4.12**). As demonstrated in Aim 1, scaffolds grown in ambient and low oxygen both exhibited positive pimonidazole staining (**Figure 4.12 A, B**). Double stacked scaffolds and quadruple scaffolds demonstrated a gradient of pimonidazole positive staining, with higher levels of staining observed in the center of the scaffolds (**Figure 4.12 C, D**). Double stacked scaffolds demonstrated lower pimonidazole binding then scaffolds grown in ambient oxygen. This is likely due to the use of a shaker improving oxygen diffusion in the stacked scaffolds, whereas single scaffolds were grown without the use of a holder or shaker. Pimonidazole staining in sextuple and octuple stacked scaffolds demonstrated less distinct gradients then double and quadruple stacked scaffolds (**Figure 4.12 E, F**). Sextuple stacked scaffolds demonstrated reduced pimonidazole binding at the surface of the stack as compared to the interior stack, further confirming changes observed in DNA content and gene expression. Octuple stacked scaffolds demonstrated no clear differences in pimonidazole staining. This further confirmed our previous results suggesting a lack of a gradient in the octuple stacks.

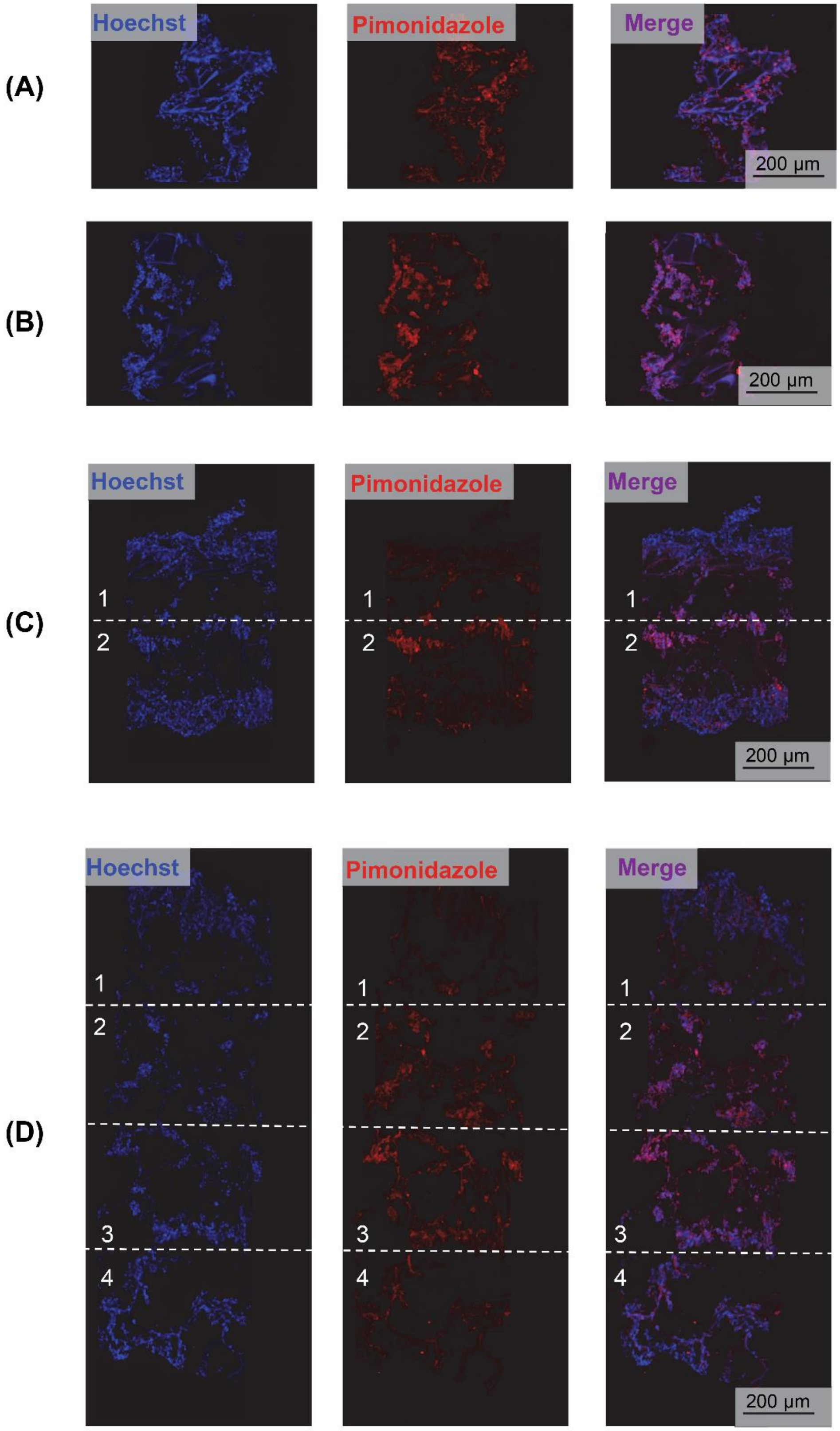
(A)
Hoechst
Pimonidazole
Merge
200 µm
(B)
200 µm
(C)
Hoechst
Pimonidazole
Merge
1
2
200 µm
(D)
Hoechst
Pimonidazole
Merge
1
2
3
4
200 µm

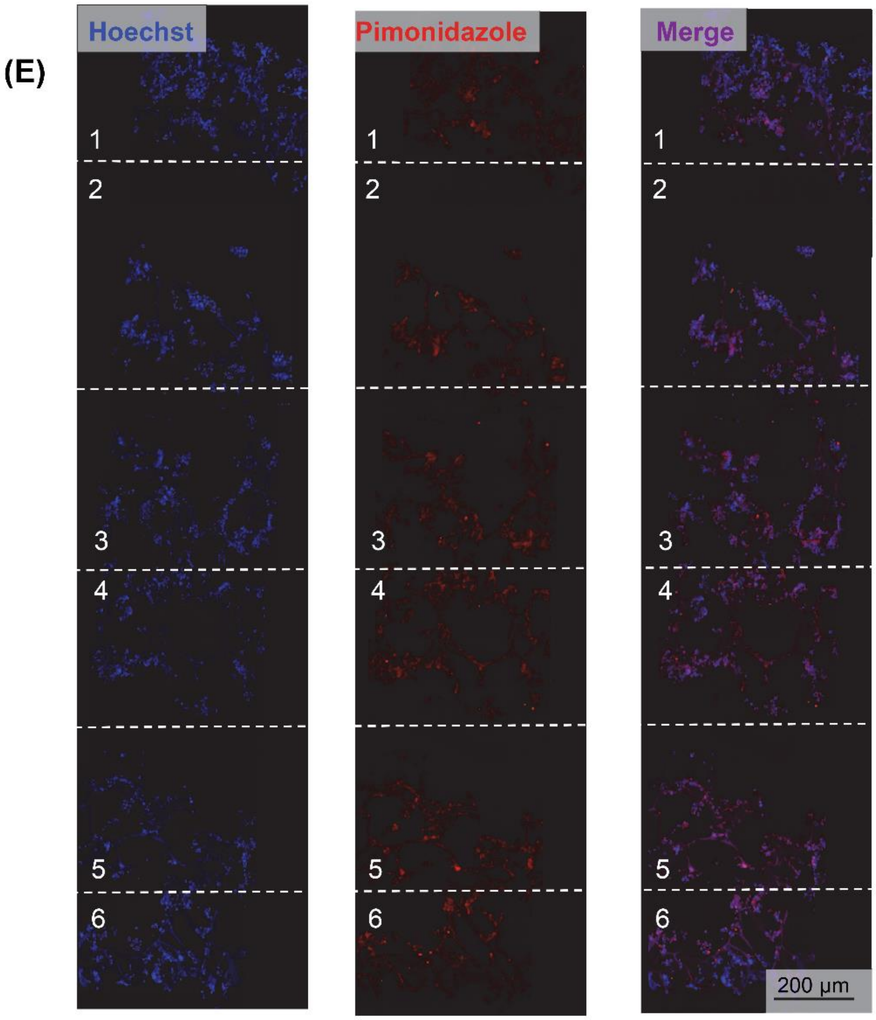
(E)
Hoechst
Pimonidazole
Merge
1
2
3
4
5
6
200 µm

(F)

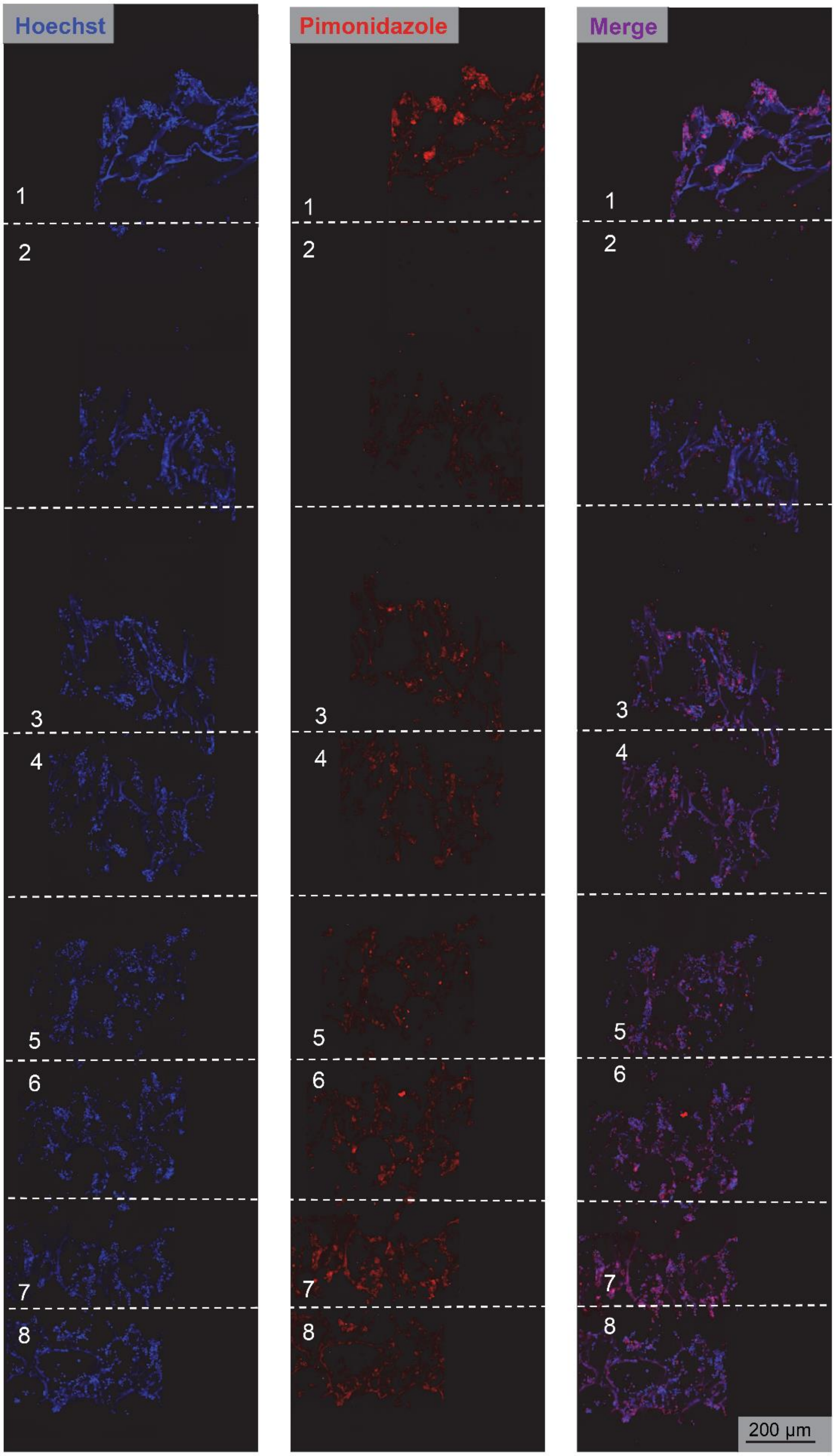

Figure 4.12. Pimonidazole staining of stacked scaffolds.
Pimonidazole staining of SK-N-AS NB scaffolds to visualize hypoxia within stacks 3 d post stacking. (A) Single scaffolds grown in ambient oxygen (21%). (B) Single scaffolds grown in low oxygen (1%). (C) Double stacked scaffolds. (D) Quadruple stacked scaffolds. € Sextuple stacked scaffolds. (F) Octuple stacked scaffolds.

4.4. Discussion

Hypoxia is a critical cell driven gradient in solid tumors that has been demonstrated to drive tumorigenesis, metastasis, and therapeutic resistance. However, few models exist that are capable of controllable oxygen gradients. In this work we used 200 µm silk scaffolds stacked together to generated cell driven oxygen gradients that mimic those of solid tumors. Silk scaffolds are mechanically strong and porous, allowing for temporal retention of scaffold dimensions and cell-driven oxygen and nutrient gradients. Further, silk does not contribute biologically to the system allowing for cell-driven responses to dominate the model system, unlike ECM-based hydrogels (e.g. Matrigel, Cultrex) which have been demonstrated to contain bioactive proteins and peptides [43].

Thick silk scaffolds, 600 μm demonstrated reduced cell distribution throughout the scaffold as compared to 200 μm scaffolds. Uneven cell distribution within large (thick), porous scaffolds has been previously identified as a limitation to these systems [44, 45]. *In vivo*, distances of 150-200 µm has been identified as the maximum diffusion distances for oxygen and nutrients due to cell-driven consumption [46, 47]. Scaffolds with a thickness of 200 µm demonstrated full cell infiltration creating a solid layer of cells. These scaffolds can then be stacked to form multilayer scaffolds that mimic a thicker tissue. To create these stacks, a scaffold holder was designed. COMSOL modeling of different well depths allowed for the design of a system capable of generating hypoxic gradients. When modeling of this system was performed with a range of scaffolds, it suggested that four scaffolds would be necessary to generate a hypoxic gradient.

Histological evaluation of stacks ranging from two to eight scaffolds demonstrated the presence of cells in each scaffold layer, regardless of stack thickness. Scaffold stacking was able to create a tumor model on the millimeter-scale of thickness, more relevant to that of solid tumors then monolayer culture. Additionally, unlike spheroids or other solid models, the stacks can be separated into single scaffolds allowing for analysis of individual levels without undergoing processing (e.g. fixing, lysis).

Using this *in vitro* system be were able to demonstrate controllable cell generated oxygen gradients within the stack. We confirmed that cells that are placed further from the source of oxygen and media showed increased expression of hypoxia markers *VEGF*, *CAIX*, *GLUT1,* and *IGFB3,* as well as a decrease in dsDNA. This indicates that these cells are experiencing decreased oxygen levels. Interestingly, the stack of eight scaffolds demonstrated a decrease in these hypoxia gene expression markers in the two interior most layers of the stack and no changes in dsDNA content. This could be due to the number of scaffolds exceeding the limitations of our holder design resulting in leaking. Staining of pimonidazole confirmed hypoxic gradients within the stacks. Stacks with thicknesses of two and four scaffolds demonstrated clear hypoxic gradients. These gradients were less distinct in the stacks of six to eight scaffolds, which aligned with the PCR data.

Here we demonstrate a silk fibroin culture capable of generating cell driven oxygen gradients that mimic those of an *in vitro* tumor. This system is advantageous as it can be assembled and/or disassembled at different times to control tumor properties. For example, stacks could be assembled, then disassembled and grown as single scaffolds to evaluate growth and cytokine secretion post oxygen deprivation. Work with two different NB cell lines demonstrates that our system is compatible with multiple cell types, which should extend to multiple cancer types.

4.5. Conclusion

In this work, we propose a silk-based, ECM-free method of modeling cell-driven oxygen gradients, that can be broadly applied to many cancer types. This silk-based culture system offers many advantageous to traditional monolayer and spheroid models. Use of different number of scaffolds has the potential to support a gradient of oxygen tensions throughout the stack, thus allowing for an understanding of fundamental biology and pathway changes. Analysis can be performed at each layer of the stack allowing for understanding of the cell population at precise regions of the model. In addition, we expect that additional cell types such as stromal and immune cells frequently found within the tumor microenvironment can be incorporated into different layers of the model. This would allow for a tumor model with oxygen and cytokine gradients similar to that of a physiological tumor.

This system also has the potential to be used for therapeutic screening as it mimics different diffusion barriers and oxygen tensions present within the tumor, which has been demonstrated to impact therapeutic response. For example, cells grown in silk scaffolds have been previously shown to have an enhanced response to therapeutics activated within hypoxia (e.g. tirapazamine). Using a stacked culture system, viability at each layer of the stack can be evaluated allowing for understanding of what regions of the tumor a therapeutic is infiltrating or is active in. Overall, we expect that this system is broadly applicable, both in fundamental tumor understanding and in therapeutic development and could be adopted for many cancer types.

4.6. Acknowledgements

The authors would like to thank Coulter Ralston for his assistance with ELISA assays, Katelyn Mistretta for her assistance in cryosectioning, and Elizabeth van Zyl for creating CAD drawings of the scaffold holders.

4.7. References

[1] J.A. Bertout, S.A. Patel, M.C. Simon, The impact of O2 availability on human cancer, Nat Rev Cancer 8(12) (2008) 967-75.

[2] R. Courtnay, D.C. Ngo, N. Malik, K. Ververis, S.M. Tortorella, T.C. Karagiannis, Cancer metabolism and the Warburg effect: the role of HIF-1 and PI3K, Mol Biol Rep 42(4) (2015) 841-51.

[3] L. D'Ignazio, M. Batie, S. Rocha, Hypoxia and Inflammation in Cancer, Focus on HIF and NF-kappaB, Biomedicines 5(2) (2017).

[4] S.R. McKeown, Defining normoxia, physoxia and hypoxia in tumours-implications for treatment response, Br J Radiol 87(1035) (2014) 20130676.

[5] B. Yu, A. Shah, B.Q. Wang, N. Rajaram, Q.L. Wang, N. Ramanujam, G.M. Palmer, M.W. Dewhirst, Measuring tumor cycling hypoxia and angiogenesis using a side-firing fiber optic probe, J Biophotonics 7(7) (2014) 552-564.

[6] S.K. Parks, Y. Cormerais, J. Pouyssegur, Hypoxia and cellular metabolism in tumour pathophysiology, J Physiol 595(8) (2017) 2439-2450.

[7] B. Muz, P. de la Puente, F. Azab, A.K. Azab, The role of hypoxia in cancer progression, angiogenesis, metastasis, and resistance to therapy, Hypoxia (Auckl) 3 (2015) 83-92.

[8] C.R. Justus, E.J. Sanderlin, L.V. Yang, Molecular Connections between Cancer Cell Metabolism and the Tumor Microenvironment, Int J Mol Med 16(5) (2015) 11055-11086.

[9] P. Fardin, A. Barla, S. Mosci, L. Rosasco, A. Verri, R. Versteeg, H.N. Caron, J.J. Molenaar, I. Ora, et al., A biology-driven approach identifies the hypoxia gene signature as a predictor of the outcome of neuroblastoma patients, Mol Cancer 9 (2010).

[10] L. Holmquist-Mengelbier, E. Fredlund, T. Lofstedt, R. Noguera, S. Navarro, H. Nilsson, A. Pietras, J. Vallon-Christersson, A. Borg, et al., Recruitment of HIF-1alpha and HIF-2alpha to common target genes is differentially regulated in neuroblastoma: HIF-2alpha promotes an aggressive phenotype, Cancer Cell 10(5) (2006) 413-23.

[11] H.M. Ameis, A. Drenckhan, M. Freytag, J.R. Izbicki, C.T. Supuran, K. Reinshagen, S. Holland-Cunz, S.J. Gros, Influence of hypoxia-dependent factors on the progression of neuroblastoma, Pediatr Surg Int 32(2) (2016) 187-92.

[12] M.R. Horsman, J. Overgaard, The impact of hypoxia and its modification of the outcome of radiotherapy, J Radiat Res 57 Suppl 1 (2016) i90-i98.

[13] G. Jimenez-Valerio, O. Casanovas, Angiogenesis and Metabolism: Entwined for Therapy Resistance, Trends Cancer 3(1) (2017) 10-18.

[14] J.J. Morton, G. Bird, Y. Refaeli, A. Jimeno, Humanized Mouse Xenograft Models: Narrowing the Tumor-Microenvironment Gap, Cancer Res 76(21) (2016) 6153-6158.

[15] A. Herrmann, M. Rice, R. Levy, B.L. Pizer, P.D. Losty, D. Moss, V. See, Cellular memory of hypoxia elicits neuroblastoma metastasis and enables invasion by non-aggressive neighbouring cells, Oncogenesis 4 (2015) e138.

[16] J. Chiche, K. Ilc, J. Laferriere, E. Trottier, F. Dayan, N.M. Mazure, M.C. Brahimi-Horn, J. Pouyssegur, Hypoxia-inducible carbonic anhydrase IX and XII promote tumor cell growth by counteracting acidosis through the regulation of the intracellular Ph, Cancer Res 69(1) (2009) 358-68.

[17] S. Daster, N. Amatruda, D. Calabrese, R. Ivanek, E. Turrini, R.A. Droeser, P. Zajac, C. Fimognari, G.C. Spagnoli, et al., Induction of hypoxia and necrosis in multicellular tumor spheroids is associated with resistance to chemotherapy treatment, Oncotarget 8(1) (2017) 1725-1736.

[18] A. Voissiere, E. Jouberton, E. Maubert, F. Degoul, C. Peyrode, J.M. Chezal, E. Miot-Noirault, Development and characterization of a human three-dimensional chondrosarcoma culture for in vitro drug testing, PLoS One 12(7) (2017) e0181340.
[19] S. Riffle, R.S. Hegde, Modeling tumor cell adaptations to hypoxia in multicellular tumor spheroids, J Exp Clin Cancer Res 36(1) (2017) 102.
[20] G. Xu, F. Yin, H. Wu, X. Hu, L. Zheng, J. Zhao, In vitro ovarian cancer model based on three-dimensional agarose hydrogel, J Tissue Eng 5 (2014) 2041731413520438.
[21] L. Chen, Z. Xiao, Y. Meng, Y. Zhao, J. Han, G. Su, B. Chen, J. Dai, The enhancement of cancer stem cell properties of MCF-7 cells in 3D collagen scaffolds for modeling of cancer and anti-cancer drugs, Biomaterials 33(5) (2012) 1437-44.
[22] T.M. Yeung, S.C. Gandhi, W.F. Bodmer, Hypoxia and lineage specification of cell line-derived colorectal cancer stem cells, Proc Natl Acad Sci U S A 108(11) (2011) 4382-7.
[23] E. Dondajewska, W. Juzwa, A. Mackiewicz, H. Dams-Kozlowska, Heterotypic breast cancer model based on a silk fibroin scaffold to study the tumor microenvironment, Oncotarget 9(4) (2018) 4935-4950.
[24] S.J. Hollister, Porous scaffold design for tissue engineering, Nat Mater 4(7) (2005) 518-24.
[25] A.S. Truong, M.R. Lockett, Oxygen as a chemoattractant: confirming cellular hypoxia in paper-based invasion assays, Analyst 141(12) (2016) 3874-82.
[26] M. Leung, F.M. Kievit, S.J. Florczyk, O. Veiseh, J. Wu, J.O. Park, M. Zhang, Chitosan-alginate scaffold culture system for hepatocellular carcinoma increases malignancy and drug resistance, Pharm Res 27(9) (2010) 1939-48.
[27] C. Correia, S. Bhumiratana, L.P. Yan, A.L. Oliveira, J.M. Gimble, D. Rockwood, D.L. Kaplan, R.A. Sousa, R.L. Reis, et al., Development of silk-based scaffolds for tissue engineering of bone from human adipose-derived stem cells, Acta Biomater 8(7) (2012) 2483-92.
[28] J. Rnjak-Kovacina, L.S. Wray, K.A. Burke, T. Torregrosa, J.M. Golinski, W. Huang, D.L. Kaplan, Lyophilized Silk Sponges: A Versatile Biomaterial Platform for Soft Tissue Engineering, Acs Biomater Sci Eng 1(4) (2015) 260-270.
[29] D.N. Rockwood, R.C. Preda, T. Yucel, X. Wang, M.L. Lovett, D.L. Kaplan, Materials fabrication from Bombyx mori silk fibroin, Nat Protoc 6(10) (2011) 1612-31.
[30] L.S. Wray, J. Rnjak-Kovacina, B.B. Mandal, D.F. Schmidt, E.S. Gil, D.L. Kaplan, A silk-based scaffold platform with tunable architecture for engineering critically-sized tissue constructs, Biomaterials 33(36) (2012) 9214-24.
[31] R. Derda, A. Laromaine, A. Mammoto, S.K. Tang, T. Mammoto, D.E. Ingber, G.M. Whitesides, Paper-supported 3D cell culture for tissue-based bioassays, Proc Natl Acad Sci U S A 106(44) (2009) 18457-62.
[32] B. Mosadegh, M.R. Lockett, K.T. Minn, K.A. Simon, K. Gilbert, S. Hillier, D. Newsome, H. Li, A.B. Hall, et al., A paper-based invasion assay: assessing chemotaxis of cancer cells in gradients of oxygen, Biomaterials 52 (2015) 262-71.
[33] M. Fischer, M. Skowron, F. Berthold, Reliable transcript quantification by real-time reverse transcriptase-polymerase chain reaction in primary neuroblastoma using normalization to averaged expression levels of the control genes HPRT1 and SDHA, J Mol Diagn 7(1) (2005) 89-96.
[34] I. Garcia, G. Mayol, J. Rios, G. Domenech, N.K. Cheung, A. Oberthuer, M. Fischer, J.M. Maris, G.M. Brodeur, et al., A three-gene expression signature model for risk stratification of patients with neuroblastoma, Clin Cancer Res 18(7) (2012) 2012-23.

[35] S.A. Roth, O.H. Hald, S. Fuchs, C. Lokke, I. Mikkola, T. Flaegstad, J. Schulte, C. Einvik, MicroRNA-193b-3p represses neuroblastoma cell growth via downregulation of Cyclin D1, MCL-1 and MYCN, Oncotarget 9(26) (2018) 18160-18179.

[36] S. Raghavan, P. Mehta, E.N. Horst, M.R. Ward, K.R. Rowley, G. Mehta, Comparative analysis of tumor spheroid generation techniques for differential in vitro drug toxicity, Oncotarget 7(13) (2016) 16948-61.

[37] P. Buchwald, FEM-based oxygen consumption and cell viability models for avascular pancreatic islets, Theor Biol Med Model 6 (2009) 5.

[38] R.H. Swerdlow, E. Lezi, D. Aires, J.H. Lu, Glycolysis-respiration relationships in a neuroblastoma cell line, Bba-Gen Subjects 1830(4) (2013) 2891-2898.

[39] J.J. Casciari, S.V. Sotirchos, R.M. Sutherland, Mathematical modelling of microenvironment and growth in EMT6/Ro multicellular tumour spheroids, Cell Prolif 25(1) (1992) 1-22.

[40] P. Han, D.M. Bartels, Temperature dependence of oxygen diffusion in H2O and D2O, J Phys Chem-Us 100(13) (1996) 5597-5602.

[41] K.L. Eales, K.E.R. Hollinshead, D.A. Tennant, Hypoxia and metabolic adaptation of cancer cells, Oncogenesis 5 (2016).

[42] K. Groebe, P. Vaupel, Evaluation of Oxygen Diffusion Distances in Human-Breast Cancer Xenografts Using Tumor-Specific Invivo Data - Role of Various Mechanisms in the Development of Tumor Hypoxia, Int J Radiat Oncol 15(3) (1988) 691-697.

[43] N.C. Talbot, T.J. Caperna, Proteome array identification of bioactive soluble proteins/peptides in Matrigel: relevance to stem cell responses, Cytotechnology 67(5) (2015) 873-83.

[44] S.L. IshaugRiley, G.M. Crane, A. Gurlek, M.J. Miller, A.W. Yasko, M.J. Yaszemski, A.G. Mikos, Ectopic bone formation by marrow stromal osteoblast transplantation using poly(DL-lactic-co-glycolic acid) foams implanted into the rat mesentery, J Biomed Mater Res 36(1) (1997) 1-8.

[45] A.S. Goldstein, T.M. Juarez, C.D. Helmke, M.C. Gustin, A.G. Mikos, Effect of convection on osteoblastic cell growth and function in biodegradable polymer foam scaffolds, Biomaterials 22(11) (2001) 1279-88.

[46] P. Carmeliet, R.K. Jain, Angiogenesis in cancer and other diseases, Nature 407(6801) (2000) 249-57.

[47] M.C. Lewis, B.D. MacArthur, J. Malda, G. Pettet, C.P. Please, Heterogeneous proliferation within engineered cartilaginous tissue: The role of oxygen tension, Biotechnol Bioeng 91(5) (2005) 607-615.

Conclusions and Future Work

5.1. Overview

The work in this thesis describes the development of a 3D *in vitro* tumor model capable of generating cell driven microenvironment changes, specifically hypoxia. The use of lyophilized silk fibroin provided structure and spatial control for cells to grow on without the use of ECM components. Impact of growth on 3D scaffolds in ambient and low oxygen was characterized through gene expression and cytokine secretion. We determined that growth in 3D induces cell driven hypoxia and induces expression of proinflammatory cytokines, such as GM-CSF, IL-8, and MCP-3. Further, we developed a culture system for stacking of the cell-laden silk scaffolds to generate controllable hypoxic gradients. Scaffolds can be seeded with cells, grown for 3 d, allowing cells to fully infiltrate the scaffold, then stacked using a PTFE holder. Post-culture, stacks can be separated for independent analysis. Stacks of different thicknesses were evaluated for presence of hypoxia. This analysis demonstrated a gradient of hypoxia through the different layers of the stack, similar to that of a physiological tumor.

5.2. Results and Conclusions

5.2.1. Specific Aim 1: Evaluate the impact scaffolded NB growth and hypoxia on relevant gene expression, cytokine secretion, and drug sensitivity.

Many studies have demonstrated that monolayer cultured cells are not effective at mimicking the *in vivo* tumor microenvironment. Current model systems evaluate hypoxia as an independent factor or as a result of 3D culture, however they fail to make direct comparisons between hypoxia and 3D culture. This prevents a complete understanding of the role of 3D culture and hypoxia in changes in pathway expression and therapeutic response. We developed a scaffolded NB system capable of growth of NB cells. Low oxygen incubators were utilized to induce hypoxia in both monolayer and scaffolded culture. These were chosen as other methods of inducing hypoxia (typically chemical ones) have been demonstrated to induce other pathway related changes (such as metabolic).

Cell seeding on silk scaffolds demonstrated the maximum number of seeded cells on scaffolds as approximately 2 million cells. Density of cells on silk scaffold could be controlled based on number of cells attached. The effects of culturing NB cells on scaffolds (both in ambient and low oxygen) were evaluated through analysis of dsDNA content, proliferation (ki67 staining), and apoptosis (TUNEL staining). Scaffolded NB cells demonstrated similar levels of dsDNA content to non-scaffolded cells. Limited proliferation and apoptosis were observed. This result is not unexpected, as 3D culture and hypoxia has been demonstrated to slow cell proliferation. Based on preliminary studies, we identified 1 million cells as the cell number to move forward with. However, in future works, if a higher initial cell number is desired, a higher cell number can be seeded.

COMSOL modeling of scaffolded NB in ambient and low oxygen was performed to determine that oxygen gradients could be generated with the model. We identified hypoxic regions under ambient 3D culture conditions and confirmed the oxygen levels of scaffolded NB in low oxygen. These regions suggested that low oxygen and hypoxic environments were present in scaffolded NB. This was due to the highly metabolic nature of NB cells outcompeting oxygen diffusion into the scaffolds. Staining for the hypoxia marker pimonidazole confirmed the presence of hypoxia in both low and ambient oxygen scaffolded cultures.

Next we examined the impact of hypoxia and scaffolded culture on gene and cytokine secretion. We observed a significant upregulation of hypoxia relevant genes, furthering confirming the presence of hypoxia. Cytokine analysis demonstrated a significant upregulation of proinflammatory cytokines GM-CSF, IL-8, and MCP-3 in 3D, but not hypoxia, suggesting 3D culture is necessary to mimic a microenvironment similar to *in vivo*. While hypoxia was sufficient in upregulating a subset of proinflammatory cytokines, upregulation of select cytokines only occurred in scaffolded culture suggesting that a combination of 3D culture and oxygen gradients are necessary to accurately mimic the tumor microenvironment.

Development of *in vitro* systems that can be used to accurately assess therapeutic efficacy represents a critical hurdle in cancer research. Traditional monolayer cultures fail to mimic diffusion barriers and resistance mechanisms that are present *in vivo*. We utilized the scaffolded NB system in ambient and low oxygen to evaluate response to different therapeutics. Etoposide is a clinically used cytotoxic chemotherapy (topoisomerase inhibitor). Scaffolded NB demonstrated a resistance to treatment with etoposide both at ambient and low oxygen. Use of a hypoxia activated therapeutic tirapazamine demonstrated a response in both scaffolded and low oxygen culture, but not monolayer ambient oxygen culture. This demonstrated that our system is able to differentiate the efficacy of different therapeutics (both toxic and microenvironment based).

To conclude Specific Aim 1: Evaluate the impact of scaffolded NB growth and hypoxia on relevant gene expression, cytokine secretion, and drug sensitivity, we determined that scaffolded NB in low and ambient oxygen is capable of capturing different levels of the tumor microenvironment. This resulted in differential gene and cytokine secretion, as well as therapeutic efficacy. Taken together, these data suggest that scaffolded NB is more representative of the tumor microenvironment then traditional monolayer culture. Growth of different cell lines and cancer types in 3D and low oxygen can allow for evaluation of different pathway expression and response to therapeutics.

5.2.2. Specific Aim 2: Design, fabricate, and evaluate a culture system capable of controllable cell driven microenvironments.

In this section of the thesis, we incorporated the findings from Specific Aim 1 by developing a model capable of mimicking the effects of low oxygen incubators on scaffolded NB in a single culture system. First, in an effort to develop a model with a more comprehensive oxygen gradient we evaluated the use of larger dimension scaffolds. Analysis of cell content in the scaffolds through quantification of dsDNA, metabolic activity, and visualization through histology demonstrated that cells were not able to fully infiltrate scaffolds. Therefore, we determined that stacking of pre-seeded thin scaffolds had the potential to develop cell driven oxygen gradients.

To achieve this, we designed a scaffold holder using COMSOL modeling. Modeling of different scaffold holder setups predicted oxygen gradients based on oxygen diffusion in the media and into the scaffolds. This modeling was extended to different scaffold numbers which predicted different oxygen gradients based on scaffold number.

To evaluate impact of stacking using different numbers of scaffolds in the scaffold holder, we first performed histology and evaluated dsDNA content. Both histology and dsDNA content demonstrated cells throughout the scaffold. In stacks of four and six scaffolds, the dsDNA content at the interior was similar to that of low oxygen scaffolded culture. This suggested that differences existed between the exterior and interior of the stacks existed similar to that of scaffolds grown in different oxygen levels.

These changes were further characterized through changes in gene expression and positive pimonidazole staining. Hypoxia induced gene expression changes were present in the stacks of four scaffolds and six scaffolds with significant differences present at the interior of the stacks. Pimonidazole staining of stacks demonstrated the presence of oxygen gradients in two, four, and six scaffolds. Interestingly, stacks of eight scaffolds demonstrated limited differences in dsDNA content, gene expression, and pimonidazole staining. Lack of a hypoxic gradient in stacks of eight scaffolds could potentially be due to leakage of the scaffold holder. Taken together, this data demonstrates the fabrication of a tumor model with a range of oxygen gradients relevant to that of an *in vivo* tumor and the identification of four and six scaffolds as the optimal number of layers with our design.

To conclude Specific Aim 2: Design, fabricate, and evaluate a culture system capable of controllable cell driven microenvironments, we developed a stacked culture system capable of cell driven oxygen gradients. Comparison of different layers of the stacks to scaffolds grown in low and ambient oxygen allowed for correlation of dsDNA level and gene expression at the interior of the stacked culture to that of scaffolds grown in low oxygen. Additionally, using a hypoxia stain we were able to visualize these gradients throughout the stack. As this system employs layers of scaffolds, it can be separated for layer by layer analysis. This could be highly effective for future work examining different levels of the tumor microenvironment.

5.3. Future Work

The ultimate goal of this dissertation was to develop a culture system for 3D growth of neuroblastoma capable of capturing different levels of the tumor microenvironment, specifically cell driven hypoxic gradients. In accomplishing this goal, we determined the impact of hypoxia and 3D culture on NB cell lines and developed a stacked culture model. To further develop this silk scaffold technology, work can be done to incorporate multiple cell types into the system, characterize additional pathways in the scaffolds, evaluate therapeutic response of the stacks, incorporate patient tumor samples, and implant scaffolds *in vivo*. Further, the stacking system could be redesigned to be high throughput and adapted into a bioreactor system.

5.3.1. Evaluation of HIF activation in scaffolded culture

In this work transcriptional targets of HIF were evaluated to determine if hypoxic regions were present in scaffolds. Transcriptional targets of HIF including VEGF, CAIX, and GLUT1 are frequently used as indicators of HIF activity as HIF protein is rapidly degraded, making accurate analysis difficult [1]. However, multiple transcription factors target these genes [2, 3]. To directly determine HIF activation and location (cytosol vs. nucleus) a fluorescent reporter system could be utilized. Cells can be tagged with GFP or RFP labeled HIF, allowing for visualization of HIF protein localization. This method has been previously employed to understand the role of HIF *in vitro* and *in vivo* [4, 5].

There are three HIF transcription factors HIF-1α, HIF-2α, and HIF-3α. These transcription factors are found in the cytosol, but under hypoxic conditions translocate to the nucleus and dimerize with their respective β subunits leading to transcription of downstream pathways. In cancer, hypoxia regulated pathways changes have been linked to HIF-1α and HIF-2α, whereas HIF-3 α is less extensively studied [6]. In NB, HIF-1α and HIF-2α have both been detected and been demonstrated to correlate to patient outcome, whereas HIF-3α has only been detected at extremely low levels [7]. There is a large amount of overlap in the transcriptional targets of HIF-1α and HIF-2α, however there are some key differences. HIF-1α is primarily responsible for metabolic changes, whereas HIF-2α is linked to an undifferentiated state and stemness in NB [8, 9]. Additionally, MYCN status in NB has been linked to differential expression of HIF-1α and HIF-2α [9]. Therefore, understanding the impact of scaffolded culture on expression of HIF-1α and HIF-2α is important.

For this work, a dual reporter system with GFP-tagged HIF-1α and RFP-tagged HIF-2α could be utilized. Plasmids for HIF-1α and HIF-2α could be purchased from addgene (pg-HIF-

1alpha-EGFP, pg-dsRedXP-HIF-2alpha) [10]. These plasmids could then be grown up in bacteria (DH5alpha bacteria under Kanamycin selection) and the plasmid could be purified using a Maxiprep (Qiagen). Cells could then be transfected with GFP-tagged HIF-1α and/or RFP-tagged HIF-2α. This would allow for elucidation of how scaffolded culture impacts both HIF pathways and direct correlation to HIF status. As NB cell lines have been demonstrated to express HIF-1 and HIF-2 differentially (primarily based on MYCN status), the first step would be to transfect cells with GFP-HIF-1α and RFP- HIF-2α and confirm positive expression under short term and chronic hypoxia. HIF-1α and HIF-2α could then be examined in scaffolded culture under ambient and low oxygen. This would allow for understanding of whether transcriptional changes are due to HIFs and where those changes were localized in scaffolds.

5.3.2. Co-culture of NB and cells from tumor microenvironment in scaffolds

Within the NB microenvironment, stromal cells (fibroblasts, endothelial cells) and immune cells are frequently present [11, 12]. These cells contribute to the malignant nature of the tumor through cell-cell interactions, paracrine signaling, and secreted factors. Cancer cells promote migration of stromal and immune cells into the tumor environment through secretion of cytokines and inflammation within the tumor. Culture of NB cells with stromal and immune cells has been evaluated *in vitro* in monoculture models, however, our work has demonstrated fundamental differences in monolayer and scaffolded culture [11-13]. Use of scaffolded and stacked culture systems with multiple cell types has the potential to better understand signaling and malignant drivers within the tumor microenvironment.

Macrophages can be acquired in the form of cell lines (THP-1) or isolated from peripheral blood based on surface expression of CD14. Similarly, CD16- expressing natural killer (NK) cells, and T-cells can be acquired or isolated. Immune cells can be cocultured directly or indirectly with scaffolds. Our data suggests the upregulation of proinflammatory cytokines that have the poteintial to recruit immune cells into the scaffolds. For initial experiments, medium from scaffolds and monolayer cells grown under ambient and low oxygen could be used for indirect coculture on immune cells (NK cells, macrophages). This would assist in identifying changed based on secreted factors. Gene expression and immunostaining, could be used to determine activation and/or polarization of the immune cells. For example, macrophages are can be polarized to TAM in the presence of secreted cytokines from cancer cells. This polarization can be measured through gene expression. Once the impact of secreted factors on immune cell activation has been evaluated, a direct co-culture system could be employed. Primary co-culture experiments would be performed utilizing a polymer trasnwell system with scaffolds or monolayer cancer cells on the bottom of the transwell system and immune cells in the top level of the transwell system. Post-culture gene expression, cytokine secretion, and cell morphology could be evaluated. This would allow for elucidation of cross talk between cancer cells and immune cells. Finally, immune cells could be incorporated into the scaffolded tumor model (both the stacked and single scaffold system). Ratios of immune cells as well as location with the stacked culture could be controlled. This would allow for a more accurate tumor representation, in addition provide a more accurate system for therapeutic testing, specifically for immunotherapuetics.

Stromal cells such as fibroblasts have been associated with high risk NB and demonstrated to exert a protumerogenic effect on NB cells [11, 12]. In addition, they have been demonstrated to inhibit apoptosis and induce resistance to therapeutics [11]. Fibroblast (or hmscs with a fibroblast phenotype) could be cocultured both directly and indirectly with NB cells in monolayer and scaffolded culture. Impact on viability, proliferation, and morphology of both cancer and stromal cells could be evaluated. Media from indirect and direct coculture could be analyzed for cytokine secretion. Gene expression in stromal cells (oncogenes) and in the cancer cells (PI3K pathway) could be evaluated. This could guide understanding of the role of the tumor stroma in cancer progression. In addition, CAFs have been demonstrated to reduce cancer cell response to therapeutics. Therefore, integrating CAFs at different rations into the tumor model and evaluating therapeutic efficacy could create are more accurate tumor model.

Our data suggests the upregulation of angiogenic factors (IL8, VEGF) in scaffolded NB culture. High levels of angiogenic factors has been associated with advanced tumor stage in NB [14]. It has also been associated with metastatic disease and poor outcomes. This silk-based culture system could be used to evaluate infiltration and migration of vascular cells into the tumor bed. .Impact on viability, proliferation, and morphology of both cancer and stromal cells could be evaluated. Media from indirect and direct coculture could be analyzed for cytokine secretion. Finally a cancer model with vascular cells on the exterior (adjacent to the media source) could be generated to better understand tumor/vascular interactions. For testing of therapeutics, this could represent the diffusion barrier presented by vascular cells *in vivo*.

To best mimic the *in* vivo tumor microenvironment a complex multicellular model would need to be developed. This model would contain a mixture of stromal and immune cells in combination with cancer cells/ Development of these multicell culture models could assist in understanding functional biology questions as well as developing more effective therapeutics.

5.3.3. Examination of extracellular adenosine as a function of hypoxia and 3D culture

The hypoxic tumor microenvironment has been demonstrated to exhibit increased extracellular adenosine *in vitro* as well as *in vivo* [15] [16]. Increased extracellular adenosine occurs as a result of dying cells releasing ATP [17]. ATP is then degraded by CD73 and CD39 enzymes, converting ATP to adenosine [18, 19]. In normoxic conditions, the concentrations of ATP and ADP are balanced, however, in hypoxia there is an increase of ADP. ADP can be degraded into adenosine via 5'-nucleotidase, acting as an additional source of adenosine [20]. Functionally, adenosine inhibits immune cell activation by binding to adenosine receptors on the surface of immune cells [15]. These receptors can impact the G protein (either activation or inhibition), which regulates the intracellular adenyl cyclase-cAMP system. Receptors A_1 and A_3 decrease cAMP, while receptors A_{2A} and A_{2B} increase cAMP [15]. Increases in intracellular cAMP can decrease immune cell function through the cAMP/PKA signally pathway. Thus, understanding of the role of adenosine in solid tumors is essential.

Analyzing the content of intracellular and extracellular adenosine as well as surface associated CD73 and CD39 enzymes can be evaluated. Presence of adenosine in this culture system would further validate its relevance to the *in vivo* microenvironment. Once this has been identified response to adenosine receptor (A_{2A} and A_{2B}) antagonists such as SCH58261, SCH420814 and PSB1115 could be evaluated in combination with immune cells.

5.3.4. Evaluation of therapeutic response in a stacked culture system

Stacked culture systems have demonstrated gradients of oxygen based on the layer cells are present in. Presence of hypoxia has previously been demonstrated to impact therapeutic response *in vitro* and *in vivo*. Our stacked culture system could be used to examine therapeutic efficacy. The ability to evaluate therapeutic response at different oxygen gradients could provide insight into how hypoxia effects different parts of tumors. This is further enhanced by the use of stacks of scaffolds. Stacks can be separated into individual layers for analysis. This would allow us to examine the sensitivity to therapeutics at each layer, something that cannot be achieved in spheroid culture. Outside of chemotherapeutics and hypoxia dependent therapies use of the stacking system for evaluation of immunotherapies as well as pathway specific inhibitors.

To bettwe evaluate therapeutic efficacy cells stacks of cells could be evaluated. Cells could first be seeded in monolayer and in scaffolds. After 3 d scaffolds could be stacked and allowed to grow for an additional 3 d. Medium containing therapeutic could then be applied to scaffolds, stacks of scaffolds, or monolayer cells. To analyze therapeutic efficacy a PicoGreen dsDNA assay could be used. Stacks could be analyzed both in bulk and in a layer by layer method. This would allow for understanding of how therapeutics impact each level of the stack. In addition, scaffolds and stacks could be frozen and cryosectioned. Histology (H&E) and TUNEL staining could be performed to identify regions of cell death within scaffolds/stacks.

5.3.5. Use of patient derived NB cells in silk model

Patient derived xenografts (PDX) are cells taken directly from the patient and serially passaged in mice. This eliminates adaptations acquired through grown in traditional *in vitro* 2D cell culture and has been determined to retain a phenotype closer to that of the patient tumor [21-23]. Recently our lab has acquired 5 PDX samples from the Childhood Solid Tumor Network (St. Jude's) (**Table 5.1**). Biopsies were taken of these frozen stocks to determine if any cells had the potential to grow *in vitro*. One PDX line was able to be cultured and demonstrated a mix of adherent and non-adherent cells **(Figure 5.1**).

Additionally, preliminary culturing procedures have been determined for these cells (**Appendix I**). We hypothesize that we can use PDX cells to better mimic patient tumors. Use of our system for patient-derived tumors could provide insight into relevant pathway changes as well as assist in development of therapeutic strategies. PDX cells could first be grown in monolayer and scaffolded culture, under both ambient and low oxygen. RNA seq could be used to identify genetic changes based on culture conditions. Dot blots could be used to characterize the secrotome of PDX cells. Finally, therapeutic efficacy on PDX cells could be evaluated under different culture conditions.

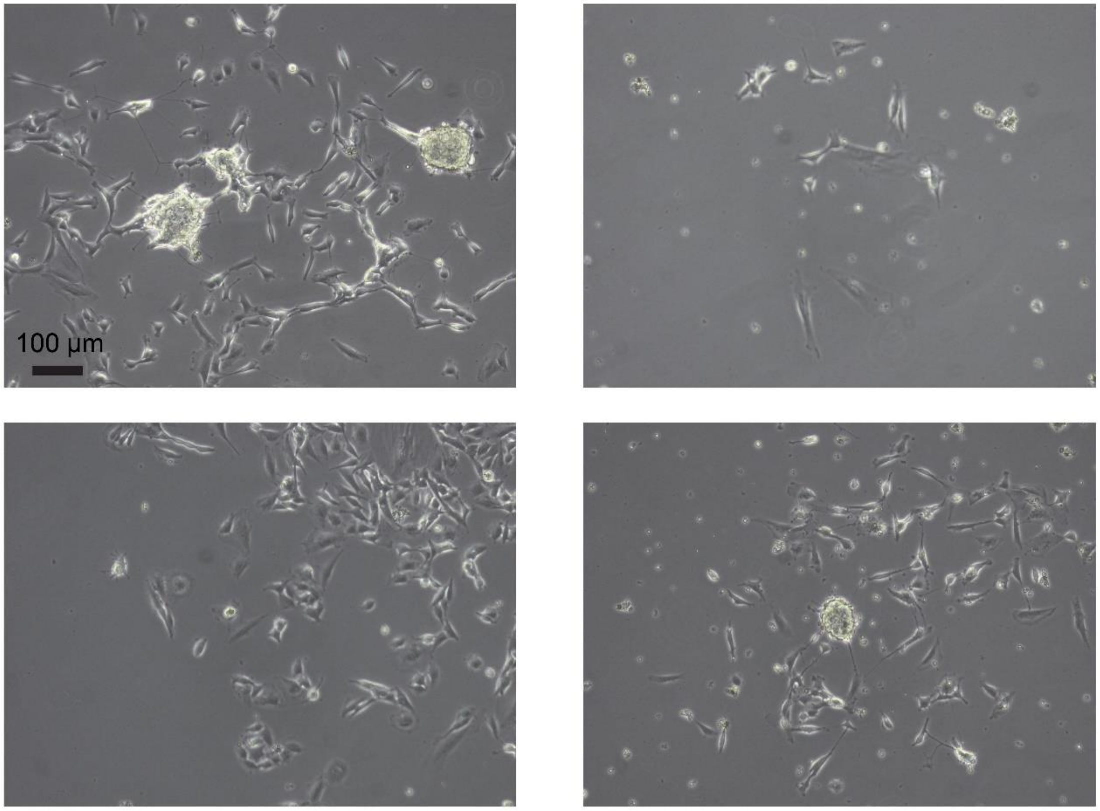

Figure 5.1. Images of cultured PDX cell line.
Representative images of PDX tumor Mast 3.2_142_RBC- after 21 days in culture, prior to being passaged. A mixed population of spheroids and adherent cells can be observed.

Table 5.1.PDX Tumors from St. Jude's (Childhood Solid Tumor Network)

Tumor	Status
Mast 191.B-1.2	Did not grow *in vitro*
Mast 3.2_142 RBC-	Growing slowly *in vitro*
Mast 190_1.1	Did not grow *in vitro*
Mast 121_3	Did not grow *in vitro*
Mast 78_11	Did not grow *in vitro*

5.3.6. Understanding interactions between cells and silk

Previous literature has demonstrated the ability for cells to adhere to and proliferate on silk fibroin scaffolds [24-27]. However, the specific mechanisms by which cells adhere to silk scaffolds remains unclear. The hypothesized mechanism for cell adhesion to silk scaffolds involves interactions between media components (proteins present in serum or secreted by cells) and the silk fibroin creating binding sites for cells. This is similar to the mechanism by which cells adhere to tissue culture plates. Tissue culture plates are treated to be negatively charged, proteins (either in the medium or cell secreted) then adhere through electrostatic interactions to plate surface creating binding sites for cells. As silk fibroin is negatively charged, a similar mechanism is potentially present between cells and silk. In order to elucidate the mechanism of cell binding silk could be soaked in medium (either non conditioned media or conditioned media from cells) to allow for proteins to interact with the silk. Mass spectrometry could then be employed to identify proteins or peptides present on the silk surface. Once these proteins have been identified to determine binding interactions immunostaining for proteins or associated integrins, or co-immunoprecipitation could be employed. This would be useful in understanding cell-silk interactions and identifying adhesion properites of different cell types to silk.

5.3.7. Implantation of scaffolded NB in *vivo*

While the goal of this project is to develop an *in vitro* tumor model, animal studies can be performed to validate these *in vitro* models for clinical relevance. Scaffolded NB and injected NB cells can be implanted into a murine model after preconditioning in ambient oxygen or hypoxic conditions. Tumor growth, vascularization, immune cell infiltration, and metastasis can be evaluated. Previous work has examined *in vivo* implantation of scaffolded cancer cells using a stacked paper-based system [28]. Researchers were able to examine invading cells from the surrounding microenvironment in response to different gradients. In addition, comparative analysis implanted cells grown in monolayer with implanted scaffolds can allow for understanding of morphologic and pathway changes promoted by scaffolded growth and the presence of an intact stroma.

For this work, female NCr mice at 6–8 weeks of age will be used. 1 x 10^6 SK-N-AS or KELLY human NB cells (in 100 µL Matrigel or on silk scaffolds) will be injected subcutaneously in the left flank region. Control animals will receive silk and Matrigel only. Tumor progression will be monitored every two to three days via caliper measures of the two longest perpendicular axes in the x-y plane. Tumor volume will be calculated as $V=(xy^2)/2$, where y is defined as the shortest of the perpendicular axes. Tumors will be monitored and be harvested at predetermined timepoints of 3 d, 7 d, 10 d, 14 d, 21 d, and 28 d post-implantation. If the tumor volume exceeds

1.5 cm^3 or if humane endpoints are reached prior to the timepoints, tumors will be harvested. Tumors harvested at predetermined endpoints will be evaluated for histology, infiltration of stromal/immune cells, and a subset will be taken for RNA extraction. Samples lysed for RNA can be evaluated for a panel of hypoxic genes or could be evaluated for a large number of gene changes using RNA seq.

5.3.8. Development of a high throughput stacking system

While our system is effective in modeling hypoxic gradients within the tumor microenvironment, it requires a large number of cells and uses a large volume of medium. This is inefficient for high-throughput drug screening. However, our current system could be modified for high throughput therapeutic testing. Scaffolds could be biopsy punched to smaller diameters (1-2 mm, as compared to 6 mm). This would decrease the cell number and amount of medium required for culture. Additionally, the holder system for silk scaffolds could be modified to hold smaller scaffolds and accommodate multiple stacks into one holder.

5.3.9. Development of a bioreactor system for silk scaffolds

One challenge of this culture system is adequately supplying the scaffolds with medium (nutrients) and oxygen. This requires large media reservoirs and shaking to enhance oxygen diffusion into the culture. Our lab has been developing a bioreactor system capable of flowing medium over silk scaffolds and recycling medium. Currently, this system has been designed to hold 10 mm diameter silk scaffolds and has not been optimized for thin silk scaffolds or stacks. This perfusion bioreactor system could be designed to hold scaffolds or stacks scaffolds under continuous medium flow. Different perfusion rates could be evaluated to optimize cell viability and impact on oxygen concentrations.

In addition, other cancer microenvironment cells could be incorporated into the bioreactor system. Previously, an MQP team in our lab (3D Perfusable, Endothelialized Tumor Model, 2017-2018) determined that vascular cells could be grown un the surface of silk scaffolds and cultured in a bioreactor setup. Seeding of vascular cells on the outermost layer of the scaffold could mimic the interface between the cancer cells and the vasculature. As cancer cells have been demonstrated to migrate into layers of vascular cells, this system would better mimic the *in vivo* tumor environment. Additionally, medium containing circulating cells such as immune cells could be flowed over the scaffold. A perfusion-based cell infiltration system would better mirror the way that the cells interact with the tumor *in vivo*.

5.4. Final Conclusions

In this thesis, we developed tools to examine the impact of scaffolded growth and hypoxia on cancer cells. We investigated the impact of these culture systems and found that a combination of scaffolded growth and different oxygen gradients is necessary to accurately mimic *in vivo* tumors. Significant changes in gene expression, cytokine secretion, and therapeutic efficacy Combinatorial use of low oxygen incubators and scaffolded growth allowed us to elucidated changes dependent on hypoxia as compared to those driven by scaffolded culture.

We then progressed this system to create a stacked scaffolded system capable of combining the effects observed in scaffolds grown in low oxygen with scaffolds grown in ambient oxygen. This resulted in a single culture system with cell driven oxygen gradients relevant to that a physiological tumor. These data suggest that these models will be able to identify critical pathway and therapeutic responses in tumors. Evaluation of these systems with different NB cell lines has demonstrated that these gradients are conserved. This suggests that this system could be broadly applicable to multiple cancer types.

5.5. References

[1] S. Salceda, J. Caro, Hypoxia-inducible factor 1alpha (HIF-1alpha) protein is rapidly degraded by the ubiquitin-proteasome system under normoxic conditions. Its stabilization by hypoxia depends on redox-induced changes, J Biol Chem 272(36) (1997) 22642-7.
[2] J. Josko, M. Mazurek, Transcription factors having impact on vascular endothelial growth factor (VEGF) gene expression in angiogenesis, Med Sci Monit 10(4) (2004) RA89-98.
[3] A. Barthel, S.T. Okino, J. Liao, K. Nakatani, J. Li, J.P. Whitlock, Jr., R.A. Roth, Regulation of GLUT1 gene transcription by the serine/threonine kinase Akt1, J Biol Chem 274(29) (1999) 20281-6.
[4] T.Q. Kong, H.K. Eltzschig, J. Karhausen, S.P. Colgan, C.S. Shelley, Leukocyte adhesion during hypoxia is mediated by HIF-1-dependent induction Of beta 2 integrin gene expression, Proc Natl Acad Sci U S A 101(28) (2004) 10440-10445.
[5] X.H. Liu, A. Kirschenbaum, M. Lu, S. Yao, A. Dosoretz, J.F. Holland, A.C. Levine, Prostaglandin E2 induces hypoxia-inducible factor-1alpha stabilization and nuclear localization in a human prostate cancer cell line, J Biol Chem 277(51) (2002) 50081-6.
[6] J.C. Jun, A. Rathore, H. Younas, D. Gilkes, V.Y. Polotsky, Hypoxia-Inducible Factors and Cancer, Curr Sleep Med Rep 3(1) (2017) 1-10.
[7] S. Pahlman, S. Mohlin, Hypoxia and hypoxia-inducible factors in neuroblastoma, Cell Tissue Res 372(2) (2018) 269-275.
[8] A. Pietras, L.M. Hansford, A.S. Johnsson, E. Bridges, J. Sjolund, D. Gisselsson, M. Rehn, S. Beckman, R. Noguera, et al., HIF-2alpha maintains an undifferentiated state in neural crest-like human neuroblastoma tumor-initiating cells, Proc Natl Acad Sci U S A 106(39) (2009) 16805-10.
[9] G. Qing, N. Skuli, P.A. Mayes, B. Pawel, D. Martinez, J.M. Maris, M.C. Simon, Combinatorial regulation of neuroblastoma tumor progression by N-Myc and hypoxia inducible factor HIF-1alpha, Cancer Res 70(24) (2010) 10351-61.
[10] S.E. Taylor, J. Bagnall, D. Mason, R. Levy, D.G. Fernig, V. See, Differential sub-nuclear distribution of hypoxia-inducible factors (HIF)-1 and -2 alpha impacts on their stability and mobility, Open Biol 6(9) (2016).
[11] L. Borriello, R. Nakata, M.A. Sheard, G.E. Fernandez, R. Sposto, J. Malvar, L. Blavier, H. Shimada, S. Asgharzadeh, et al., Cancer-Associated Fibroblasts Share Characteristics and Protumorigenic Activity with Mesenchymal Stromal Cells, Cancer Res 77(18) (2017) 5142-5157.
[12] O. Hashimoto, M. Yoshida, Y.I. Koma, T. Yanai, D. Hasegawa, Y. Kosaka, N. Nishimura, H. Yokozaki, Collaboration of cancer-associated fibroblasts and tumour-associated macrophages for neuroblastoma development, J Pathol 240(2) (2016) 211-223.
[13] P. Yeung, H.S. Sin, S. Chan, G.C.F. Chan, B.P. Chan, Microencapsulation of Neuroblastoma Cells and Mesenchymal Stromal Cells in Collagen Microspheres: A 3D Model for Cancer Cell Niche Study, Plos One 10(12) (2015).
[14] A. Eggert, N. Ikegaki, J. Kwiatkowski, H. Zhao, G.M. Brodeur, B.P. Himelstein, High-level expression of angiogenic factors is associated with advanced tumor stage in human neuroblastomas, Clin Cancer Res 6(5) (2000) 1900-8.
[15] G. Hasko, J. Linden, B. Cronstein, P. Pacher, Adenosine receptors: therapeutic aspects for inflammatory and immune diseases, Nat Rev Drug Discov 7(9) (2008) 759-70.

[16] J. Blay, T.D. White, D.W. Hoskin, The extracellular fluid of solid carcinomas contains immunosuppressive concentrations of adenosine, Cancer Res 57(13) (1997) 2602-5.
[17] H.K. Eltzschig, L.F. Thompson, J. Karhausen, R.J. Cotta, J.C. Ibla, S.C. Robson, S.P. Colgan, Endogenous adenosine produced during hypoxia attenuates neutrophil accumulation: coordination by extracellular nucleotide metabolism, Blood 104(13) (2004) 3986-92.
[18] J. Bastid, A. Cottalorda-Regairaz, G. Alberici, N. Bonnefoy, J.F. Eliaou, A. Bensussan, ENTPD1/CD39 is a promising therapeutic target in oncology, Oncogene 32(14) (2013) 1743-1751.
[19] L. Wang, J. Fan, L.F. Thompson, Y. Zhang, T. Shin, T.J. Curiel, B. Zhang, CD73 has distinct roles in nonhematopoietic and hematopoietic cells to promote tumor growth in mice, J Clin Invest 121(6) (2011) 2371-2382.
[20] U.K. Decking, G. Schlieper, K. Kroll, J. Schrader, Hypoxia-induced inhibition of adenosine kinase potentiates cardiac adenosine release, Circ Res 81(2) (1997) 154-64.
[21] N. Braekeveldt, D. Bexell, Patient-derived xenografts as preclinical neuroblastoma models, Cell Tissue Res 372(2) (2018) 233-243.
[22] N. Braekeveldt, C. Wigerup, D. Gisselsson, S. Mohlin, M. Merselius, S. Beckman, T. Jonson, A. Borjesson, T. Backman, et al., Neuroblastoma patient-derived orthotopic xenografts retain metastatic patterns and geno- and phenotypes of patient tumours, Int J Cancer 136(5) (2015) E252-E261.
[23] N. Braekeveldt, C. Wigerup, I. Tadeo, S. Beckman, C. Sanden, J. Jonsson, J.S. Erjefalt, A.P. Berbegall, A. Borjesson, et al., Neuroblastoma patient-derived orthotopic xenografts reflect the microenvironmental hallmarks of aggressive patient tumours, Cancer Letters 375(2) (2016) 384-389.
[24] C. Correia, S. Bhumiratana, L.P. Yan, A.L. Oliveira, J.M. Gimble, D. Rockwood, D.L. Kaplan, R.A. Sousa, R.L. Reis, et al., Development of silk-based scaffolds for tissue engineering of bone from human adipose-derived stem cells, Acta Biomater 8(7) (2012) 2483-92.
[25] E. Dondajewska, W. Juzwa, A. Mackiewicz, H. Dams-Kozlowska, Heterotypic breast cancer model based on a silk fibroin scaffold to study the tumor microenvironment, Oncotarget 9(4) (2018) 4935-4950.
[26] B. Subia, T. Dey, S. Sharma, S.C. Kundu, Target specific delivery of anticancer drug in silk fibroin based 3D distribution model of bone-breast cancer cells, ACS Appl Mater Interfaces 7(4) (2015) 2269-79.
[27] L.S. Wray, J. Rnjak-Kovacina, B.B. Mandal, D.F. Schmidt, E.S. Gil, D.L. Kaplan, A silk-based scaffold platform with tunable architecture for engineering critically-sized tissue constructs, Biomaterials 33(36) (2012) 9214-24.
[28] R. Derda, A. Laromaine, A. Mammoto, S.K. Tang, T. Mammoto, D.E. Ingber, G.M. Whitesides, Paper-supported 3D cell culture for tissue-based bioassays, Proc Natl Acad Sci U S A 106(44) (2009) 18457-62.

Appendix I: Culture of PDX Cells

Media Composition:

DMEM

20% FBS

L-glut

Pen Step

Culture protocol:

1. Small portions of frozen stocks were removed using 26 G needled and placed into prewarmed culture media (3 mL, in a 6-well plate)
2. Leave cultures in 37 °C incubator without moving plate for 7 days
3. After 7 days begin periodic media changes (2 per week)

Media change protocol:

1. Removed 1 mL of culture medium
2. Spin down medium at 1000 rpm for 5 minutes
3. Removed medium from cell pellet, take care as very few cells are present
4. Resuspend cells in 1 mL of medium and add to culture

Cells have undergone one passage, which resulted in a high level of cell death. Thus, for future passages the protocol should be revised.

Original passaging protocol:

1. Remove medium from cells
2. Add 0.5 mL of 0.25% Trypsin EDTA to culture
3. Incubate cells with trypsin for 5 minutes at 37 °C
4. Neutralize trypsin with 4 mL of complete medium
5. Centrifuge cells at 1000 rpm for 5 minutes
6. Remove medium from cell pellet
7. Resuspend cell pellet in 3 mL of media and replate in a 6-well plate

Appendix II: MATLAB code for dot blot analysis

Dot blot normalization code

```
%%Dot blot normalization to its own controls
%Upload data file
fileloc=inputdlg('Input the file location below:');
filename=inputdlg('Input file name below:');
file=fullfile(fileloc,filename);
filechar=char(file);
%Read the data file (Save file as Excel Workbook)
dat=xlsread(filechar);
%Normalize to controls (Subtract by average of negative controls (Blanks)

%Take mean of the blank values
controlavg=mean([dat(1,3:5),dat(2,3:5),dat(9,10:13),dat(10,10:13)]);
stddev_neg=std([dat(1,3:5),dat(2,3:5),dat(9,10:13),dat(10,10:13)]);

if controlavg<0
    controlavg==0
else
    controlavg=controlavg

end
%Subtract negative control from each sample
dat_negnorm=dat-controlavg;
```

```
%Take mean of the positive controls
posavg=mean([dat_negnorm(2,1:2),dat_negnorm(9,14),dat_negnorm(10,14)]);
std_pos=std([dat_negnorm(1,1:2),dat_negnorm(9,13:14),dat_negnorm(10,13:14)]);

%Normalize the positive controls
pos_norm=posavg-controlavg;
%Divide by positive control
dat_norm=dat_negnorm/(pos_norm);

%Display heatmap
h=heatmap(dat_norm)

%Save normalized excel sheet
newname=strcat(filechar,"_normalized");
xlswrite(newname,dat_norm);
```

Dot blot normalization to media control

```
%Normalization to Media control
%Upload data file
fileloc_blot=inputdlg('Input the blot file location below:');
filename_blot=inputdlg('Input file name below:');
file_blot=fullfile(fileloc_blot,filename_blot);
filechar_blot=char(file_blot);
%Read the normalized data file for blot comparison
dat_norm=xlsread(filechar_blot);
```

```
%Read in media control Kelly Blot 6
mediacontrol_name='R:\Masters\Dot Blot Images Analysis
_2.0\Kelly\C6\Kelly_MediaControl_6_5min_Results Documents\Kelly_MediaControl_6_5min-
Grid Measurements Table_2_normalized';
control_dat=xlsread(mediacontrol_name);

%Normalized to media control (divide each dot)
media_norm=dat_norm./control_dat;

nrows=10;
ncols=14;
A=zeros(nrows,ncols);

for c=1:ncols
   for r=1:nrows
      if dat_norm(r,c)>0 & control_dat(r,c)<0
         A(r,c)=true;

      else
         A(r,c)=media_norm(r,c);
      end
   end
end

%Save normalized data in Excel
```

```
newname1=strcat(filechar_blot,'media_normalized');

xlswrite(newname1,A);
```

Appendix III: Other gene expression evaluated in hypoxia and scaffolded culture

Gene	**2D 1%**[a]	**3D 21%**[a]	**3D 1%**[a]
LDH5	1.28	3.64	2.26
Nestin	0.76	0.46	0.36
CASPASE 8	0.97	1.18	1.44
VCAN	0.89	0.81	0.76
ITGA	0.92	1.21	2.27
NCAM	1.55	0.69	1.10
VCAM	1.49	1.67	1.98
IL-6R	0.49	1.30	2.64
MIF	1.57	1.51	2.33
OSM	1.53	0.68	1.54
uPAR	0.89	4.93	2.55
PLGF	0.52	1.13	1.08
IL-17A	1.09	0.93	1.22
PDGF	4.63	1.3	8.80

[a] Fold Change Relative to 2D 21%, Representative experiment

Appendix IV: Positive and negative controls for staining

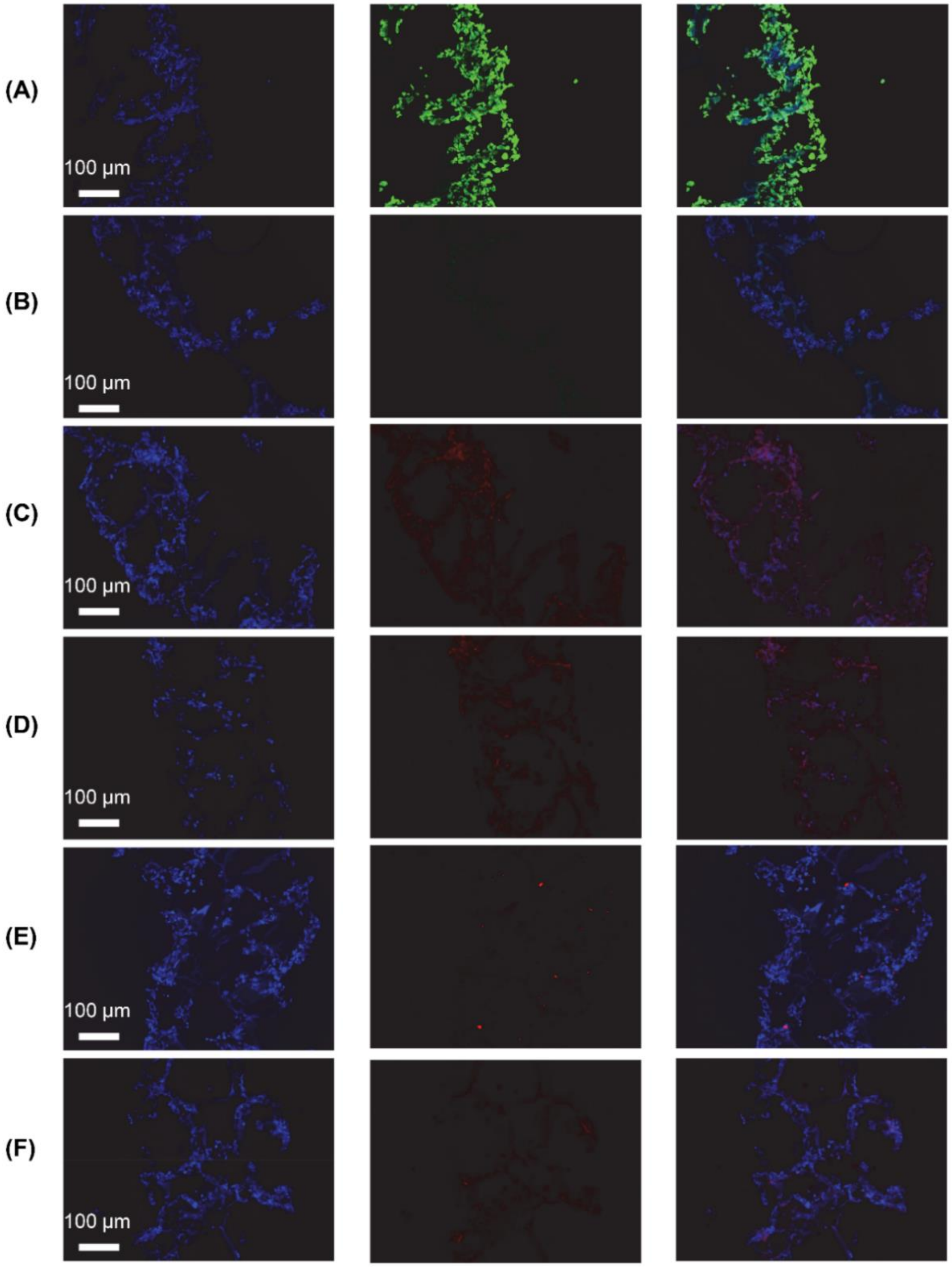

Figure A.IV.1. Positive and negative staining controls.
(A) TUNEL positive control. (B) TUNEL negative control. (C) ki67 ambient oxygen (21%) negative control. (D) ki67 low oxygen (1%) negative control. (E) Pimonidazole negative control for Aim 1 (low oxygen, no pimonoidazole added). (F) Pimonidazole negative control for Aim 2 (low oxygen, no pimonoidazole added).

Appendix V: Hematoxylin and eosin protocol

1. Remove slides from freezer
2. Fix cells in cold (4°C) 100% methanol, 5 minutes
3. Move slides to 25% methanol, 5 minutes
4. PBS at room temperature, 10 minutes
5. Harris hematoxylin, 3 minutes
6. Tap H_2O, 5 minutes
7. Acid Alcohol, 3 dips
8. Tap H_2O, 1 minute
9. Ammonia water, 3 dips
10. 95% ethanol, 1 minute
11. Eosin, 30 seconds
12. 95% ethanol, 1 minute
13. 95% ethanol, 1 minute
14. 100% ethanol, 1 minute
15. 100% ethanol, 1 minute
16. Xylene, 2 minutes
17. Xylene, 5 minutes
18. Mount with cytoseal

Appendix VI: Periodic acid -Schiffs base protocol

1. Bring slides to room temperature
2. Distilled water, 5 minutes
3. 0.5% Periodic Acid, 7 minutes
4. Distilled water, 1 minute
5. Schiff Reagent, 15 minutes
6. Running tap H_2O, 10 minutes
7. 95% ethanol, 1 minute
8. 95% ethanol, 1 minute
9. 100% ethanol, 1 minute
10. 100% ethanol, 1 minute
11. Xylene, 2 minutes
12. Xylene, 5 minutes

Appendix VII: Clinical correlation to gene and cytokine changes

Gene/Cytokine	Clinical Correlation
VEGF	Expressed clinically in NB, correlated with poor prognosis [1]
CAIX	Expressed clinically in NB, correlated with reduced survival [2]
GLUT1	Expressed clinically in NB, correlated with unfavorable histology and high-risk patients [3]
IGFBP3	No current clinical link, *in vitro* mechanism undetermined
MMP9	Correlated with poor overall survival in patients [4]
GM-CSF	Used as part of a therapeutic regime to enhance immune cell infiltration [5-7]
MCP-3	Not clinically linked to NB
TNFRI	Not clinically linked to NB
TPO	Not clinically linked to NB
GRO	Not clinically linked to NB
CXCL1	Not clinically linked to NB
PLGF	Identified as part of a malignant gene signature, secretion higher in high stage tumors [8]
IL-10	
IL-17A	Not clinically linked to NB
TNFRII	Not clinically linked to NB
IL-6R	
IL-8	Expressed in patient samples [9]
G-CSF	Linked to highly tumorigenic NB cells [10-12]
HCC4	Not clinically linked to NB
MSP	Not clinically linked to NB
I-TA	Not clinically linked to NB
CCL3	Not clinically linked to NB
uPAR	Overexpressed in high-risk NB, and associated with invasion, metastasis, and poor prognosis [13]

References

[1] G. Jakovljevic, S. Culic, J. Stepan, A. Bonevski, S. Seiwerth, Vascular endothelial growth factor in children with neuroblastoma: a retrospective analysis, J Exp Clin Cancer Res 28 (2009) 143.

[2] H.M. Ameis, A. Drenckhan, M. Freytag, J.R. Izbicki, C.T. Supuran, K. Reinshagen, S. Holland-Cunz, S.J. Gros, Carbonic anhydrase IX correlates with survival and is a potential therapeutic target for neuroblastoma, J Enzym Inhib Med Ch 31(3) (2016) 404-409.

[3] P. Ramani, A. Headford, M.T. May, GLUT1 protein expression correlates with unfavourable histologic category and high risk in patients with neuroblastic tumours, Virchows Arch 462(2) (2013) 203-9.

[4] F.H. Khan, V. Pandian, S. Ramraj, S. Aravindan, T.S. Herman, N. Aravindan, Reorganization of metastamiRs in the evolution of metastatic aggressive neuroblastoma cells, Bmc Genomics 16 (2015).

[5] S. Inoue, Y. Setoyama, A. Odaka, D. Kitagawa, Y. Beck, Chemoimmunotherapeutic effect of combined treatment with ex vivo generated antigen-presenting immune cells and conventional antitumor agents in a mouse neuroblastoma model, Journal of Pediatric Surgery 52(10) (2017) 1642-1650.

[6] M. Fukuda, K. Horibe, K. Furukawa, Enhancement of in vitro and in vivo anti-tumor activity of anti-GD2 monoclonal antibody 220-51 against human neuroblastoma by granulocyte-macrophage colony-stimulating factor and granulocyte colony-stimulating factor, Int J Mol Med 2(4) (1998) 471-5.

[7] D.R. Barreda, P.C. Hanington, M. Belosevic, Regulation of myeloid development and function by colony stimulating factors, Dev Comp Immunol 28(5) (2004) 509-54.

[8] K. Zins, D. Kovatchki, T. Lucas, D. Abraham, PlGF and VEGF-A Regulate Growth of High-Risk MYCN-Single Copy Neuroblastoma Xenografts via Different Mechanisms, Int J Mol Sci 17(10) (2016).

[9] F.A. Ferrer, A.G. Pantschenko, L.J. Miller, K. Anderson, M. Grunnet, P.H. McKenna, D. Kreutzer, Angiogenesis and neuroblastomas: interleukin-8 and interleukin-8 receptor expression in human neuroblastoma, J Urol 164(3 Pt 2) (2000) 1016-20.

[10] E.S. Kim, S. Agarwal, J.M. Shohet, G-CSF Is a Cancer Stem Cell-Specific Growth Factor-Response, Cancer Res 75(18) (2015) 3992.

[11] S. Agarwal, A. Lakoma, Z. Chen, J. Hicks, L.S. Metelitsa, E.S. Kim, J.M. Shohet, G-CSF Promotes Neuroblastoma Tumorigenicity and Metastasis via STAT3-Dependent Cancer Stem Cell Activation, Cancer Res 75(12) (2015) 2566-79.

[12] D.M. Hsu, S. Agarwal, A. Benham, C. Coarfa, D.N. Trahan, Z. Chen, P.N. Stowers, A.N. Courtney, A. Lakoma, E. Barbieri, L.S. Metelitsa, P. Gunaratne, E.S. Kim, J.M. Shohet, G-CSF receptor positive neuroblastoma subpopulations are enriched in chemotherapy-resistant or relapsed tumors and are highly tumorigenic, Cancer Res 73(13) (2013) 4134-46.

[13] P. Li, Y. Gao, Z. Ji, X. Zhang, Q. Xu, G. Li, Z. Guo, B. Zheng, X. Guo, Role of urokinase plasminogen activator and its receptor in metastasis and invasion of neuroblastoma, J Pediatr Surg 39(10) (2004) 1512

Appendix VII: Dot blot protocol

1. Remove kit from cold storage and allow to equilibrate to room temperature
2. Remove the antibody arrays from the packaging and place (printed side up) into a well of the incubation tray (one per well)
3. Pipette 2 mL of blocking buffer (supplied) into each well and incubate for 30 min at room temperature
4. Aspirate blocking buffer from each well with a pipette
5. Pipette 1 mL of undiluted media (1 freeze thaw cycle, centrifuged to remove debris) into each well and incubate overnight at 4°C on a rocking platform shaker
6. Aspirate samples from each well with a pipette
7. Dilute wash buffer I and wash buffer II (both 20-fold) with ultrapure water
8. Pipette 2 mL of 1x wash buffer I into each wel land incubate for 5 min at room temperature. Repeat 2 more times for a total of 3 washes using fresh buffer and aspirating out the buffer completely each time
9. Pipette 2 mL of 1x wash buffer II into each well and incubate for 5 min at room temperature. Repeat 1 more times for a total of 2 washes using fresh buffer and aspirating out the buffer completely each time
10. Pipette 2 mL of blocking buffer into the bottle of biotinylated antibody cocktail, mix gently with a pipette
11. Pipette 1 mL of the prepared biotinylated antibody cocktail into each well and incubate for 2 h at room temperature
12. Aspirate biotinylated antibody cocktail from each well with a pipette
13. Wash membranes as directed in steps 8 and 9
14. Dilute HRP-Streptavidin (1000-fold) with blocking buffer, mix gently with a pipette
15. Pipette 2 mL of 1x HRP-Streptavidin into each well and incubate for 2 h at room temperature
16. Aspirate HRP-Streptavidin from each well with a pipette
17. Wash membranes as directed in steps 8 and 9
18. Transfer the membranes, printed side up onto a piece of tissue or blotting paper on a flat benchtop
19. Remove excess wash buffer by blotting the membrane edges with another piece of paper
20. Transfer and place the membranes, printed side up, onto a plastic sheet
21. In a clean tube, pipette equal volumes of detection buffer C and detetection buffer D (250 µL of each, for a total of 500 µL is enough for one membrane)
22. Gently pipette 500 µL of the detection buffer mixture onto each membrane and incubate for 2 mins at room temperature (Do not rock or shake)

23. Place another plastic sheet on top of the membranes by starting at one end and gently "rolling" the flexible plastic sheet across the surface to the opposite end to smooth out any air bubbles. The membranes should now be "sandwiched" between two plastic sheets.
24. Transfer the sandwiched membranes to the chemiluminescence imaging system such as a CCD camera (recommended) and expose.
25. Steps 22-24 can be repeated if chemiluminescence fades

Appendix IX: ELISA protocol

1. Dilure the capture antibody to the working dilution (specific to each lot) in PBS without carrier protein. Immediately coat a 96-well microplate with 100 µL per well of the diluted capture antibody. Seal the plate and incubate overnight at room temperaute.
2. Aspirate each well and wash with wash buffer, repeating the process two times for a total of three washes. Wash by filling each well with wash buffer using a squirt bottle. To completely remove wash buffer, blot against clean papr towels.
3. Block plates by adding 300 µL of reagent dilutent (blocking solution for IL-8) to each well. Incubate at room temperature for 1 hr.
4. Repeat the aspiration/wash as in step 2.
5. Add 100 µL of sample of standards in reagent dilutent per well. Standards are specific to individual lots, samples run undiluted , 1:10, and 1:100. Seal the plate and incubate for 2 h at room temperature.
6. Repeat the aspiration/wash as in step 2.
7. Add 100 µL of the detection antibody (diluted in reagent dilution, specific to each lot) to each well. Cover plate and incubate for 2 hr at room temperature.
8. Repeat the aspiration/wash as in step 2.
9. Add 100 µL of the working dilution of streptavidin-HRP (diluted in reagent dilution, specific to each lot) to each well. Cover the plate and incubate for 20 min at room temperature. Avoid placing the plate in direct light.
10. Repeat the aspiration/wash as in step 2.
11. Add 100 µL of substrate solution (not supplied) to each well. Incubate for 20 mins at room temperature. Avoid placing the plate in direct light.
12. Add 50 µL of stop solution to each well. Gently tap the plate to ensure thorough mixing.
13. Using a microplate reader, determing optical density of eacg well at wavelengths of 450 nm, 540 nm, 570 nm. Readings done at 540 nm and 570 nm are background readings which can be subtracted from 450 nm data.

Assay components not in kit:

Wash buffer (All): 0.05% Tween® 20 in PBS, pH 7.2-7.4, 0.2 µm filtered

Regent Dilutent (GM-CSF, MCP-3, VEGF), Blocking solution (IL-8): 1% BSA in PBS, pH 7.2-7.4, 0.2 µm filtered

Reagent Dilutent (IL-8): 0.1% BSA, 0.05% Tween® 20 in Tris-buffered Saline, pH 7.2-7.4, 0.2 µm filtered

Substrate solution: BIOFX EXTENDED RANGE TMB

Stop solution: 2N H_2SO_4

Appendix X: Picogreen protocol

- Quanti-iT Picogreen dsDNA Reagent and Kit
    - 20X TE Buffer
    - Lambda DNA Standard
    - PicoGreen dsDNA reagent
- Black Plate (brand new – this is because it is believed that PicoGreen stains plates)

1. Make fresh 1 x TE buffer **if necessary**. (1.25 mL 22 x buffer into 23.75 mL filtered milliq water). Left over buffer can be stored in the fridge 4C.
2. Dilute all the sample supernatant as described with 1X TE buffer using labeled new tubes, so that the final concentration of Triton is 0.1% (e.g. 80 ul of 1x TE + 20 ul of sample in 0.5% TE buffer)
3. Prepare DNA standard (found in kit in fridge). In 1x TE + 0.1% Triton

Standard	How to Prep
S1 -2 ug	5 µL DNA standard & 245 µL 1X TE Buffer
S2- 0.667 ug	75 µL S1 & 150 µL of 1X TE Buffer
S3-0.222 ug	75 µL S2 & 150 µL of 1X TE Buffer
S4-0.074 ug	75 µL S3 & 150 µL of 1X TE Buffer
S5-0.025 ug	75 µL S4 & 150 µL of 1X TE Buffer
S6-0.008 ug	75 µL S5 & 150 µL of 1X TE Buffer
S7-0.0027 ug	75 µL S6 & 150 µL of 1X TE Buffer
S8 Blank	200 µL of 1X TE Buffer

4. Prepare pico green reagent diluting 5ul per 995 ul of 1X TE Buffer.
5. Turn off the lights in work area.
6. Using a new black plate add 50 µL of PicoGreen to each well and then add 50 µL of sample to the respective wells. Mix thoroughly. Plate duplicates of standard.
7. Let incubate in a drawer for 5 minutes.
8. Read on plate reader using the appropriate PicoGreen protocol (standard fluorescein wavelengths, excitation ~480 nm, emission ~520 nm) three times.